The current version of the human genome reference assembly, GRCh38.p14 (GRCh38), has millions of bases represented by the letter "N," which means that the actual base residing at that location is unknown.

There are also 169 sequences that cannot confidently be ordered or oriented within the assembly, typically owing to their repetitive nature

Until recently, limitations of sequencing technology, primarily that the sequencers could read no more than about 1000 bases at a time,

The HGP opted for a more structured approach. This involved cloning genomic DNA into pieces that could be grown in bacteria (clones) and indexed in 96-well plates. Clones from these libraries were first mapped to chromosome regions, then individually sequenced.

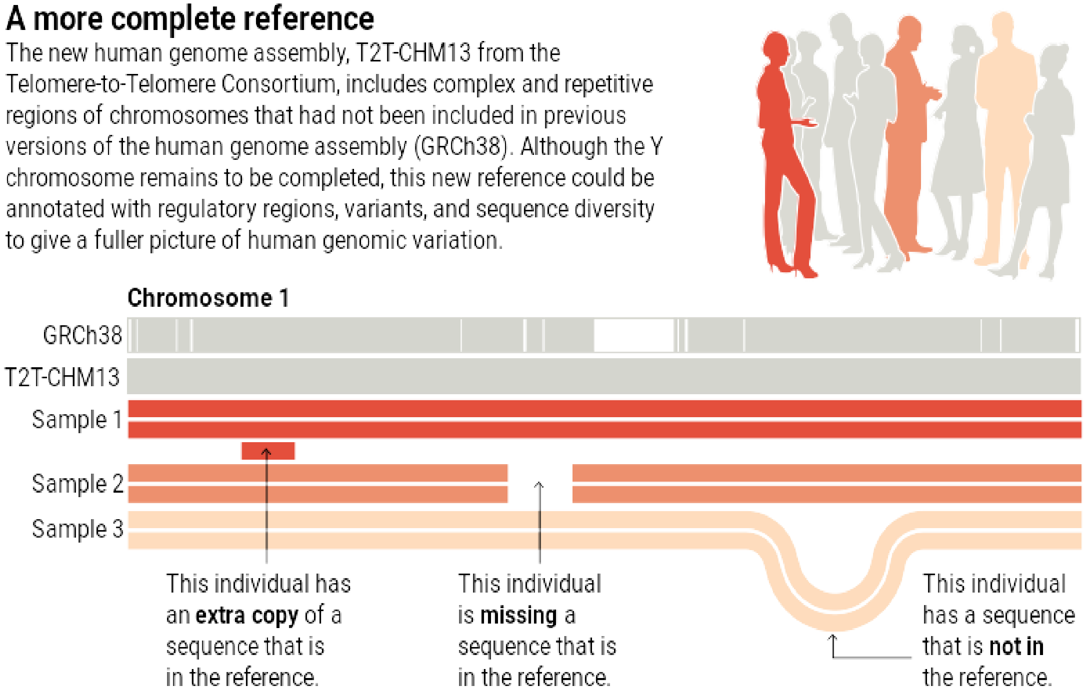

A more complete reference

The new human genome assembly, T2T-CHM13 from the Telomere-to-Telomere Consortium, includes complex and repetitive regions of chromosomes that had not been included in previous versions of the human genome assembly (GRCh38). Although the Y chromosome remains to be completed, this new reference could be annotated with regulatory regions, variants, and sequence diversity to give a fuller picture of human genomic variation.

This individual has an **extra copy** of a sequence that is in the reference.

This individual is **missing** a sequence that is in the reference.

This individual has a sequence that is **not in** the reference.

An important attribute of the human reference assembly is that the source DNA was derived from multiple individuals.

when two clones from different haplotypes of an individual are adjacent in the reference assembly, this can create sequence representations that are not normally found in the population

T2T Consortium, eliminated the problem of allelic diversity by sequencing the genome of a cell line derived from a complete hydatidiform mole (CHM).

This is duplicated so that the cell contains two copies of the same parental genome

A next-generation human genome sequence, Volume: 376, Issue: 6588, Pages: 34-35, DOI: (10.1126/science.abo5367)

Genome sequencing

February 2001 - Publication of the first draft of the human genome

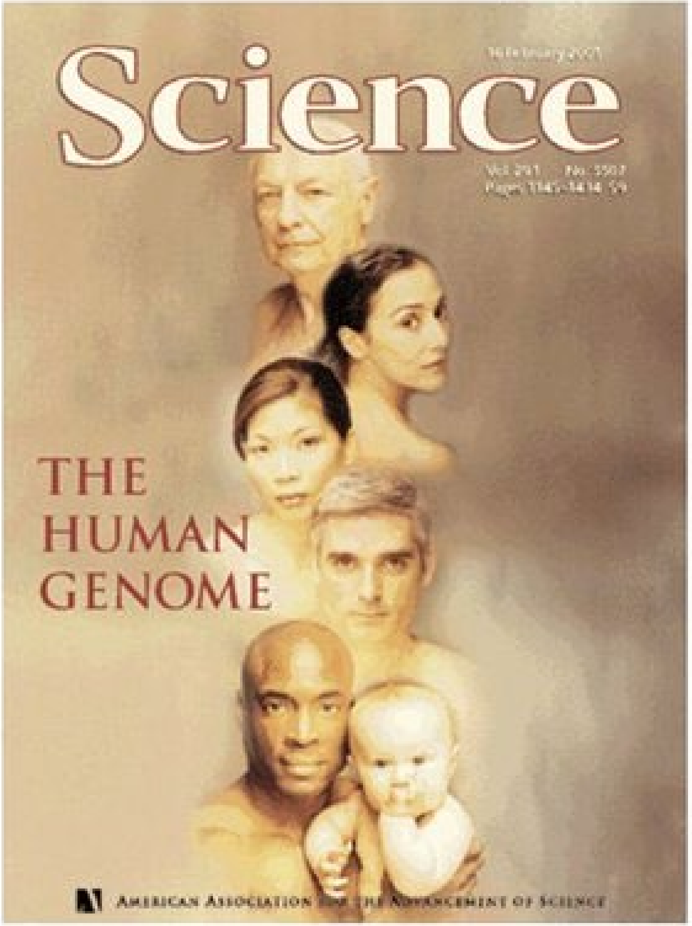

DNA Sequencing

https://www.youtube.com/watch?v=vK-HIMaitnE

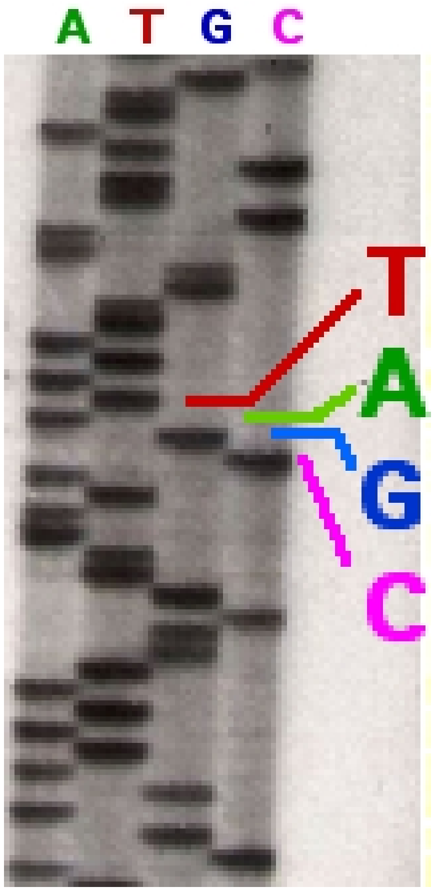

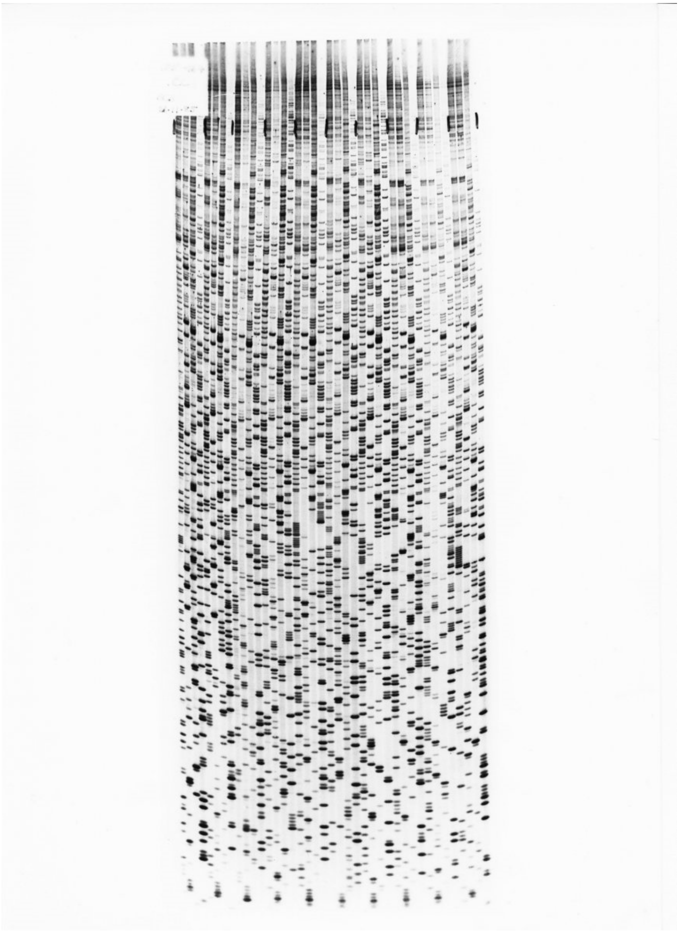

100-1000 bps

DNA Sequencing

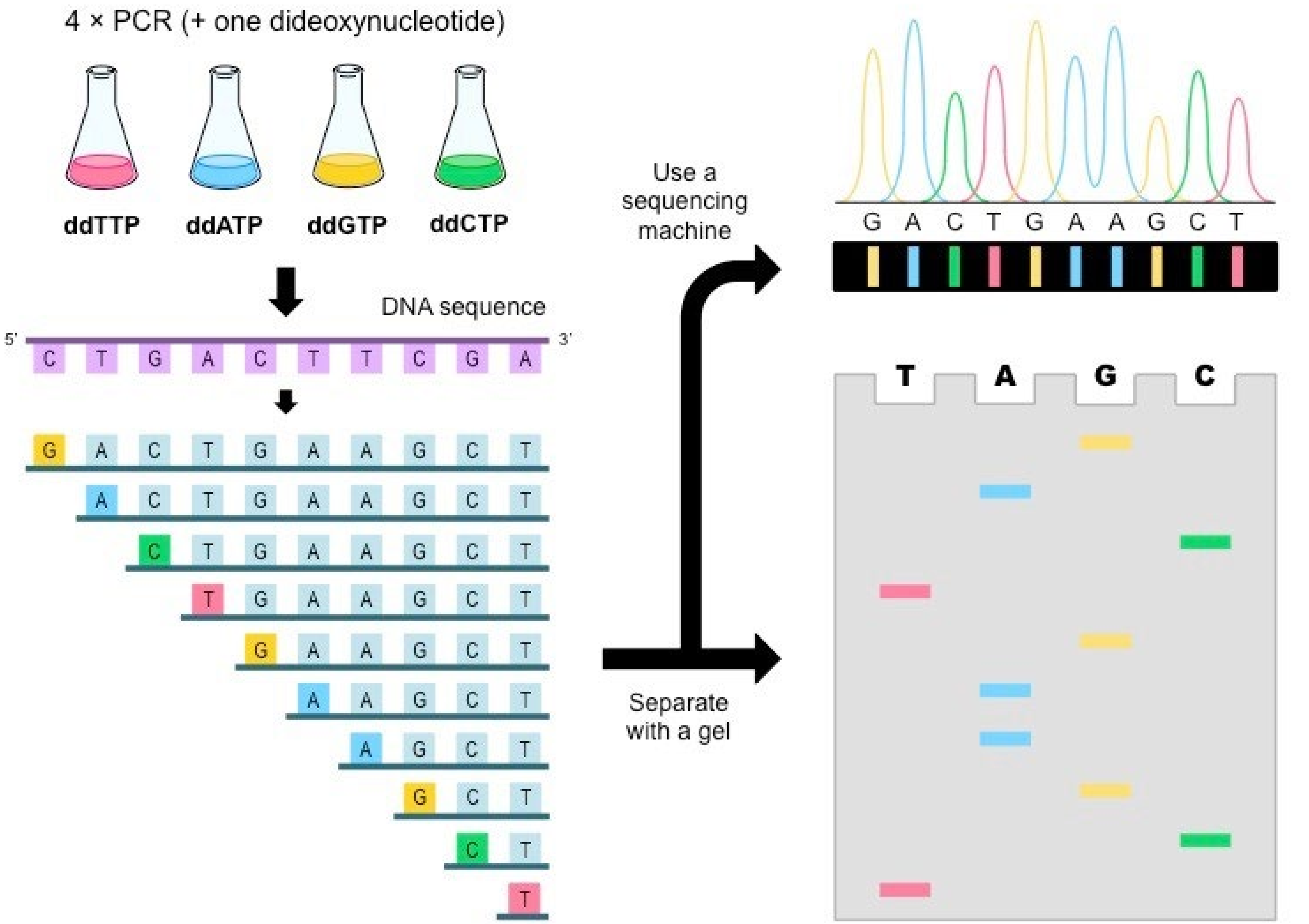

Dye Terminations

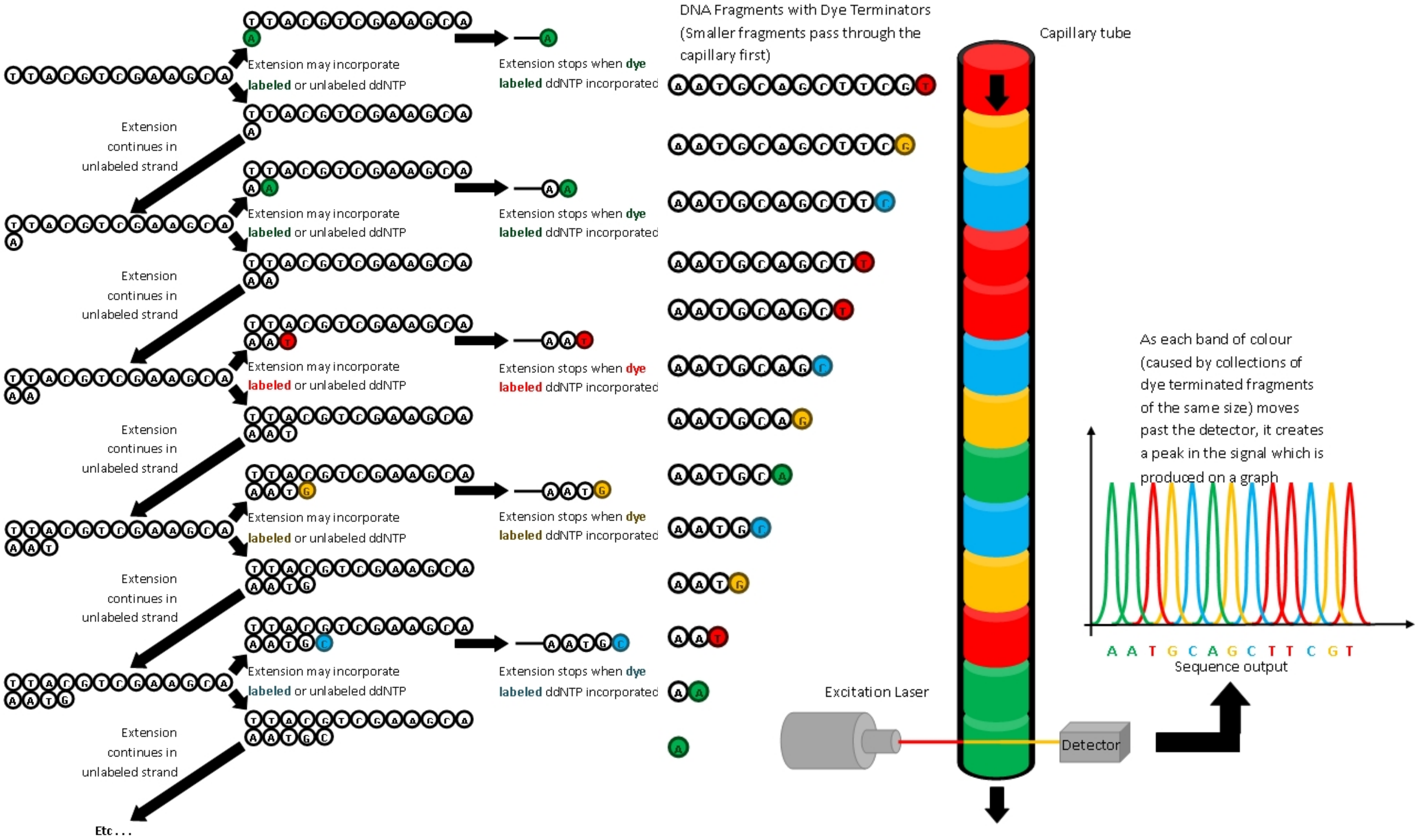

Extension may incorporate **labeled** or unlabeled ddNTP

Extension stops when **dye labeled** ddNTP incorporated

Extension continues in unlabeled strand

Extension may incorporate **labeled** or unlabeled ddNTP

Extension stops when **dye labeled** ddNTP incorporated

Extension continues in unlabeled strand

Extension may incorporate **labeled** or unlabeled ddNTP

Extension stops when **dye labeled** ddNTP incorporated

Extension continues in unlabeled strand

Extension may incorporate **labeled** or unlabeled ddNTP

Extension stops when **dye labeled** ddNTP incorporated

Extension continues in unlabeled strand

Extension may incorporate **labeled** or unlabeled ddNTP

Extension stops when **dye labeled** ddNTP incorporated

Extension continues in unlabeled strand

Etc . . .

DNA Fragments with Dye Terminators (Smaller fragments pass through the capillary first)

Capillary tube

As each band of colour (caused by collections of dye terminated fragments of the same size) moves past the detector, it creates a peak in the signal which is produced on a graph

Excitation Laser

Detector

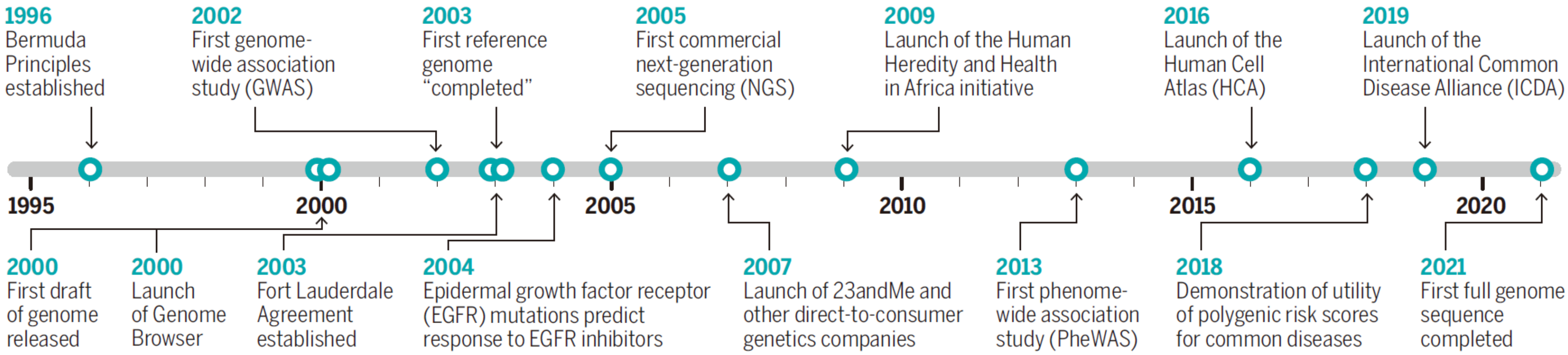

1996 Bermuda Principles established

2002 First genome-wide association study (GWAS)

2003 First reference genome "completed"

2005 First commercial next-generation sequencing (NGS)

2009 Launch of the Human Heredity and Health in Africa initiative

2016 Launch of the Human Cell Atlas (HCA)

2019 Launch of the International Common Disease Alliance (ICDA)

2000 First draft of genome released

2000 Launch of Genome Browser

2003 Fort Lauderdale Agreement established

2004 Epidermal growth factor receptor (EGFR) mutations predict response to EGFR inhibitors

2007 Launch of 23andMe and other direct-to-consumer genetics companies

2013 First phenome-wide association study (PheWAS)

2018 Demonstration of utility of polygenic risk scores for common diseases

2021 First full genome sequence completed

Bermuda Principles

- Automatic release of sequence assemblies larger than 1 kb (preferably within 24 hours).
- Immediate publication of finished annotated sequences.
- Aim to make the entire sequence freely available in the public domain for both research and development in order to maximise benefits to society.

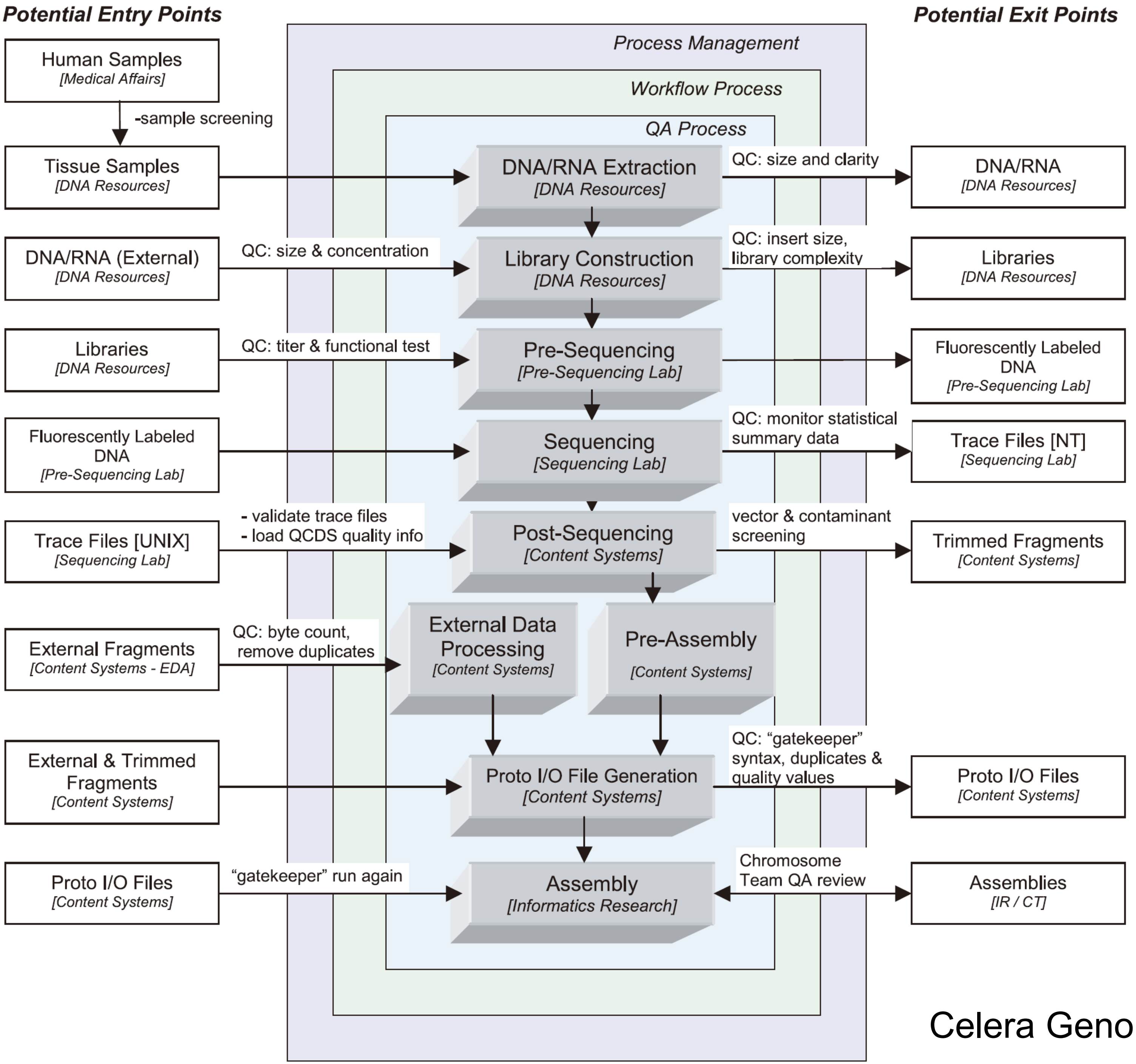

Potential Entry Points

Potential Exit Points

Process Management

Workflow Process

QA Process

Human Samples
[Medical Affairs]

-sample screening

Tissue Samples
[DNA Resources]

DNA/RNA Extraction
[DNA Resources]

QC: size and clarity

DNA/RNA
[DNA Resources]

DNA/RNA (External)
[DNA Resources]

QC: size & concentration

Library Construction
[DNA Resources]

QC: insert size, library complexity

Libraries
[DNA Resources]

Libraries
[DNA Resources]

QC: titer & functional test

Pre-Sequencing
[Pre-Sequencing Lab]

Fluorescently Labeled DNA
[Pre-Sequencing Lab]

Fluorescently Labeled DNA
[Pre-Sequencing Lab]

Sequencing
[Sequencing Lab]

QC: monitor statistical summary data

Trace Files [NT]
[Sequencing Lab]

Trace Files [UNIX]
[Sequencing Lab]

- validate trace files
- load QCDS quality info

Post-Sequencing
[Content Systems]

vector & contaminant screening

Trimmed Fragments
[Content Systems]

External Fragments
[Content Systems - EDA]

QC: byte count, remove duplicates

External Data Processing
[Content Systems]

Pre-Assembly
[Content Systems]

External & Trimmed Fragments
[Content Systems]

Proto I/O File Generation
[Content Systems]

QC: “gatekeeper” syntax, duplicates & quality values

Proto I/O Files
[Content Systems]

Proto I/O Files
[Content Systems]

“gatekeeper” run again

Assembly
[Informatics Research]

Chromosome Team QA review

Assemblies
[IR / CT]

Celera Genomic

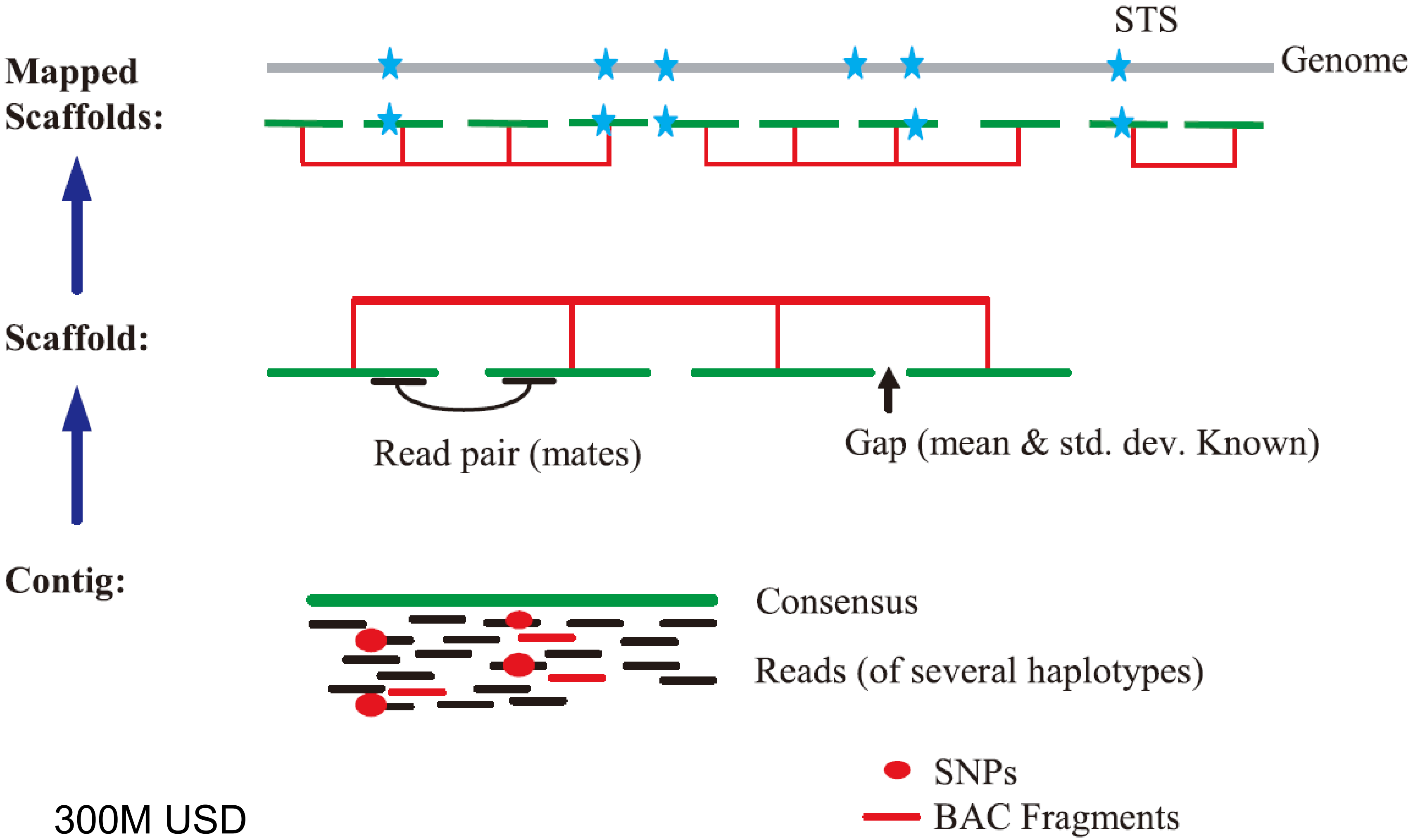

STS

Genome

Mapped Scaffolds:

Scaffold:

Read pair (mates)

Gap (mean & std. dev. Known)

Contig:

Consensus

Reads (of several haplotypes)

● SNPs

▬ BAC Fragments

300M USD
2.9 bbp
9 months
5 donors
5.1 folds
Whole-genome shotgun

Human Genome Project

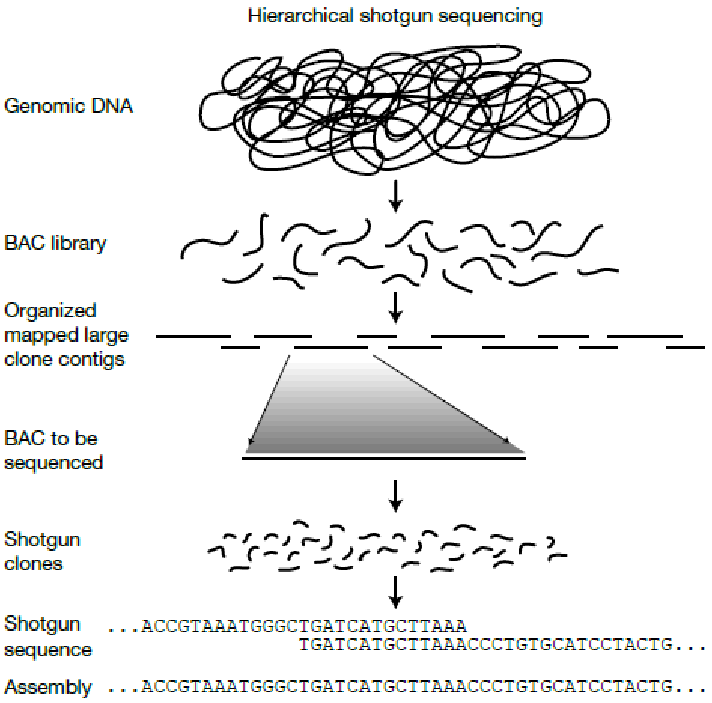

1990 15-year project 3B USD
20 groups
15 months

a)

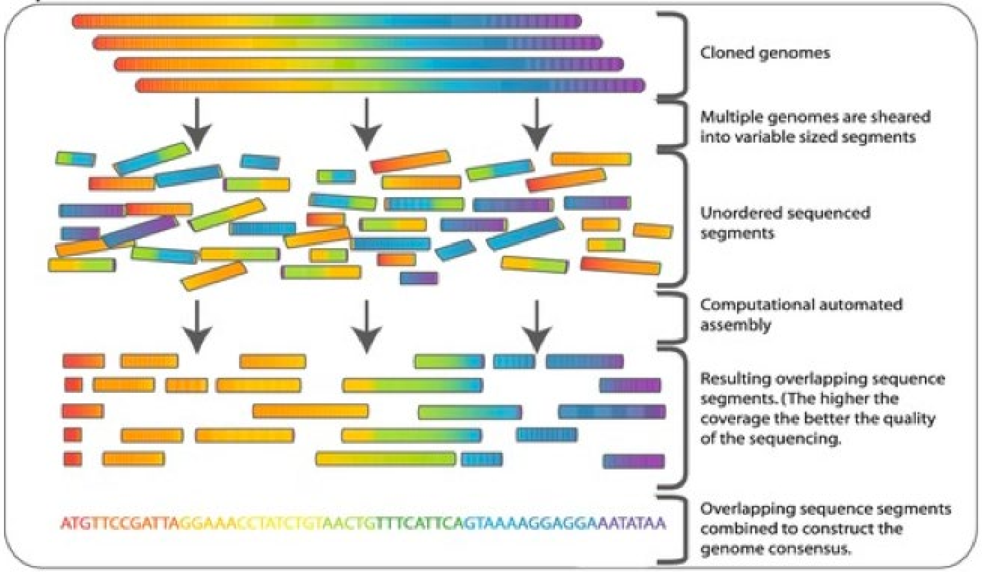
Cloned genomes
Multiple genomes are sheared into variable sized segments
Unordered sequenced segments
Computational automated assembly
Resulting overlapping sequence segments. (The higher the coverage the better the quality of the sequencing.
ATGTTCCGATTAGGAAACCTATCTGTAACTGTTTCATTCAGTAAAAGGAGGAAATATAA
Overlapping sequence segments combined to construct the genome consensus.

b)

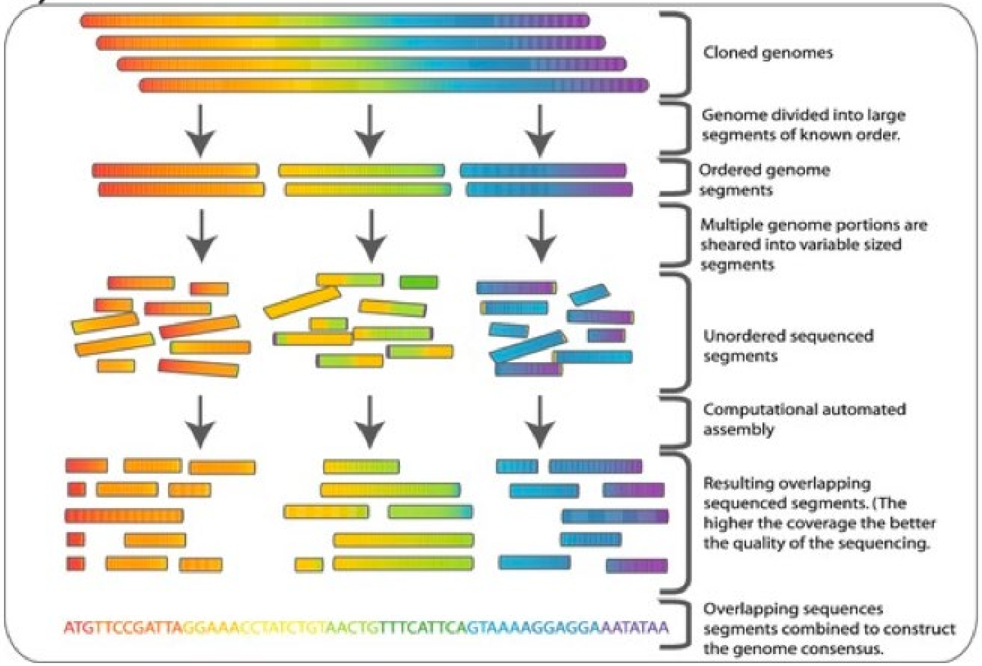
Cloned genomes
Genome divided into large segments of known order.
Ordered genome segments
Multiple genome portions are sheared into variable sized segments
Unordered sequenced segments
Computational automated assembly
Resulting overlapping sequenced segments. (The higher the coverage the better the quality of the sequencing.
ATGTTCCGATTAGGAAACCTATCTGTAACTGTTTCATTCAGTAAAAGGAGGAAATATAA
Overlapping sequences segments combined to construct the genome consensus.

Next Generation Sequencing

https://www.youtube.com/watch?v=fCd6B5HRaZ8

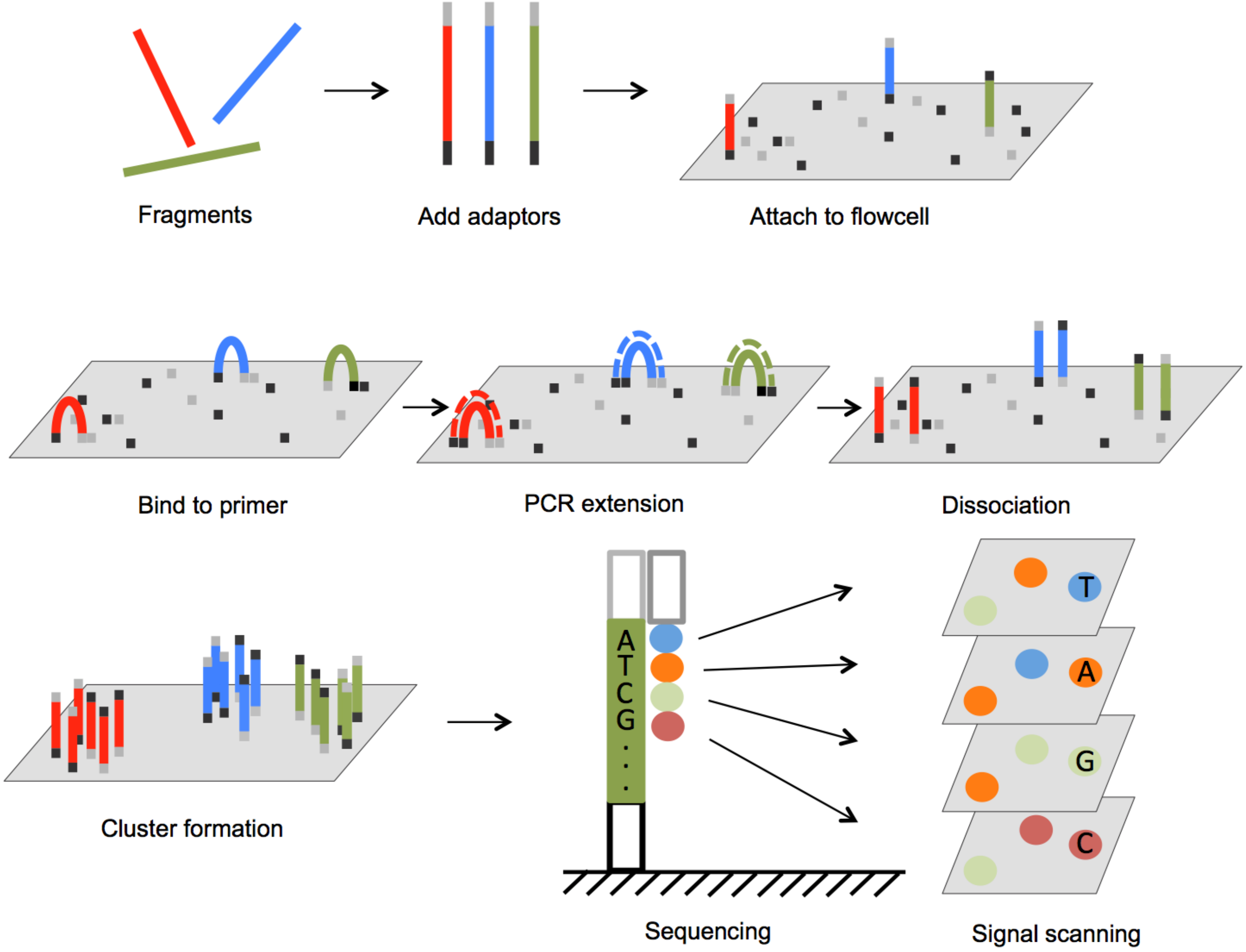

Third Generation Sequencing

PacBio SMRT seq

DNA passes thru polymerase in an illuminated volume

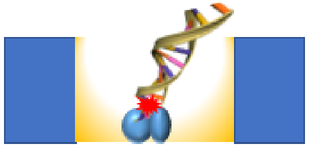

Raw output is fluorescent signal of the nucleotide incorporation, specific to each nucleotide

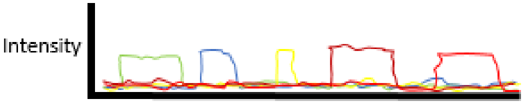

A,C,T,G have known pulse durations, which are used to infer methylated nucleotides

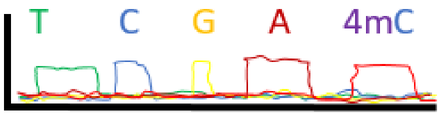

Oxford Nanopore

DNA passes thru nanopore

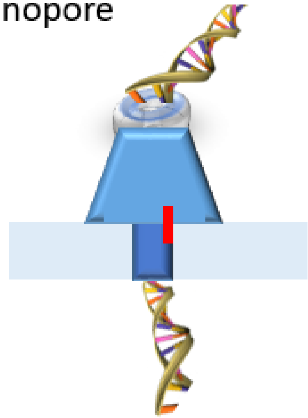

Raw output is electrical signal caused by nucleotide blocking ion flow in nanopore

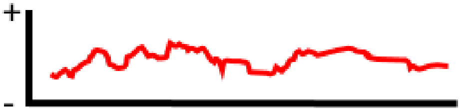

Each nucleotide has a specific electric “signature”

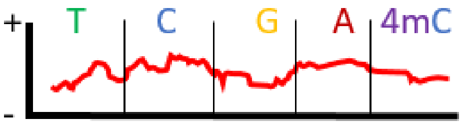

Zero Mode Waveguide

https://www.youtube.com/watch?v=NHCJ8PtYCFc

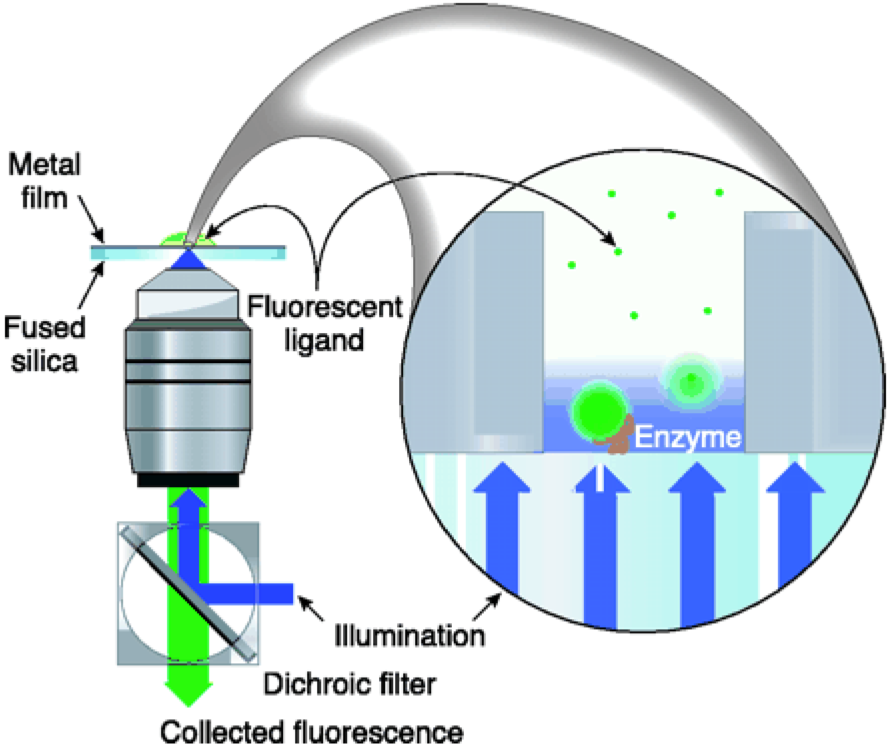

SCIENCE VOL 299 31 JANUARY 2003

Zero Mode Waveguide

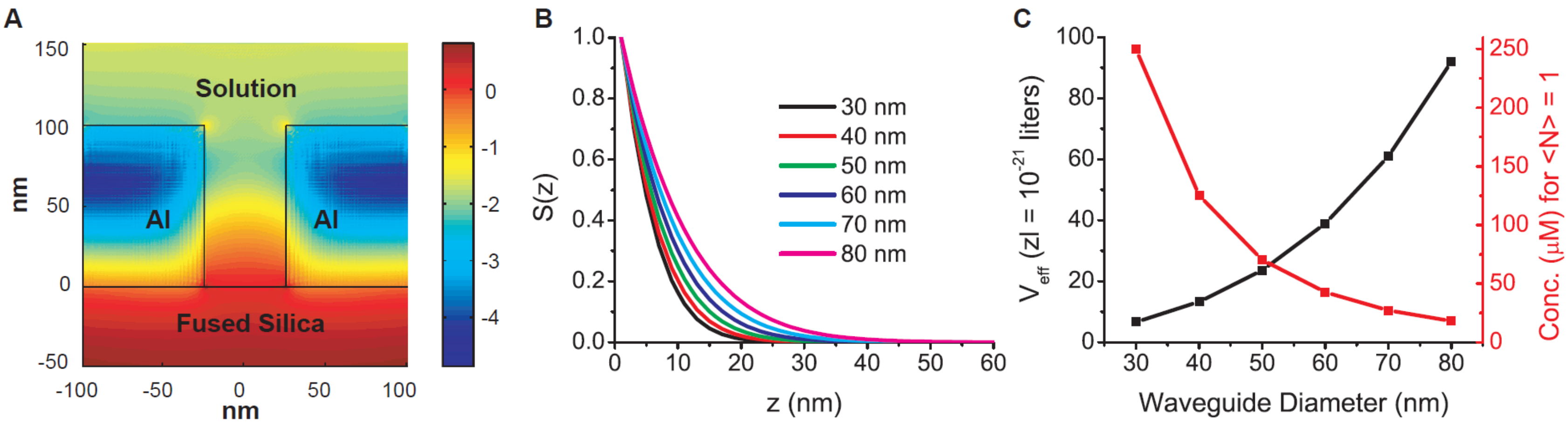

$50 \times 50 \times 10\ nm^3 = 2.5 \times 10^4 \times 10^{-21}\ cc = 2.5 \times 10^{-20}\ L = 25$ zeptoliter

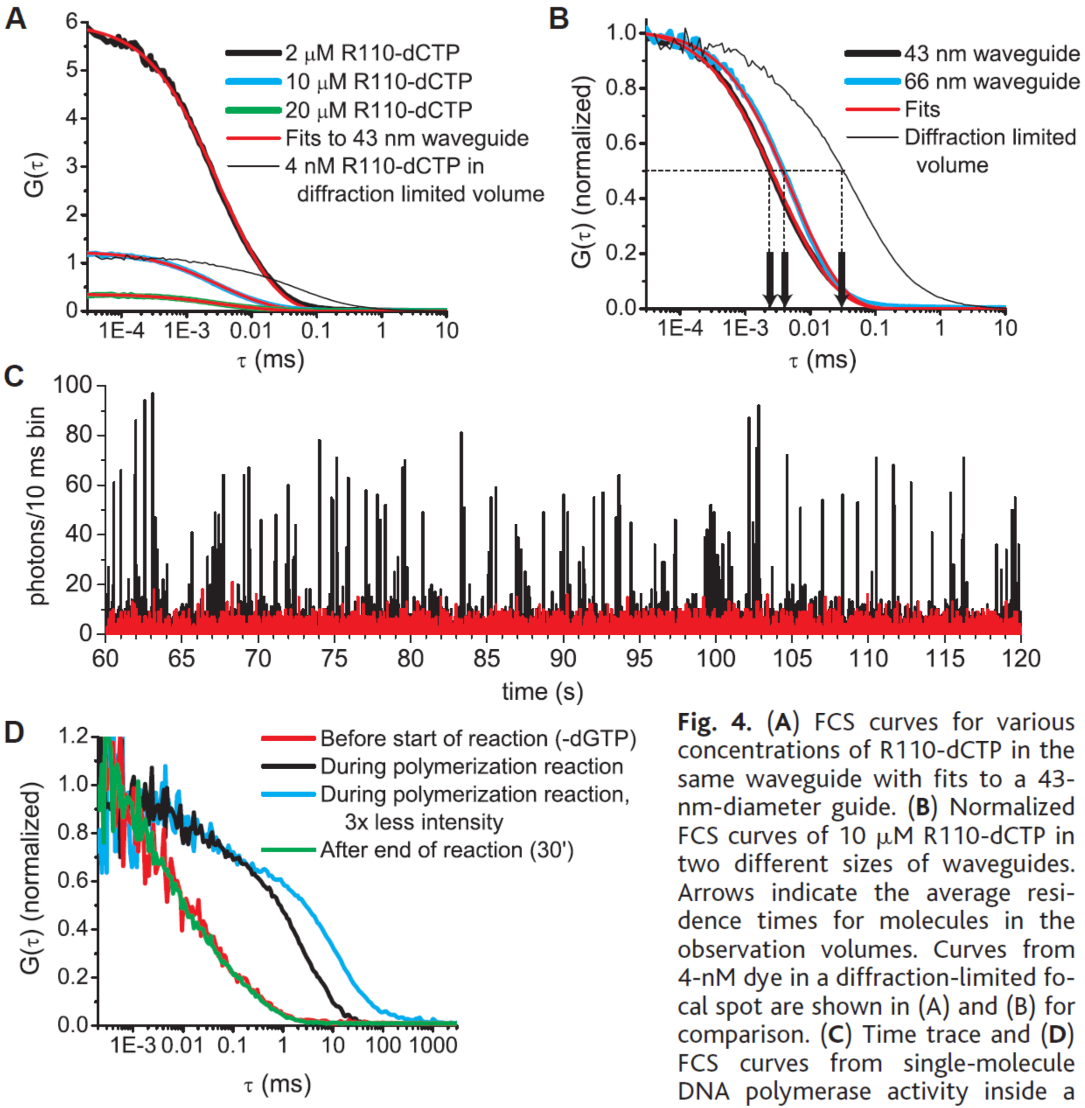

Fig. 4. (**A**) FCS curves for various concentrations of R110-dCTP in the same waveguide with fits to a 43-nm-diameter guide. (**B**) Normalized FCS curves of 10 μM R110-dCTP in two different sizes of waveguides. Arrows indicate the average residence times for molecules in the observation volumes. Curves from 4-nM dye in a diffraction-limited focal spot are shown in (A) and (B) for comparison. (**C**) Time trace and (**D**) FCS curves from single-molecule DNA polymerase activity inside a zero-mode waveguide. Incorporation events and subsequent photobleaching of coumarin-dCTP appear as distinct fluorescence bursts in the black time trace (10-ms time bins). This results in a long-time shoulder in the corresponding FCS curves during polymerization (black and blue curves) in (D). Decreasing the intensity results in slower photobleaching as seen by the longer residence time in the blue curve. The red curves in (C) and (D) are the corresponding negative controls (absence of one native nucleotide) in the same waveguide before initiation of the reaction. The green curve in (D) is the control after the reaction has stopped.

Real-Time DNA Sequencing from Single Polymerase Molecules

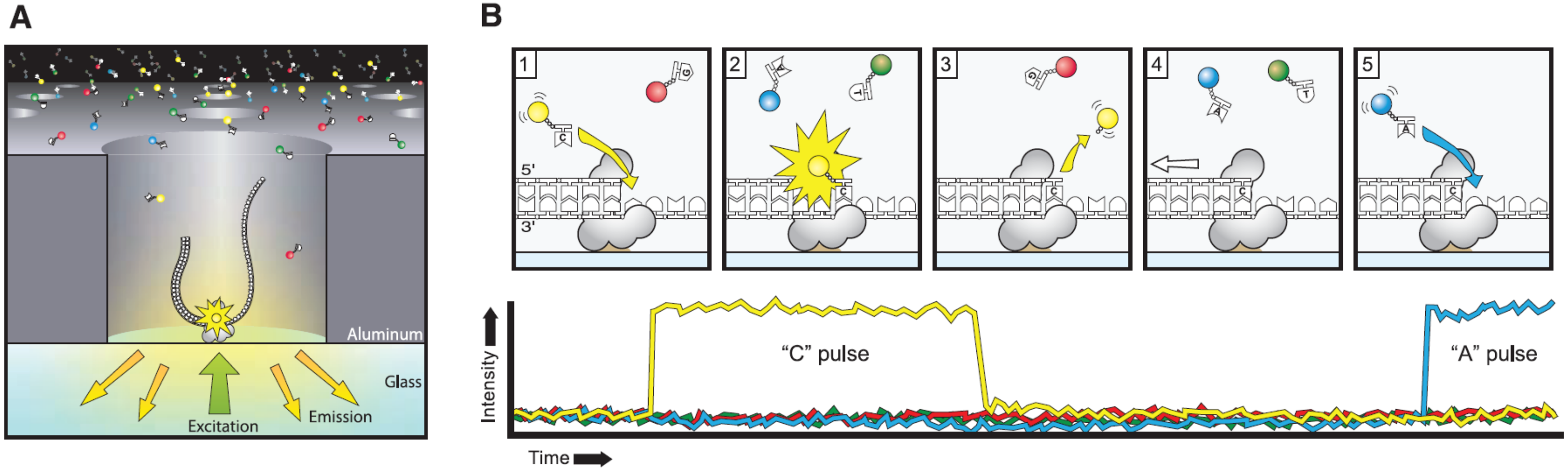

SCIENCE VOL 323 2 JANUARY 2009

Nanopore Sequencing

https://www.youtube.com/watch?v=RcP85JHLmnI

https://www.youtube.com/watch?v=qzusVw4Dp8w

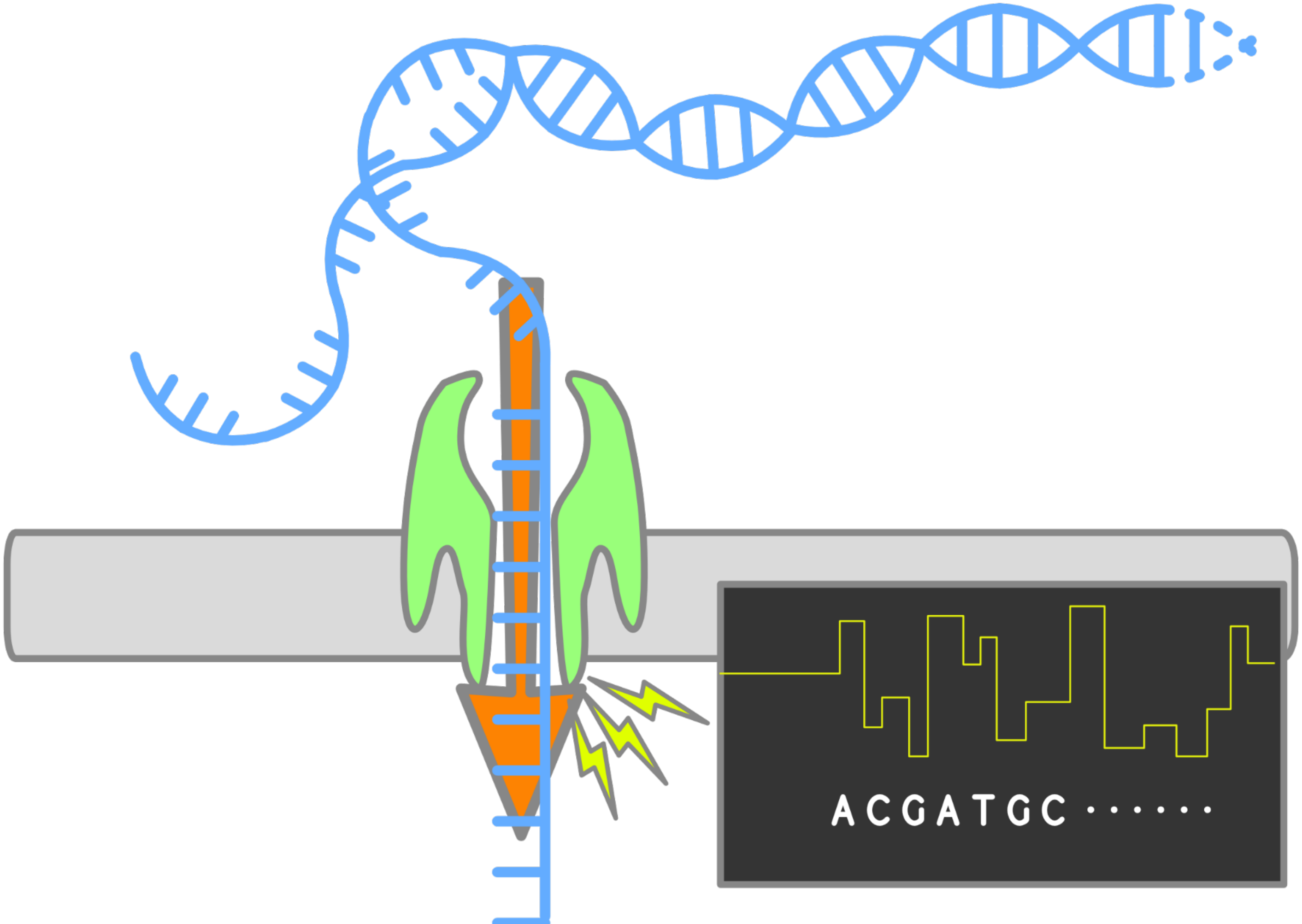

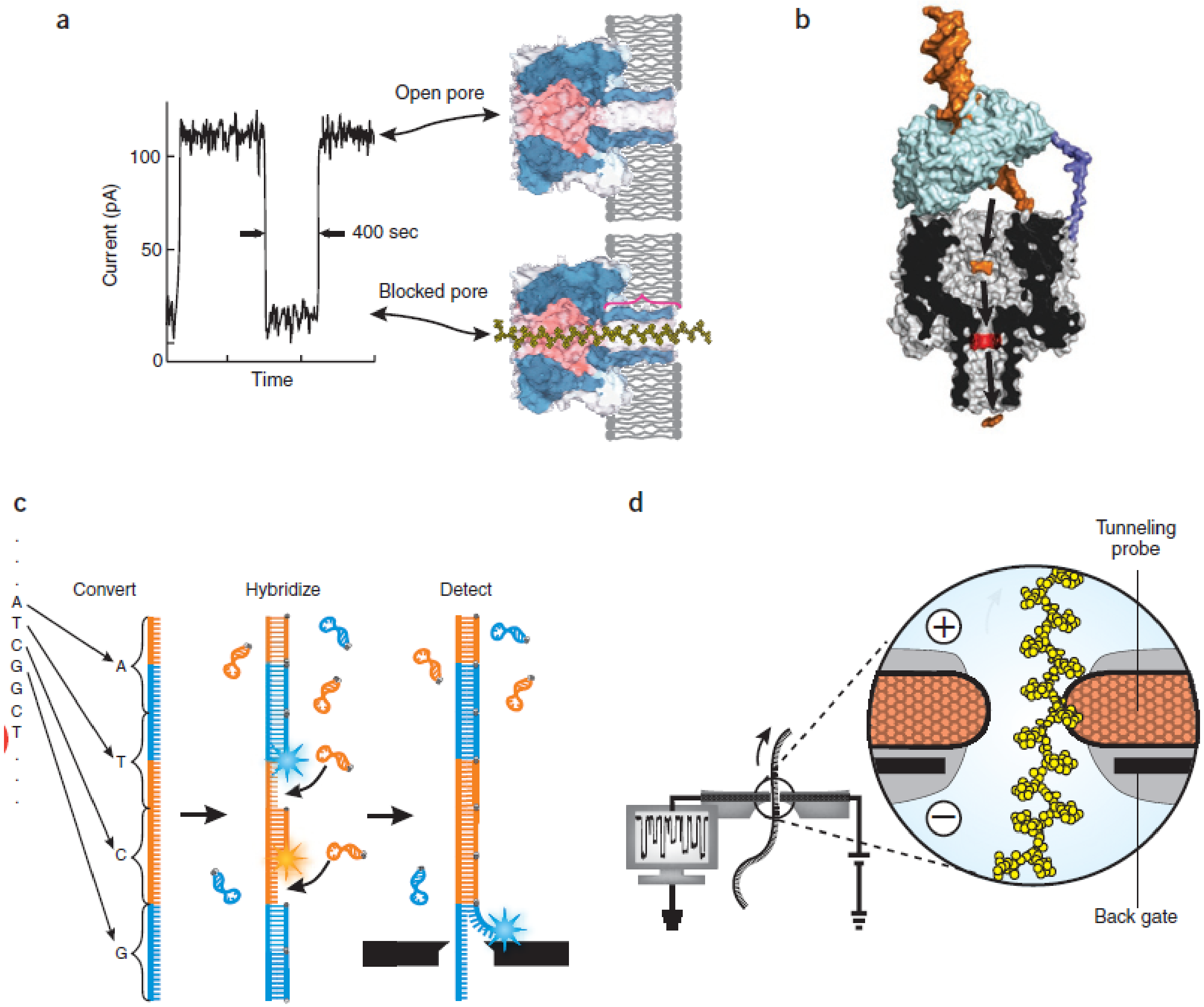
a
Current (pA)
100
50
0
Time
400 sec
Open pore
Blocked pore
b
c
A
T
C
G
G
C
T
Convert
Hybridize
Detect
A
T
C
G
d
Tunneling probe
Back gate
+
−

Cell Free DNA (cfDNA)

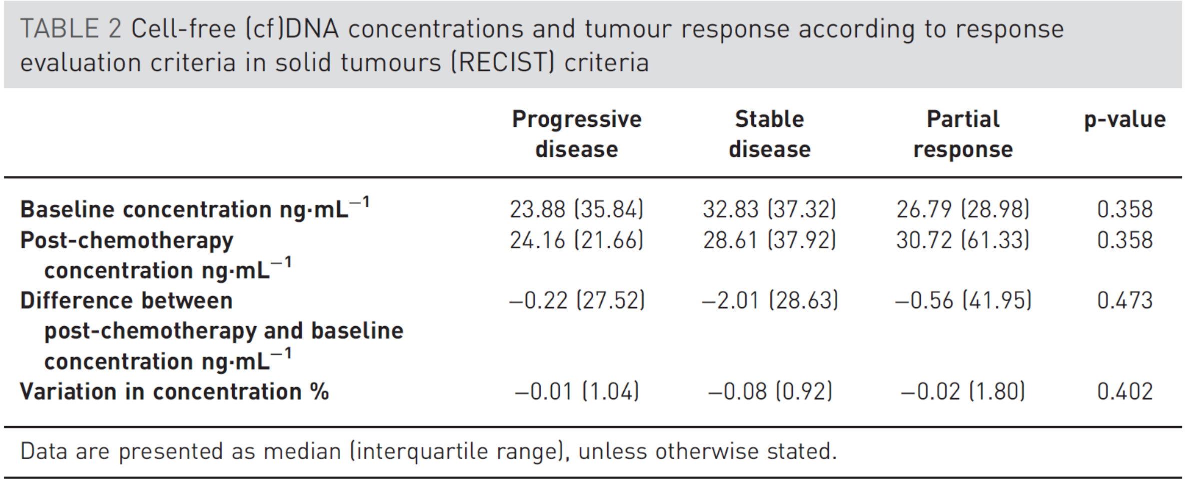

TABLE 2 Cell-free (cf)DNA concentrations and tumour response according to response evaluation criteria in solid tumours (RECIST) criteria

	Progressive disease	Stable disease	Partial response	p-value
Baseline concentration ng·mL^{-1}	23.88 (35.84)	32.83 (37.32)	26.79 (28.98)	0.358
Post-chemotherapy concentration ng·mL^{-1}	24.16 (21.66)	28.61 (37.92)	30.72 (61.33)	0.358
Difference between post-chemotherapy and baseline concentration ng·mL^{-1}	−0.22 (27.52)	−2.01 (28.63)	−0.56 (41.95)	0.473
Variation in concentration %	−0.01 (1.04)	−0.08 (0.92)	−0.02 (1.80)	0.402

Data are presented as median (interquartile range), unless otherwise stated.

0.01%-90% circulating tumor DNA (ctDNA)

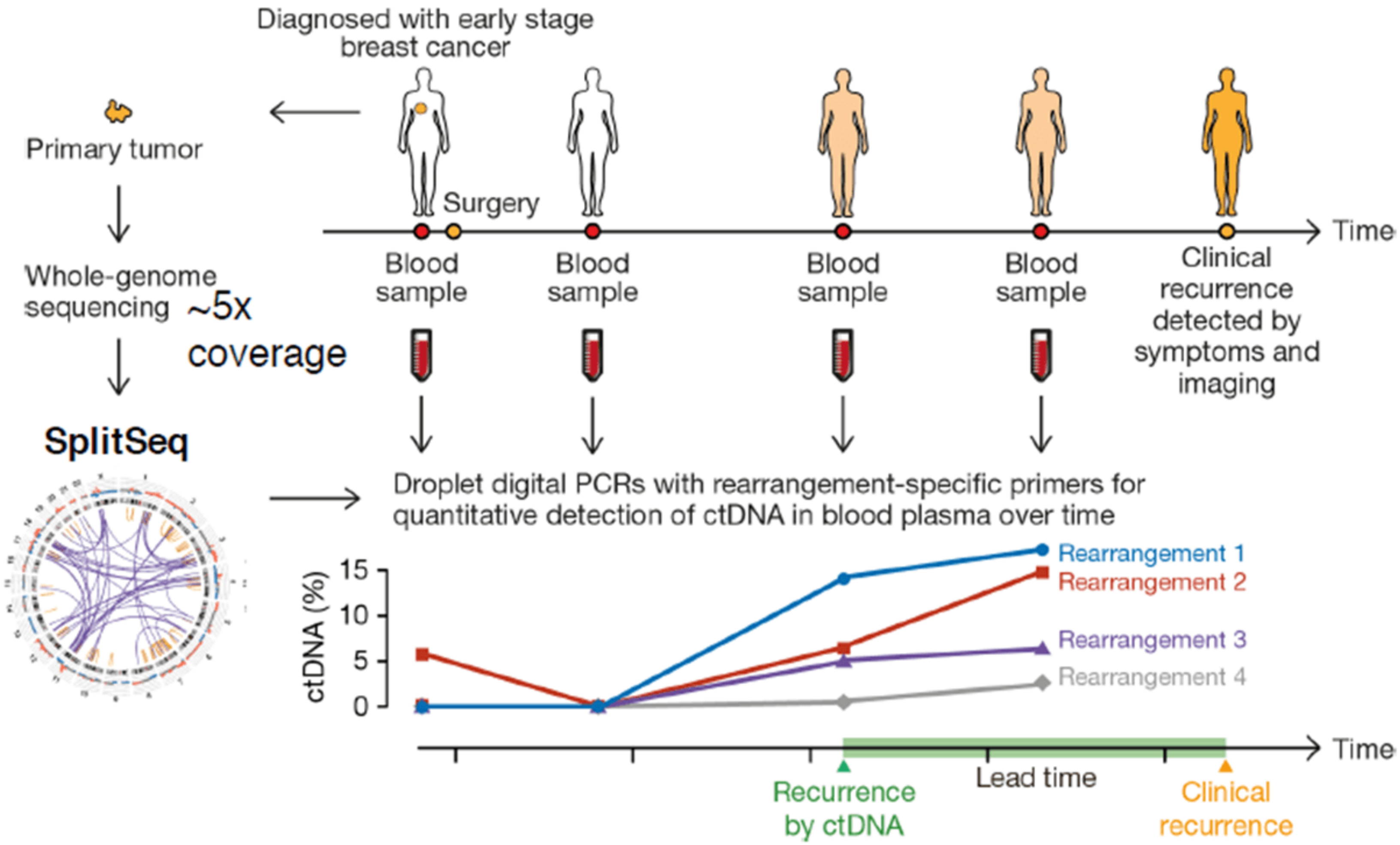

Diagnosed with early stage breast cancer

Primary tumor

Whole-genome sequencing ~5x coverage

SplitSeq

Surgery

Blood sample

Blood sample

Blood sample

Blood sample

Clinical recurrence detected by symptoms and imaging

Time

Droplet digital PCRs with rearrangement-specific primers for quantitative detection of ctDNA in blood plasma over time

Digital PCR

Droplet digital PCR

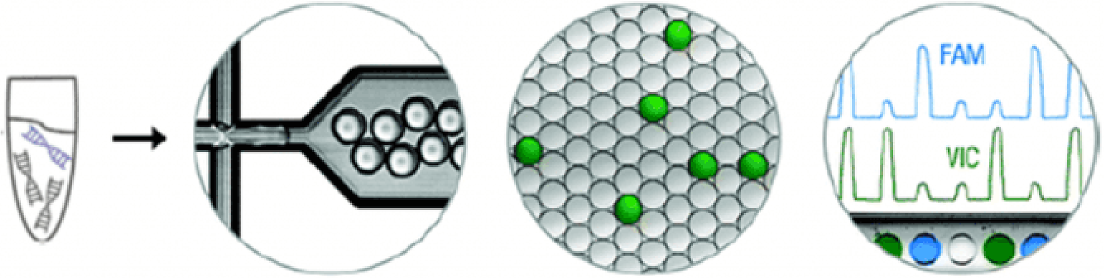

Bio-Rad QX100

1. MAKE

Sample is partitioned into 20,000 droplets

2. CYCLE

Run PCR cycles in all droplets simultaneously

3. READ

Measure fluorescence intensity in each droplet

Calculate concentration from number of positive droplets

Towards precision medicine

Euan A. Ashley

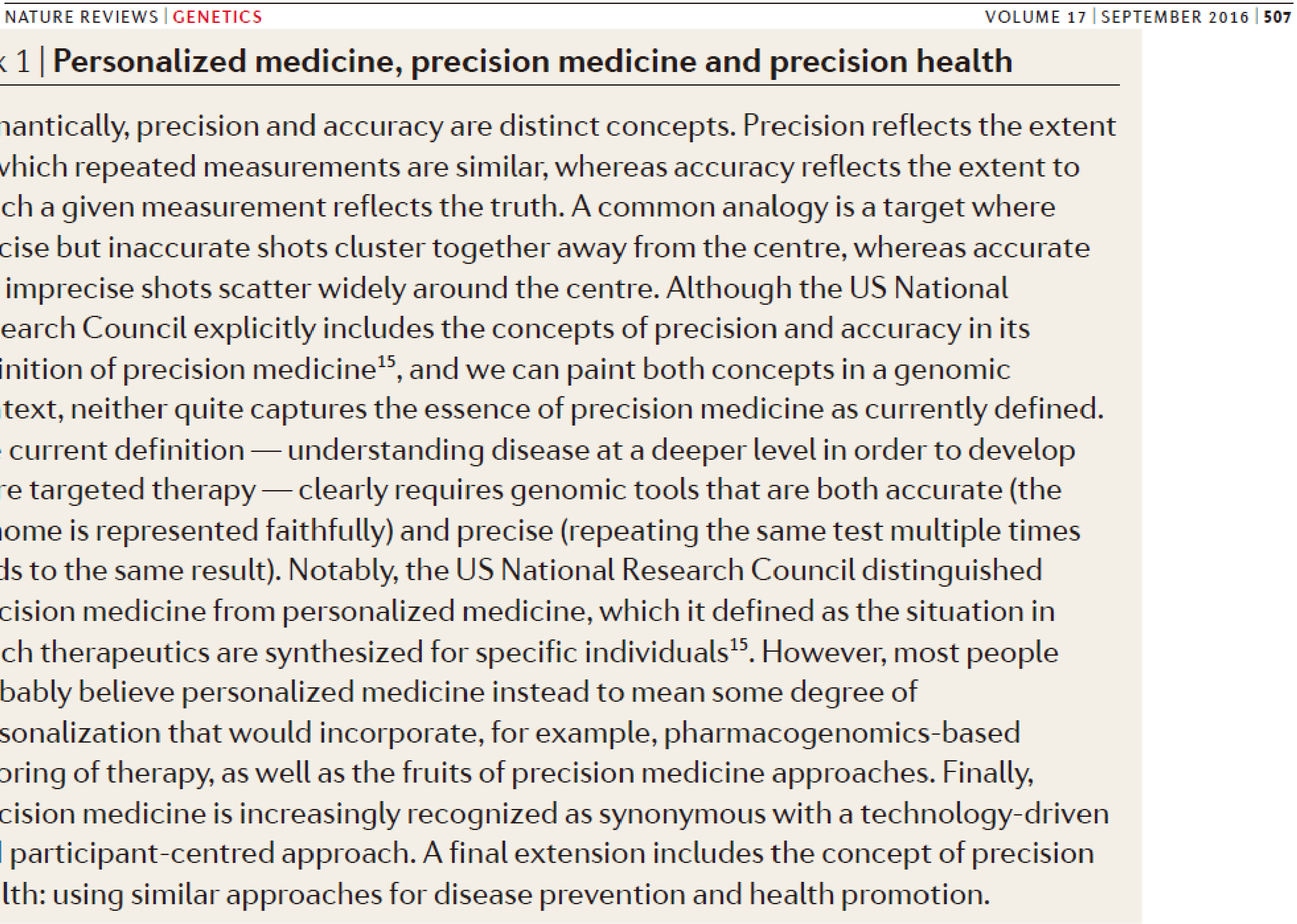

NATURE REVIEWS | GENETICS VOLUME 17 | SEPTEMBER 2016 | 507

Box 1 | **Personalized medicine, precision medicine and precision health**

Semantically, precision and accuracy are distinct concepts. Precision reflects the extent to which repeated measurements are similar, whereas accuracy reflects the extent to which a given measurement reflects the truth. A common analogy is a target where precise but inaccurate shots cluster together away from the centre, whereas accurate but imprecise shots scatter widely around the centre. Although the US National Research Council explicitly includes the concepts of precision and accuracy in its definition of precision medicine[15], and we can paint both concepts in a genomic context, neither quite captures the essence of precision medicine as currently defined. The current definition — understanding disease at a deeper level in order to develop more targeted therapy — clearly requires genomic tools that are both accurate (the genome is represented faithfully) and precise (repeating the same test multiple times leads to the same result). Notably, the US National Research Council distinguished precision medicine from personalized medicine, which it defined as the situation in which therapeutics are synthesized for specific individuals[15]. However, most people probably believe personalized medicine instead to mean some degree of personalization that would incorporate, for example, pharmacogenomics-based tailoring of therapy, as well as the fruits of precision medicine approaches. Finally, precision medicine is increasingly recognized as synonymous with a technology-driven and participant-centred approach. A final extension includes the concept of precision health: using similar approaches for disease prevention and health promotion.

The current definition — understanding disease at a deeper level in order to develop more targeted therapy — clearly requires genomic tools that are both accurate (the genome is represented faithfully) and precise (repeating the same test multiple times leads to the same result).

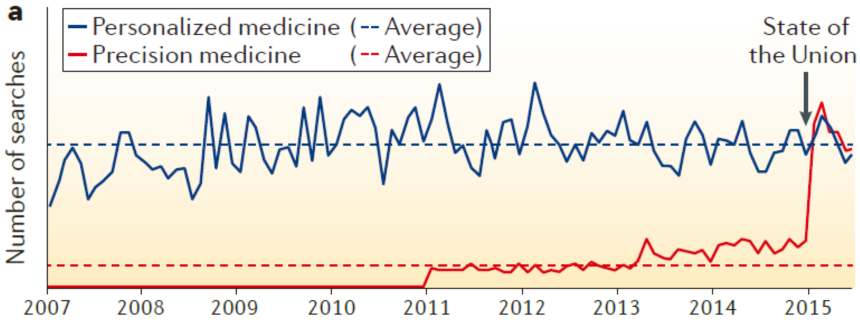

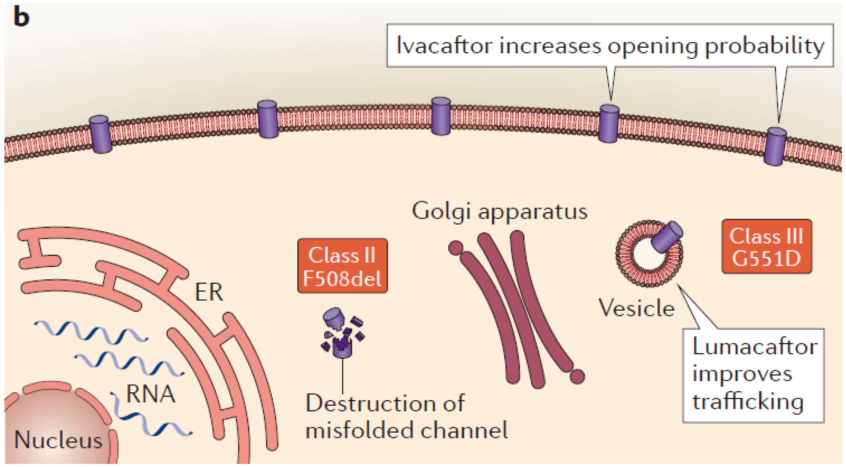

Subcategory	Functional effect	Example variant
I	No functional protein	G542x
II	Trafficking defect	F508del
III	Defective regulation	G551D
IV	Decreased conductance	R117H
V	Reduced synthesis	3120+1G>A
VI	Reduced stability	Q1412x

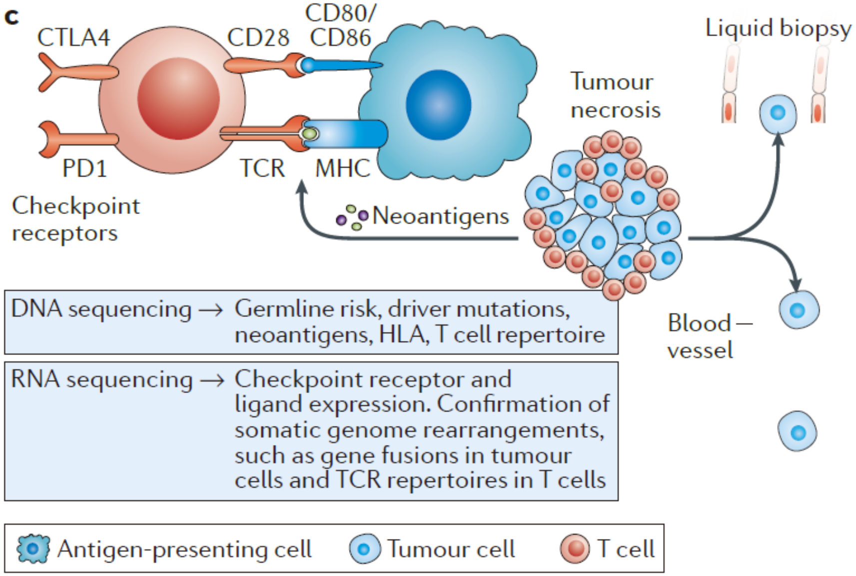

Drug development in the era of precision medicine

NATURE REVIEWS | DRUG DISCOVERY VOLUME 17 | MARCH 2018 | 183

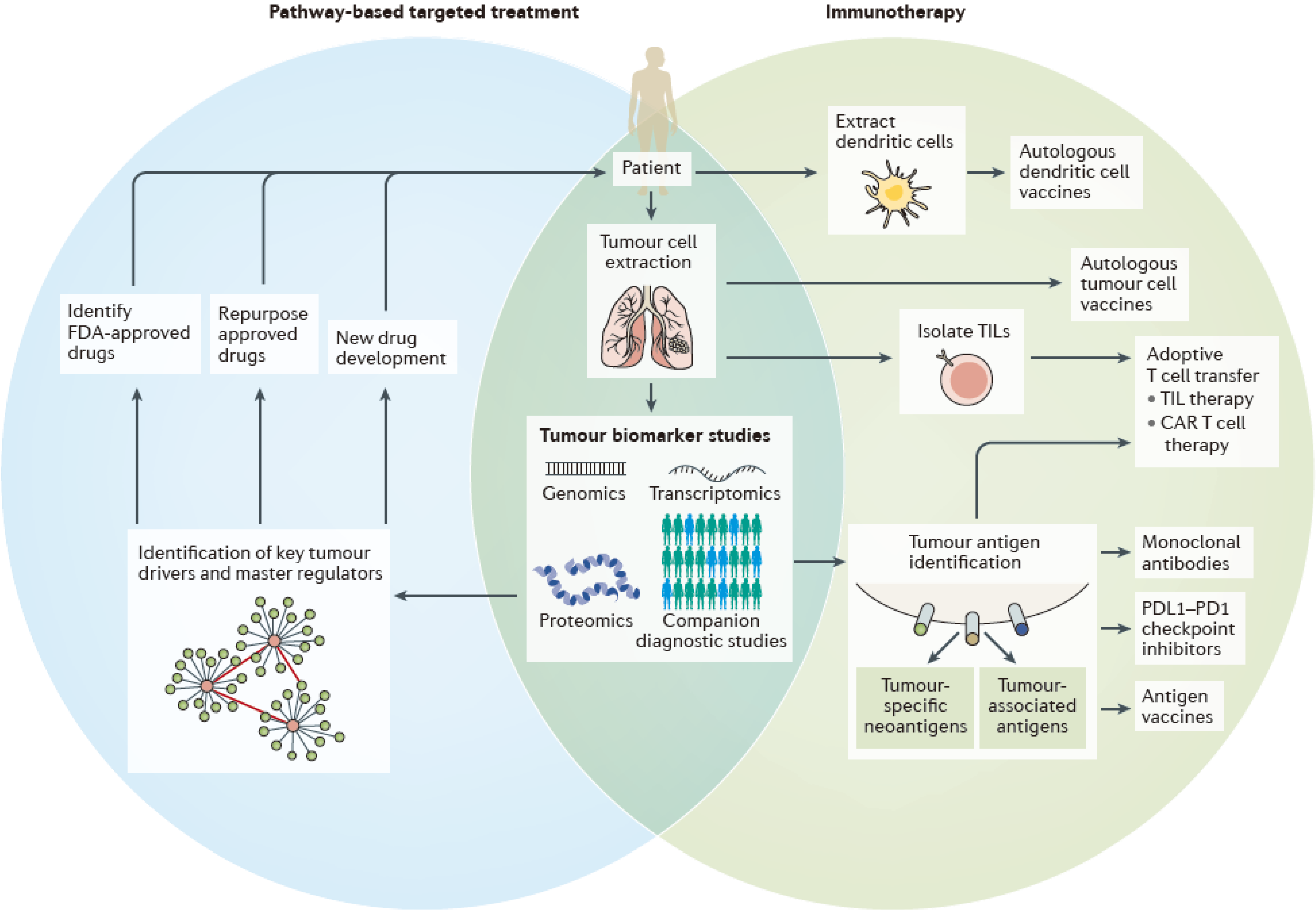

Pathway-based targeted treatment

Immunotherapy

Patient

Identify FDA-approved drugs

Repurpose approved drugs

New drug development

Identification of key tumour drivers and master regulators

Tumour cell extraction

Tumour biomarker studies

Genomics

Transcriptomics

Proteomics

Companion diagnostic studies

Extract dendritic cells

Autologous dendritic cell vaccines

Autologous tumour cell vaccines

Isolate TILs

Adoptive T cell transfer
- TIL therapy
- CAR T cell therapy

Tumour antigen identification

Tumour-specific neoantigens

Tumour-associated antigens

Monoclonal antibodies

PDL1–PD1 checkpoint inhibitors

Antigen vaccines

PROTOCOL OF SARS-COV-2 DETECTION USING REAL-TIME RT-PCR

Target gene → RdRp gene (Corman *et al.* 2020)

PCR amplification regions → nCoV_IP2/12621-12727 and nCoV_IP4/14010-14116 (Institut Pasteur, Paris)

Primer sets and probes → designed based on the first sequences of SARS-CoV-2 available on the GISAID database

RNA extraction → NucleoSpin® RNA Virus or viral RNA mini kit (QIAGEN)

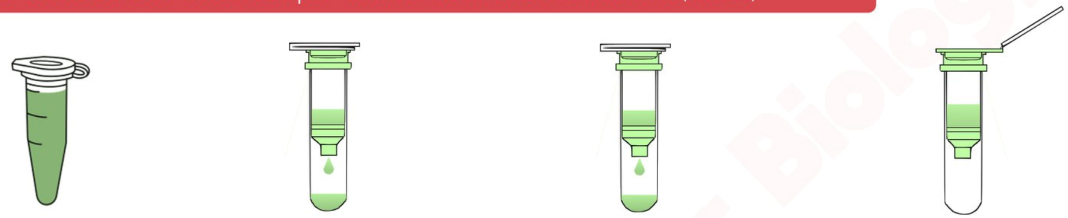

Sample lysis
5 min incubation of sample in Lysis Buffer containing Proteinase K

Binding of viral RNA
Ethanol addition and transfer of lysate to Column

Washing
1st Wash Buffer (high salt concentration)
2nd Wash Buffer (low salt concentration)

Elution of viral RNA
Elution in 20-50 µl RNase-free water or Elution Buffer

Real-time Multiplex RT-PCR (Institut Pasteur, Paris)

Multiplex Mix (nCoV_IP2&IP4)

Sample RNA	5 µl
H2O	1.3 µl
Reaction mix 2X	12.50 µl
MgSO4 (50mM)	0.40 µl
Forward Primer1 (10µM)	1.00 µl
Reverse Primer1 (10µM)	1.00 µl
Forward Primer2 (10µM)	1.00 µl
Reverse Primer2 (10µM)	1.00 µl
Probe 1 (10µM)	0.4 µl
Probe 2 (10µM)	0.4 µl
SuperscriptIII RT/Platinum Taq Mix	1.00 µl

Amplification Cycles (Lightcycler System)

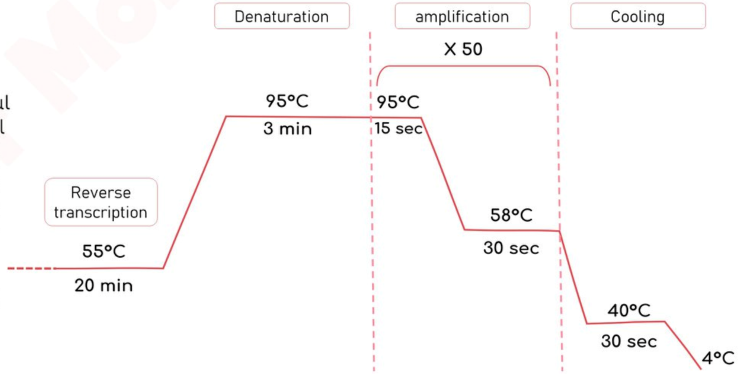

POSITIVE CONTROL

Positive control for real-time RT-PCR is the in vitro transcribed RNA derived from strain BetaCoV_Wuhan_WIV04_2019. The transcript contains the **amplification regions** of the RdRp and E gene as positive strand.

M. MERZOUG

References

1. Institut Pasteur, Paris, « Protocol: Real-time RT-PCR assays for the detection of SARS-CoV-2 », OMS, 2 mars 2020.
2. Corman VM, Landt O, Kaiser M, et al. Detection of 2019 novel coronavirus (2019-nCoV) by real-time RT-PCR. Euro Surveill 2020;25.

1 hour
Known primer

Hematology Analyzer

WBC	White Blood Cell or leukocyte count
RBC	Red Blood Cell or erythrocyte count
Hgb	Hemoglobin concentration
Hct	Hematocrit (relative volume of erythrocytes)
MCV	Mean Corpuscular (erythrocyte) Volume
MCH	Mean Corpuscular (erythrocyte) Hemoglobin
MCHC	Mean Corpuscular (erythrocyte) Hemoglobin Concentration
RDW	Red Cell (erythrocyte volume) Distribution Width
RDW-SD	Red Cell (erythrocyte volume) Distribution Width (Standard Deviation)
Plt	Platelet or thrombocyte count
MPV	Mean Platelet (thrombocyte) Volume
LY%	Lymphocyte percent
MO%	Monocyte percent
NE%	Neutrophil percent
EO%	Eosinophil percent
BA%	Basophil percent
LY#	Lymphocyte number
MO#	Monocyte number
NE#	Neutrophil number
EO#	Eosinophil number
BA#	Basophil number
NRBC%	Nucleated Red Blood Cell percent
NRBC#	Nucleated Red Blood Cell number
RET%	Reticulocyte percent
RET#	Reticulocyte number
IRF	Immature Reticulocyte Fraction
MRV	Mean Reticulocyte Volume

Chemistry Analyzer

No.	Test Name	Long Name
1	ALB	Albumin
2	ALP	Alkaline Phosphatase
3	ALT	Alanine Transferase
4	AMY	Amylase
5	AST	AspartateTransferase
6	CO2	Bicarbonate
7	DBILC	Direct Bilirubin
8	DBB	DirectBilirubinBlank
9	TBILC	Total Bilirubin
10	TBB	TotalBilirubinBlank
11	CA	Calcium Arsenazo
12	NDBILI	Direct Bili - 181
13	CHOL	Cholesterol
14	AMMON	Ammonia
15		
16	CK	CreatPhosphoKinase
17	CRE	Creatinine
18	GGT	Gamma Glutamyl Trans
19	GLU	Glucose

Protein Microarray

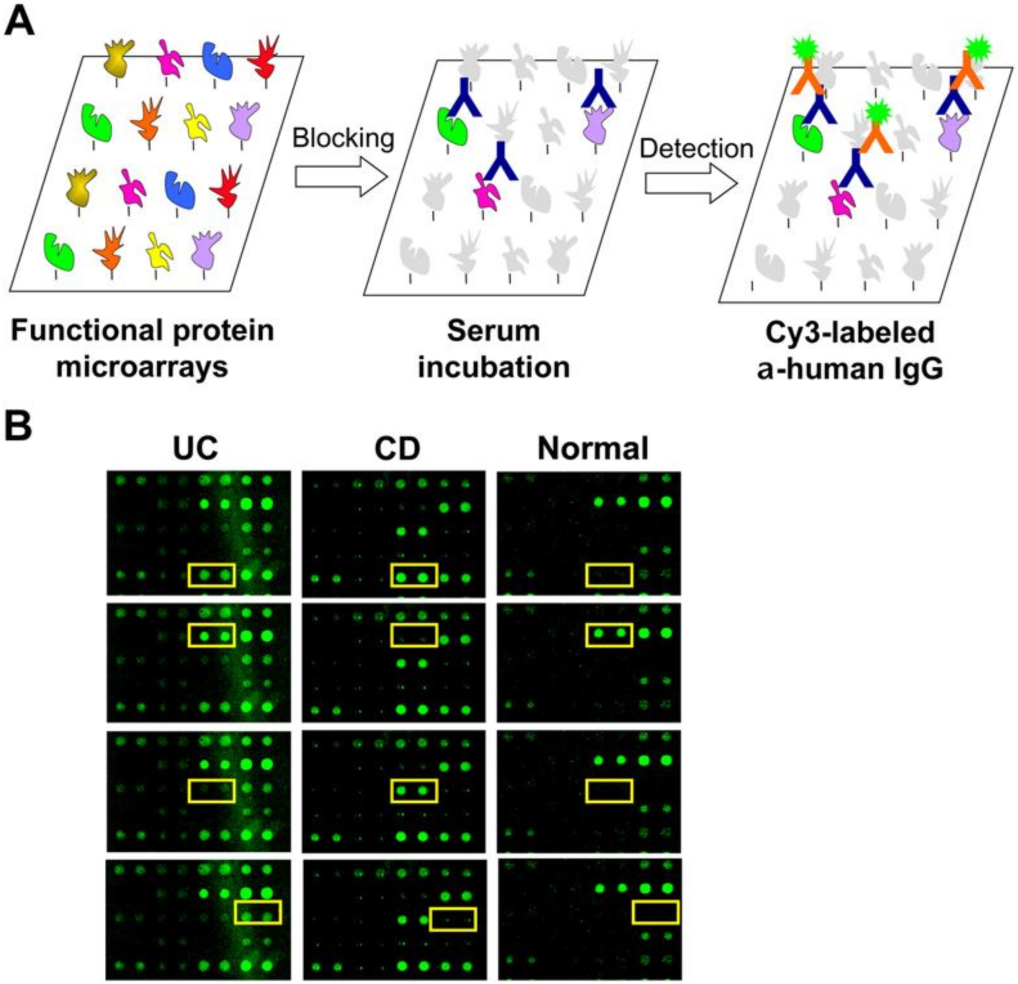

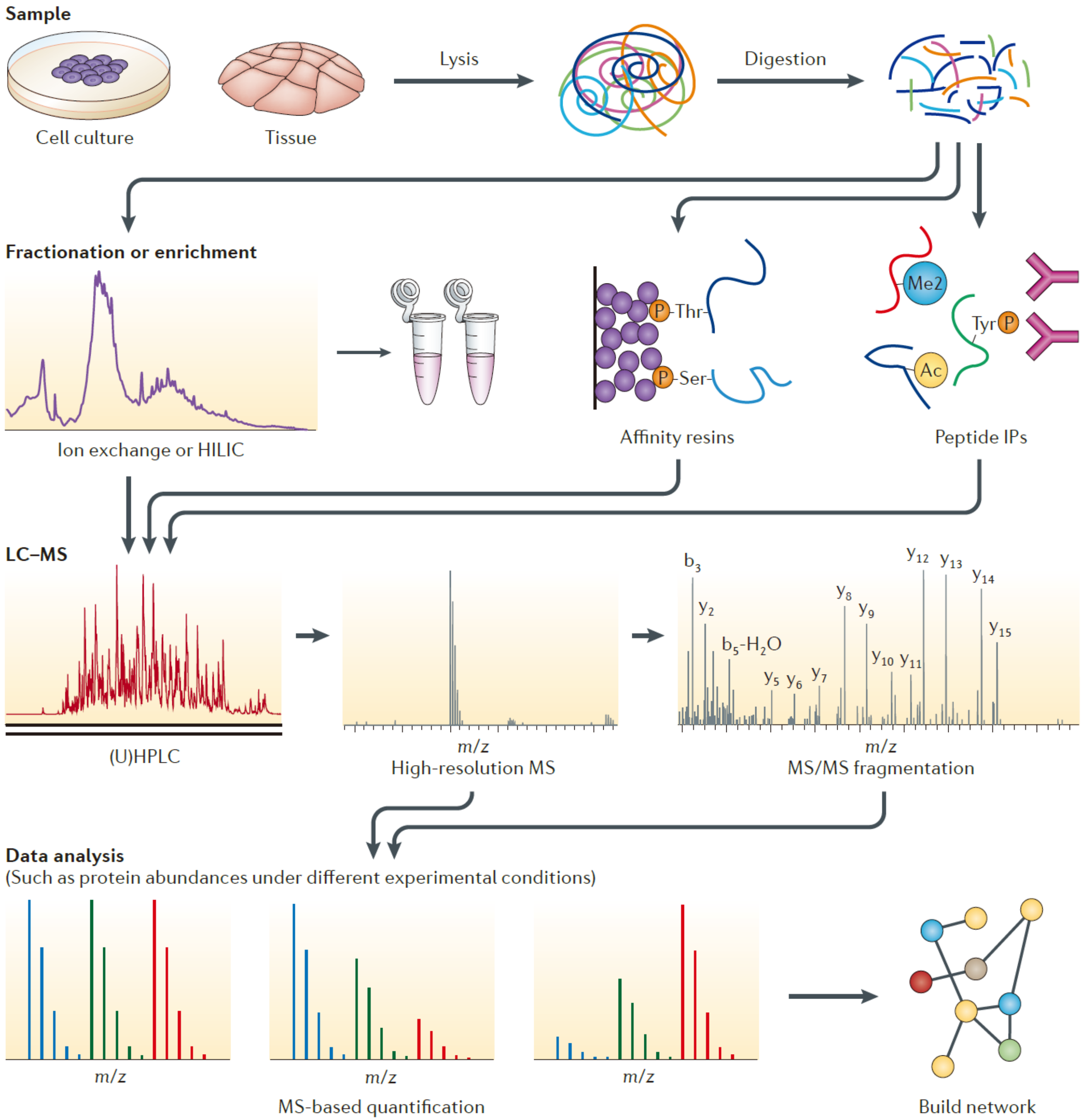
Sample
Cell culture
Tissue
Lysis
Digestion
Fractionation or enrichment
Ion exchange or HILIC
P
Thr
P
Ser
Affinity resins
Me2
Tyr
P
Ac
Peptide IPs
LC–MS
(U)HPLC
m/z
High-resolution MS
b3
y2
b5-H2O
y5
y6
y7
y8
y9
y10
y11
y12
y13
y14
y15
m/z
MS/MS fragmentation
Data analysis
(Such as protein abundances under different experimental conditions)
m/z
m/z
m/z
MS-based quantification
Build network

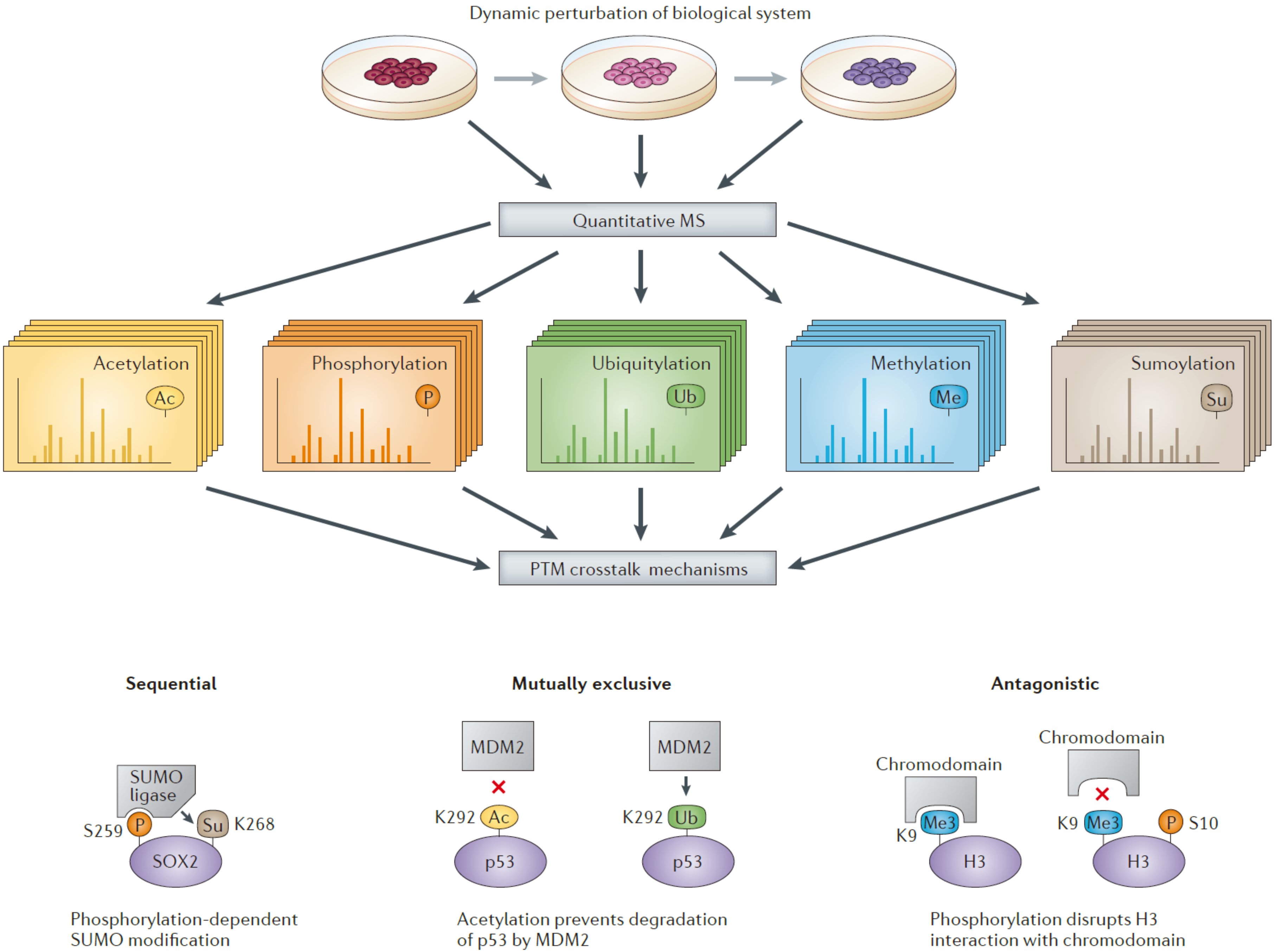
Dynamic perturbation of biological system
Quantitative MS
Acetylation
Ac
Phosphorylation
P
Ubiquitylation
Ub
Methylation
Me
Sumoylation
Su
PTM crosstalk mechanisms
Sequential
SUMO ligase
S259
P
Su
K268
SOX2
Phosphorylation-dependent SUMO modification
Mutually exclusive
MDM2
K292
Ac
p53
MDM2
K292
Ub
p53
Acetylation prevents degradation of p53 by MDM2
Antagonistic
Chromodomain
K9
Me3
H3
Chromodomain
K9
Me3
P
S10
H3
Phosphorylation disrupts H3 interaction with chromodomain

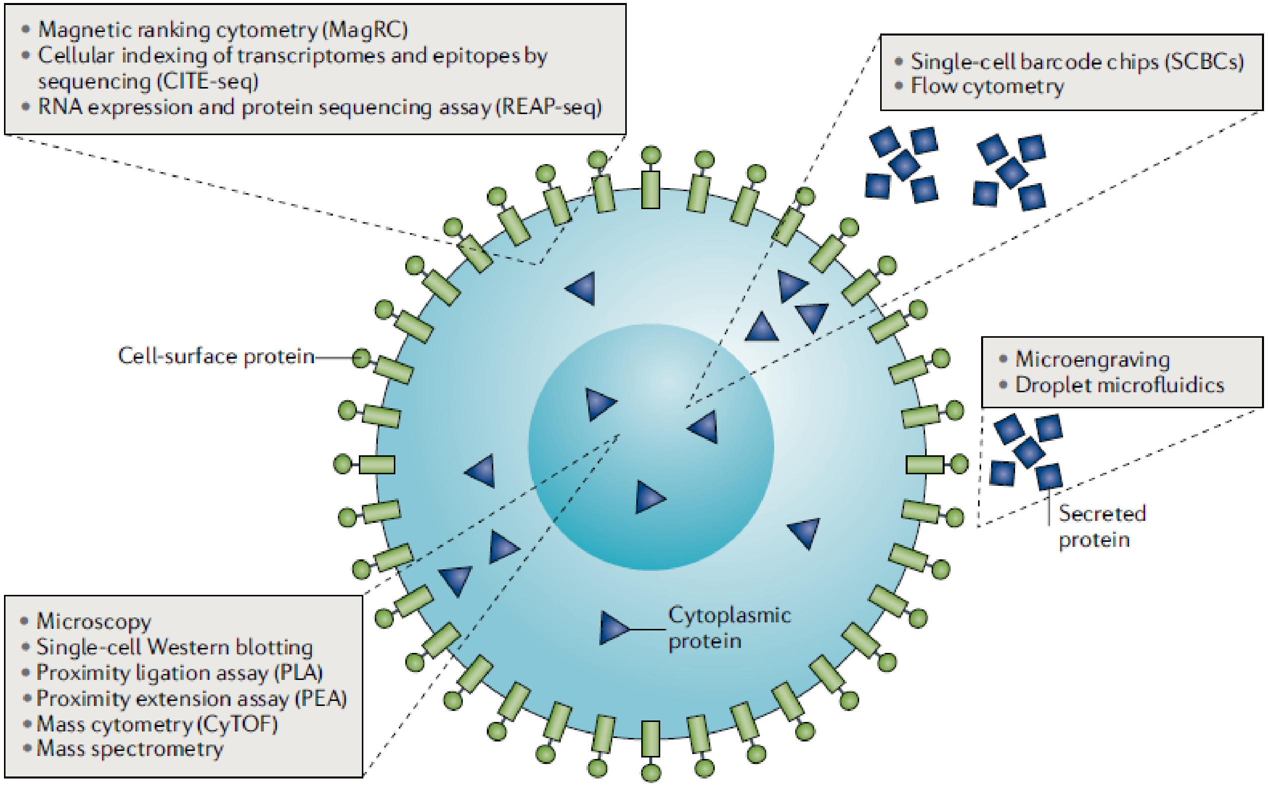

Fig. 1 | **Classification of single-cell protein analysis methods based on the location of target protein.** Cell-surface-protein analysis methods include magnetic ranking cytometry (MagRC), cellular indexing of transcriptomes and epitopes by sequencing (CITE-seq), and RNA expression and protein sequencing assay (REAP-seq). Methods that can be used for the analysis of cell-surface and cytoplasmic proteins include microscopy, single-cell Western blotting, proximity ligation assay (PLA), proximity extension assay (PEA), mass cytometry (cytometry by time of flight; CyTOF) and mass spectrometry. Methods utilized for secreted-protein analysis include droplet microfluidics and microengraving techniques. Methods used for comprehensive analysis of the three proteins include flow cytometry and single-cell barcode chips (SCBCs).

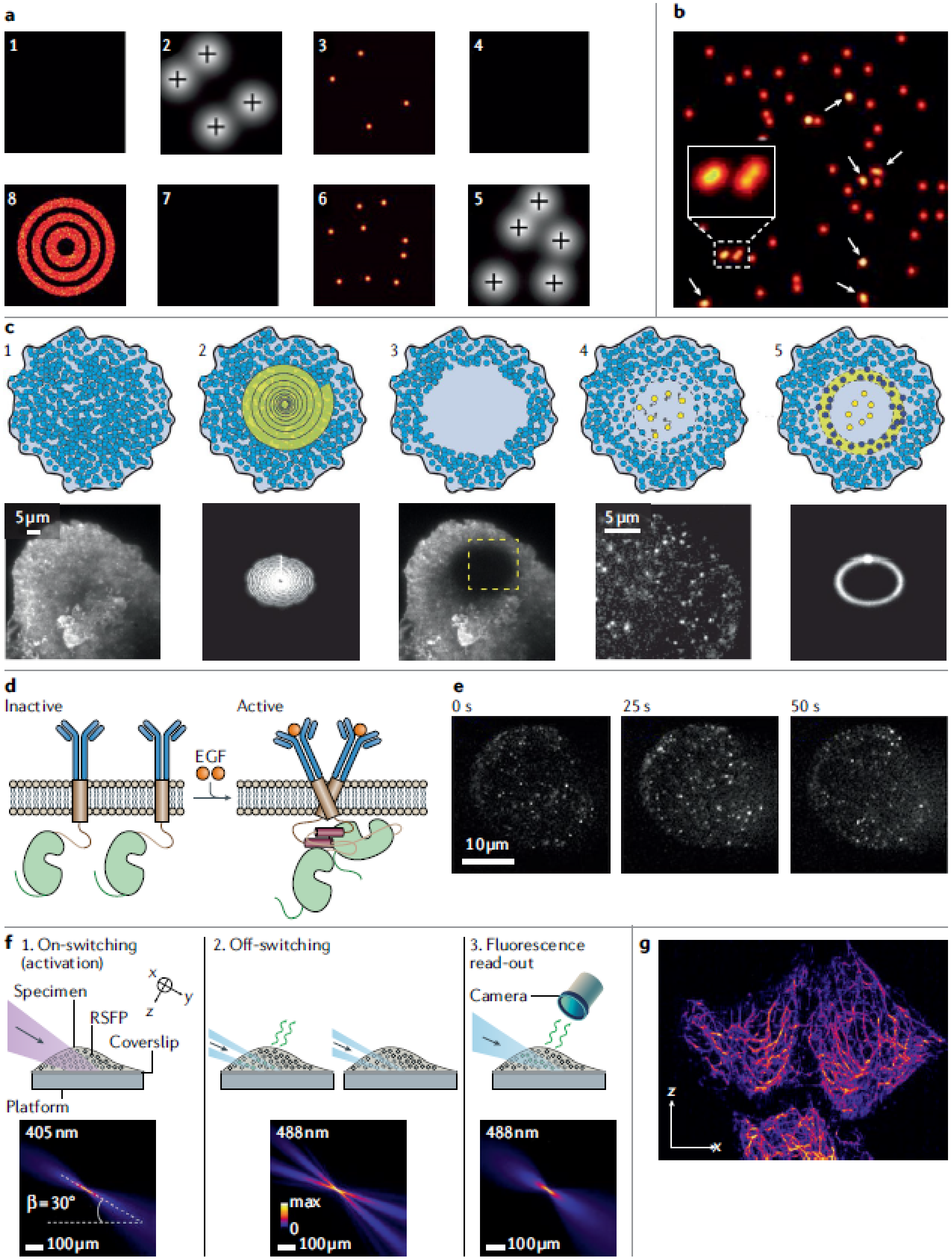
a
1
2
3
4
8
7
6
5
b
c
1
2
3
4
5
5μm
5 μm
d
Inactive
Active
EGF
e
0 s
25 s
50 s
10μm
f
1. On-switching (activation)
Specimen
RSFP
Coverslip
Platform
x
y
z
2. Off-switching
3. Fluorescence read-out
Camera
405 nm
β=30°
100μm
488nm
max
0
100μm
488nm
100μm
g
z
x

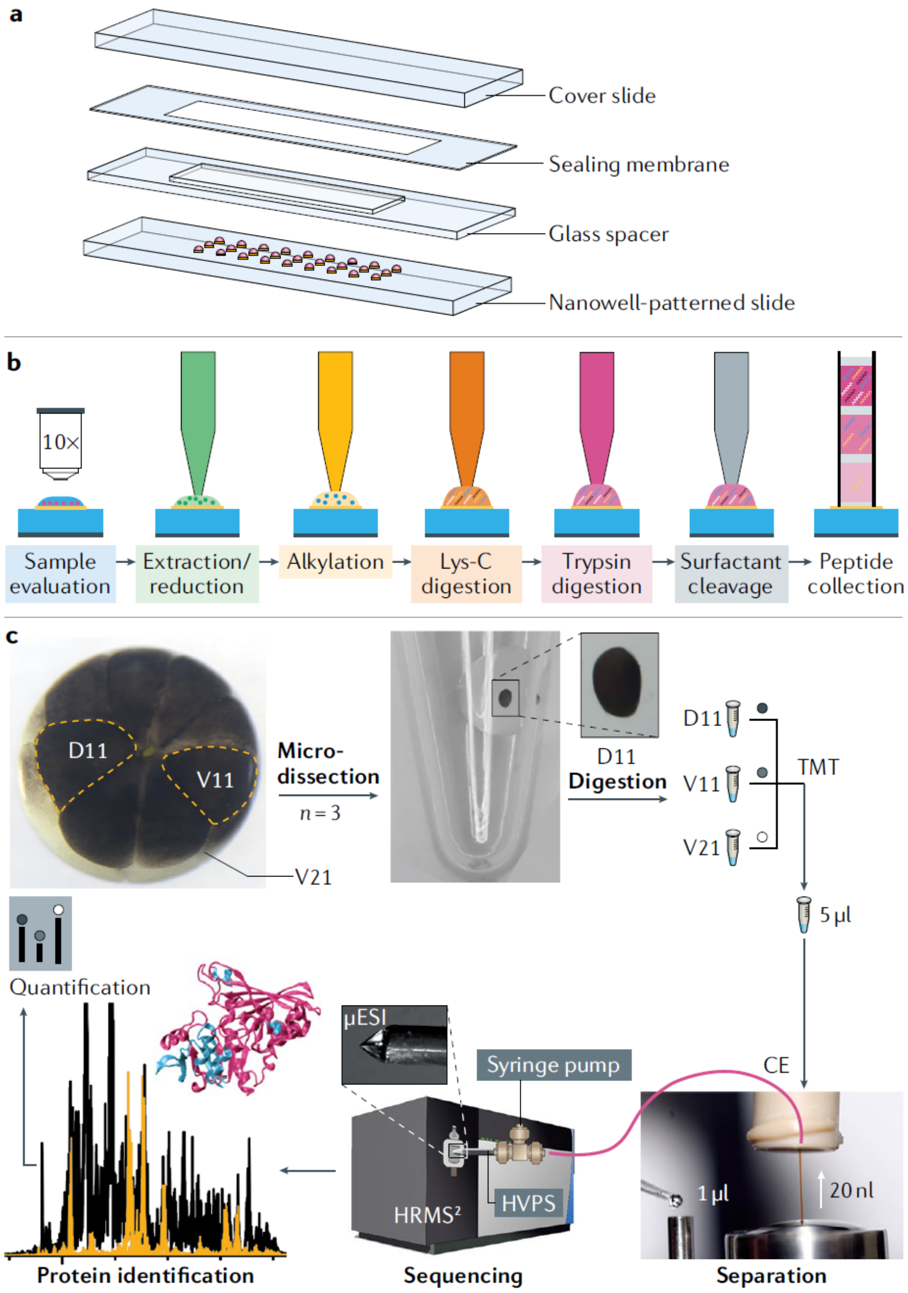
a
Cover slide
Sealing membrane
Glass spacer
Nanowell-patterned slide
b
10×
Sample evaluation
Extraction/ reduction
Alkylation
Lys-C digestion
Trypsin digestion
Surfactant cleavage
Peptide collection
c
D11
V11
V21
Micro-dissection
n = 3
D11
Digestion
D11
V11
V21
TMT
5 μl
CE
Quantification
μESI
Syringe pump
HRMS²
HVPS
1 μl
20 nl
Protein identification
Sequencing
Separation

Flow Cytometry

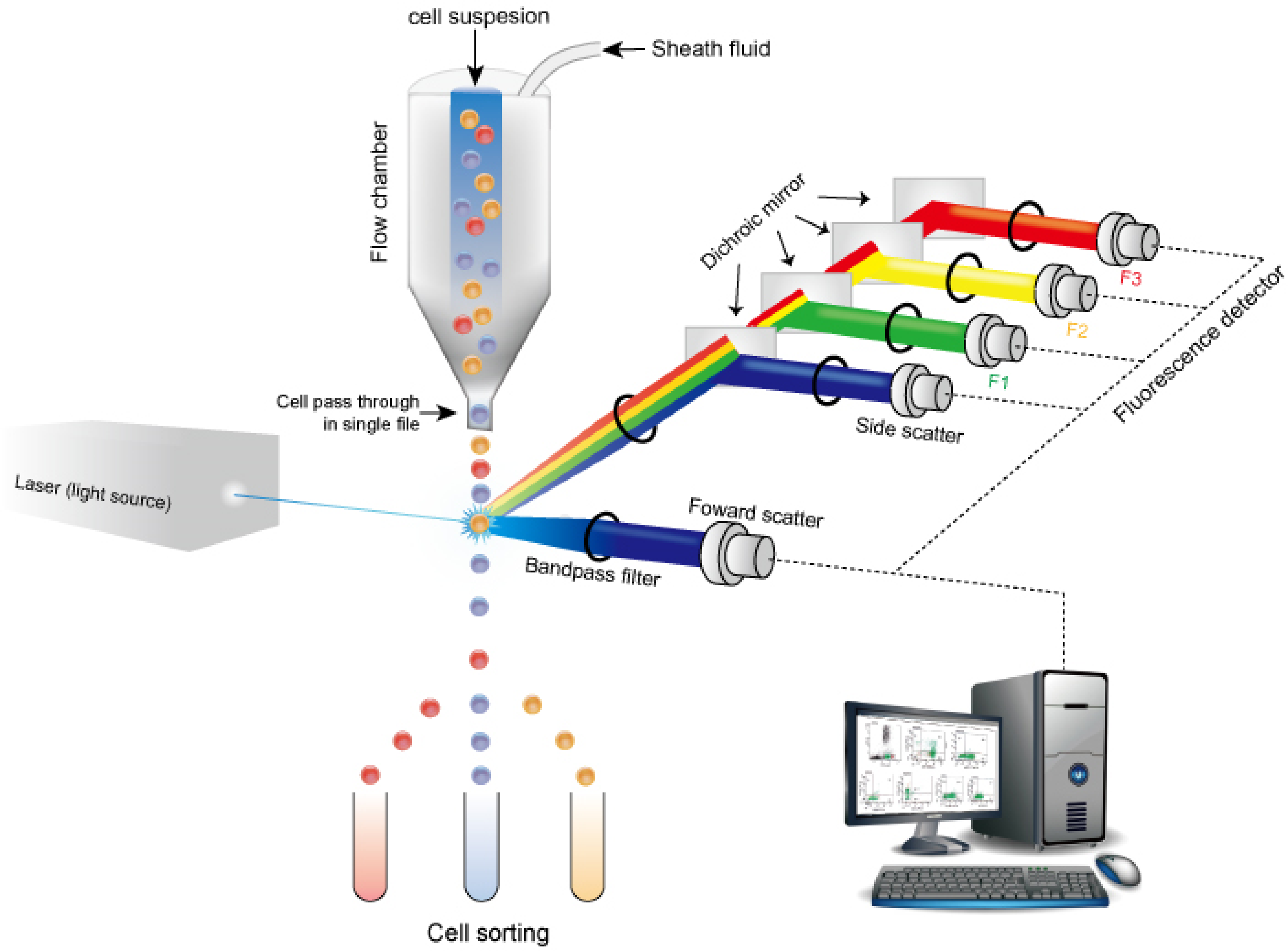

Flow Cytometry Data

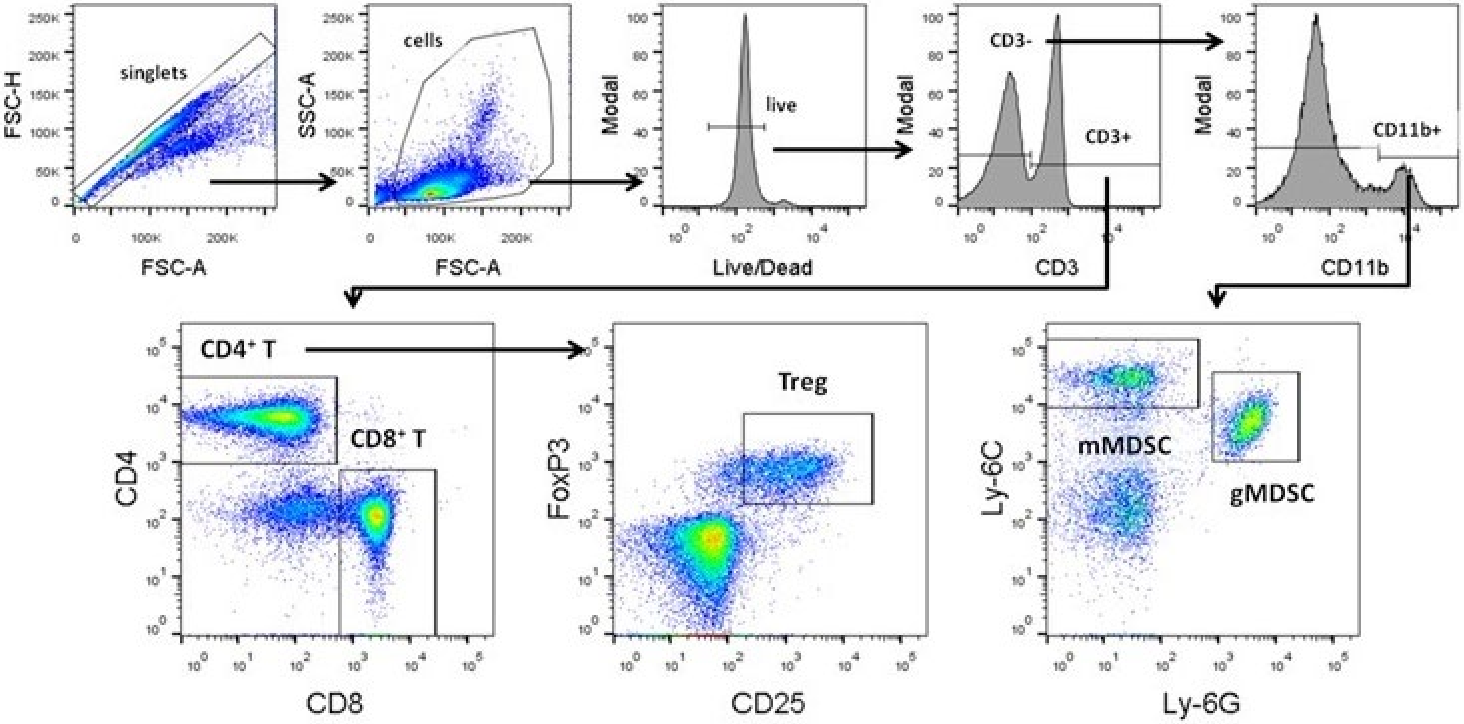

High Content Screening

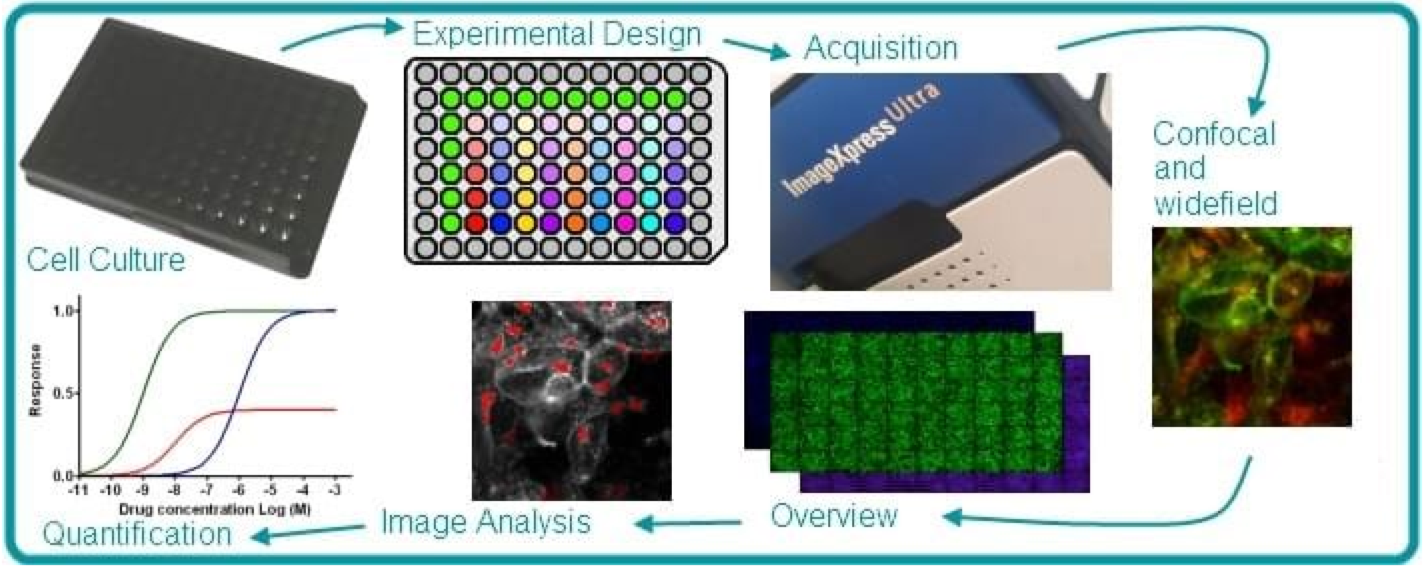

High Content Screening

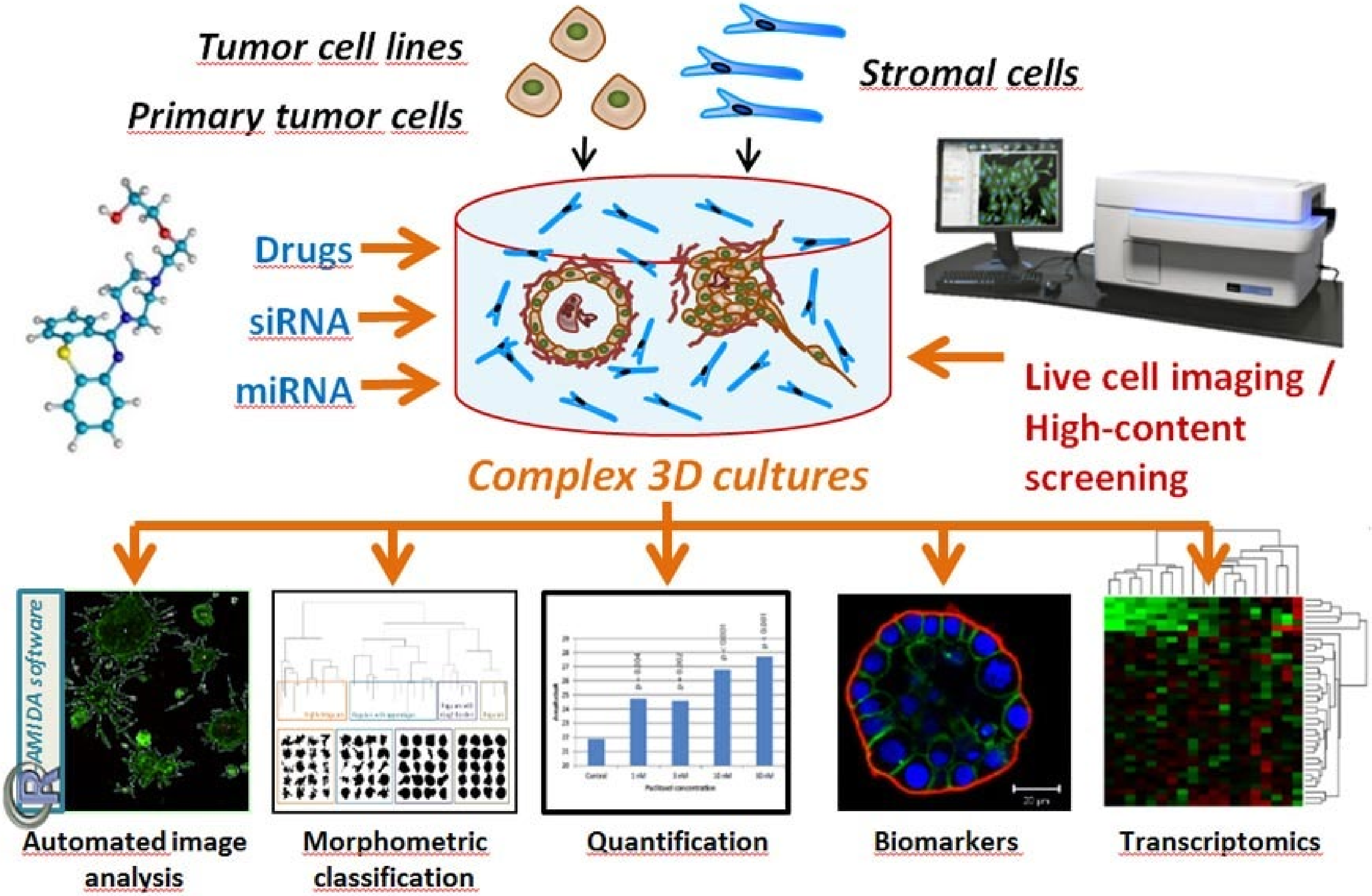

Tumor cell lines

Primary tumor cells

Stromal cells

Drugs

siRNA

miRNA

Live cell imaging / High-content screening

Complex 3D cultures

AMIDA software

Automated image analysis

Morphometric classification

Quantification

Biomarkers

Transcriptomics

Single Cell Analysis

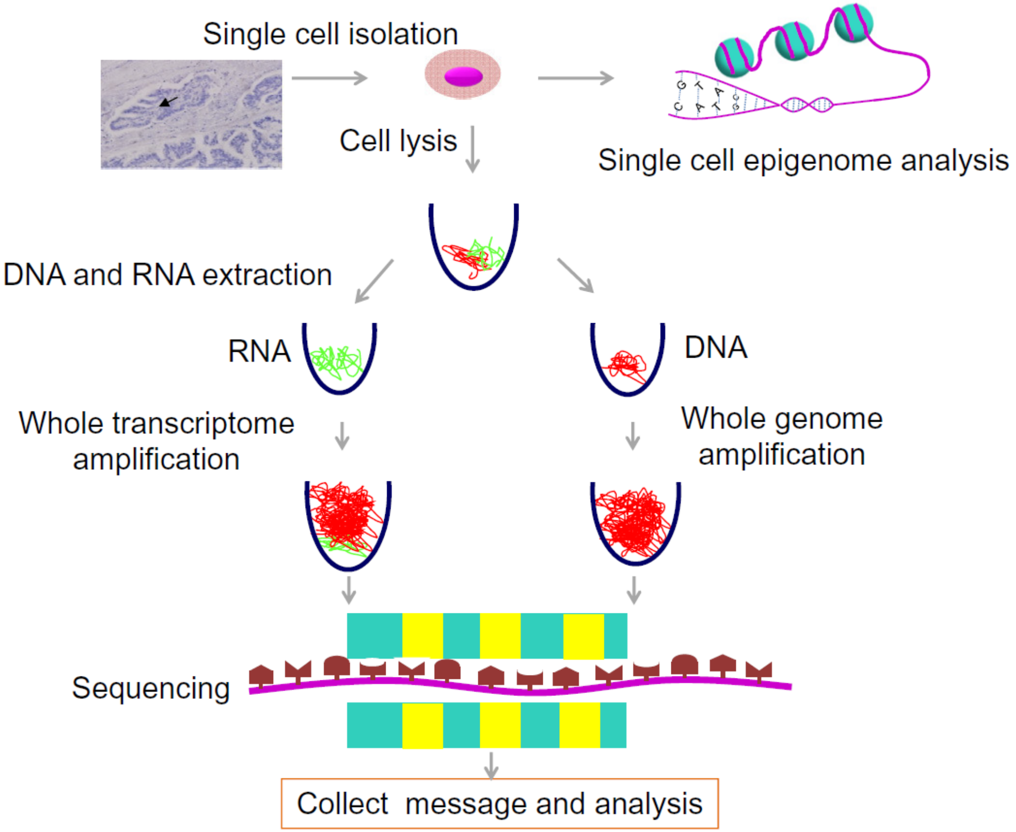

Fig. 1. Single-cell sequencing of a tumor cell. A tumor specimen is obtained by surgical excision and single cells are isolated by one of the several methods shown in Fig. 2. The individual cancer cell can be used for epigenome sequencing directly or lysed to extract the genetic material (DNA and RNA), which is in turn amplified by the methods shown in Fig. 3. Then, the amplified DNA and RNA are sequenced by single-cell sequencing technology and the result data are analyzed to provide insights into the molecular mechanisms underlying intratumor heterogeneity.

Whole Genome Amplifications

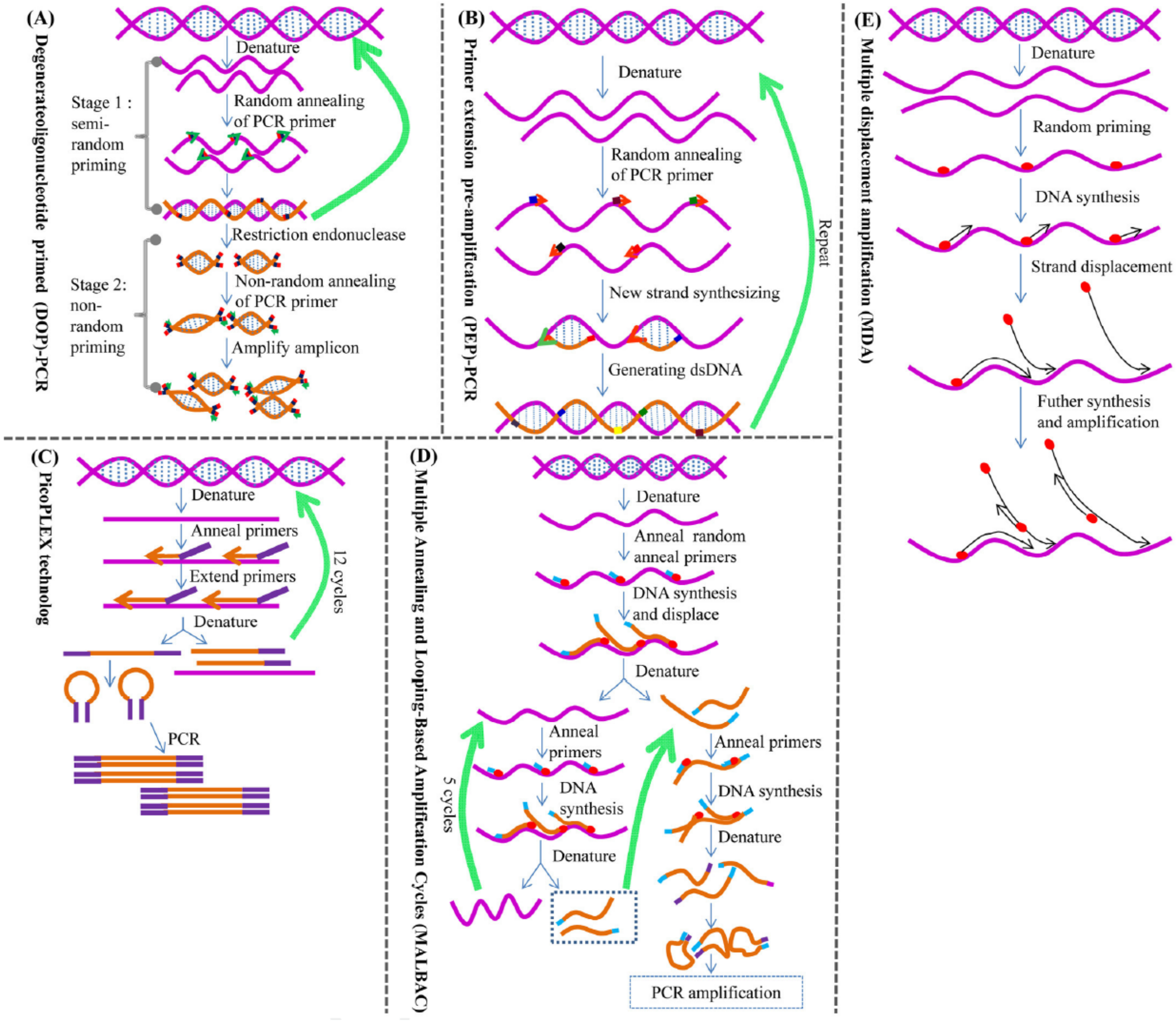

ATAC-seq (**A**ssay for **T**ransposase-**A**ccessible **C**hromatin using **seq**uencing)

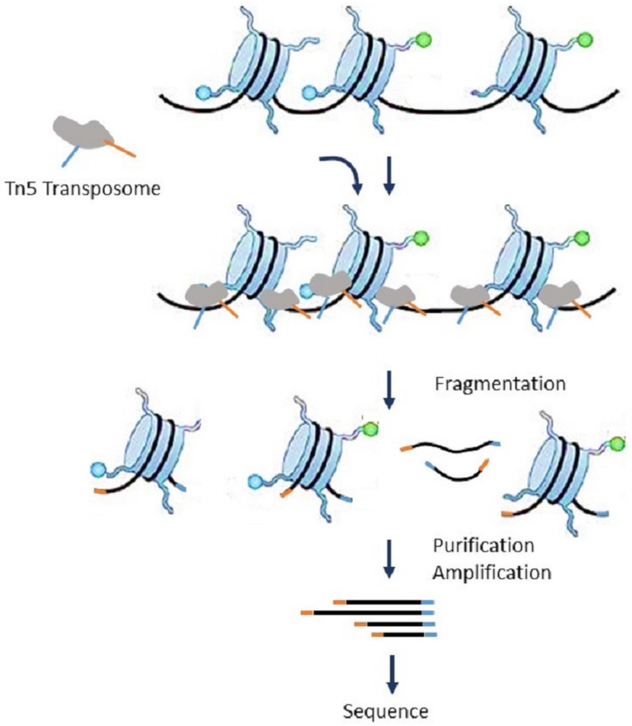

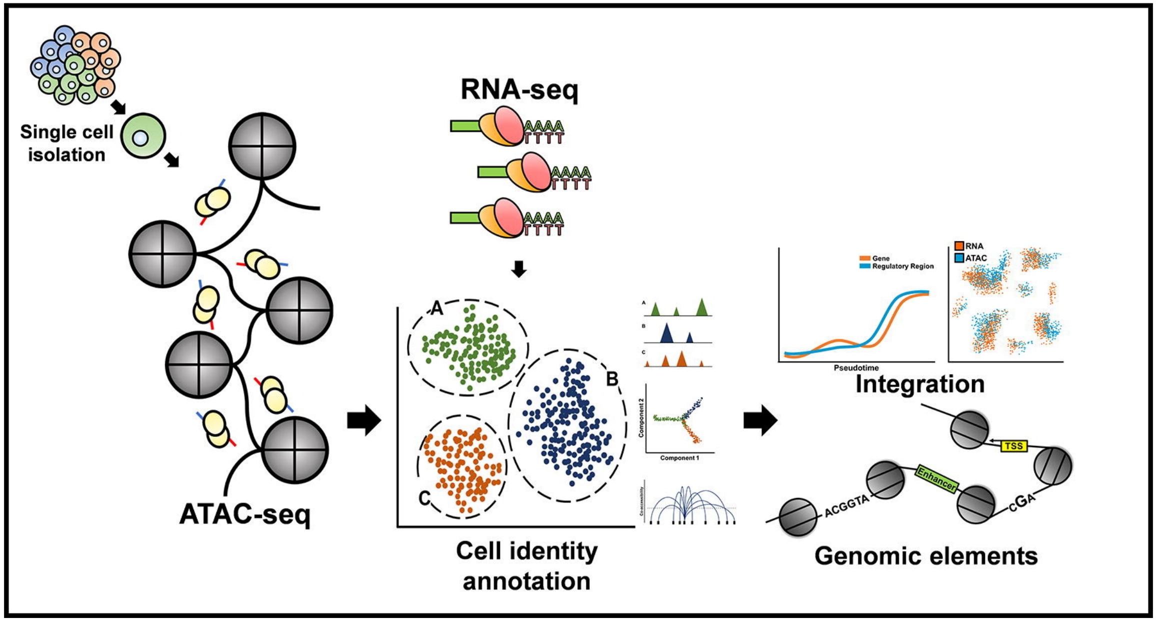

SINGLE-CELL OMICS

Integrative single-cell analysis

Tim Stuart[1] *and Rahul Satija*[1,2]*

Abstract | The recent maturation of single-cell RNA sequencing (scRNA-seq) technologies has coincided with transformative new methods to profile genetic, epigenetic, spatial, proteomic and lineage information in individual cells. This provides unique opportunities, alongside computational challenges, for integrative methods that can jointly learn across multiple types of data. Integrated analysis can discover relationships across cellular modalities, learn a holistic representation of the cell state, and enable the pooling of data sets produced across individuals and technologies. In this Review, we discuss the recent advances in the collection and integration of different data types at single-cell resolution with a focus on the integration of gene expression data with other types of single-cell measurement.

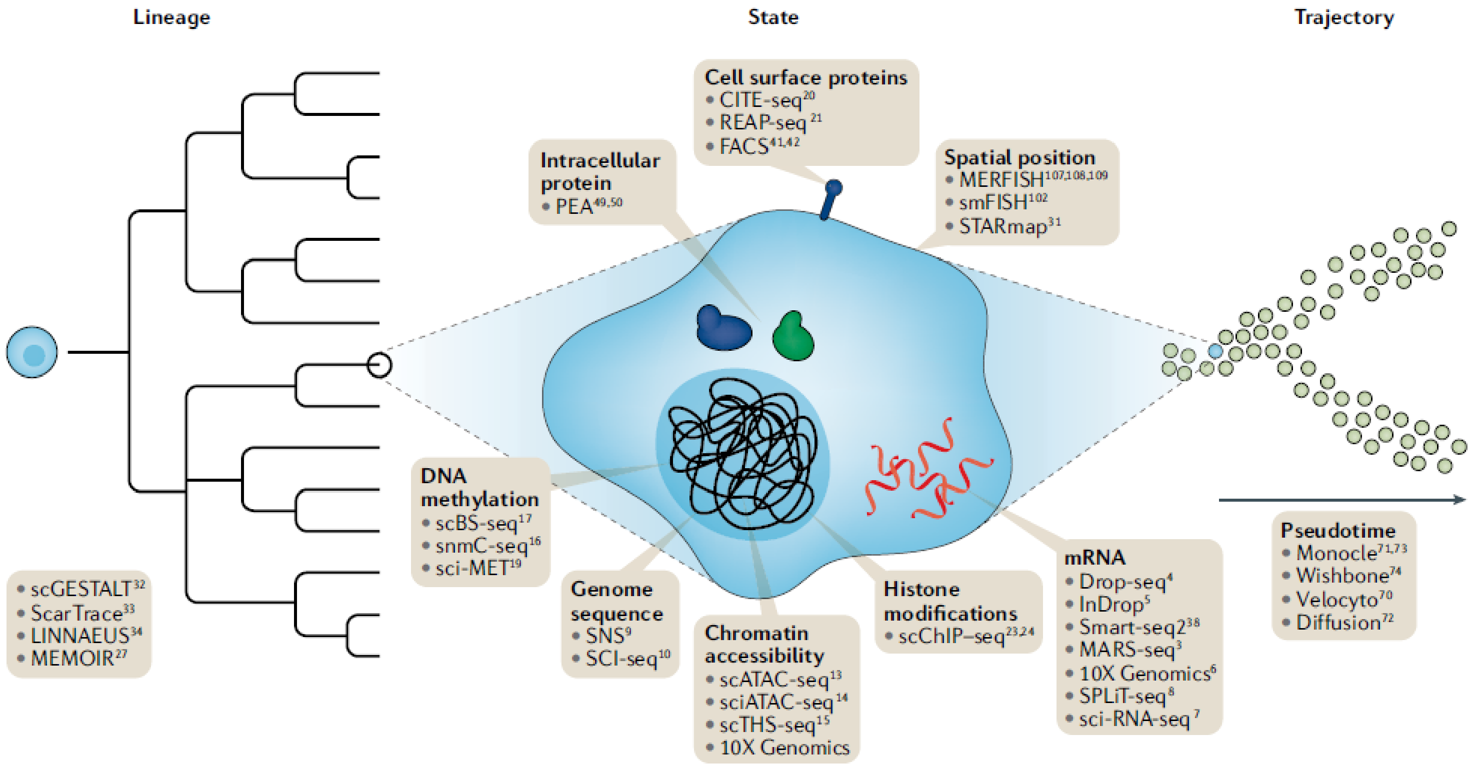

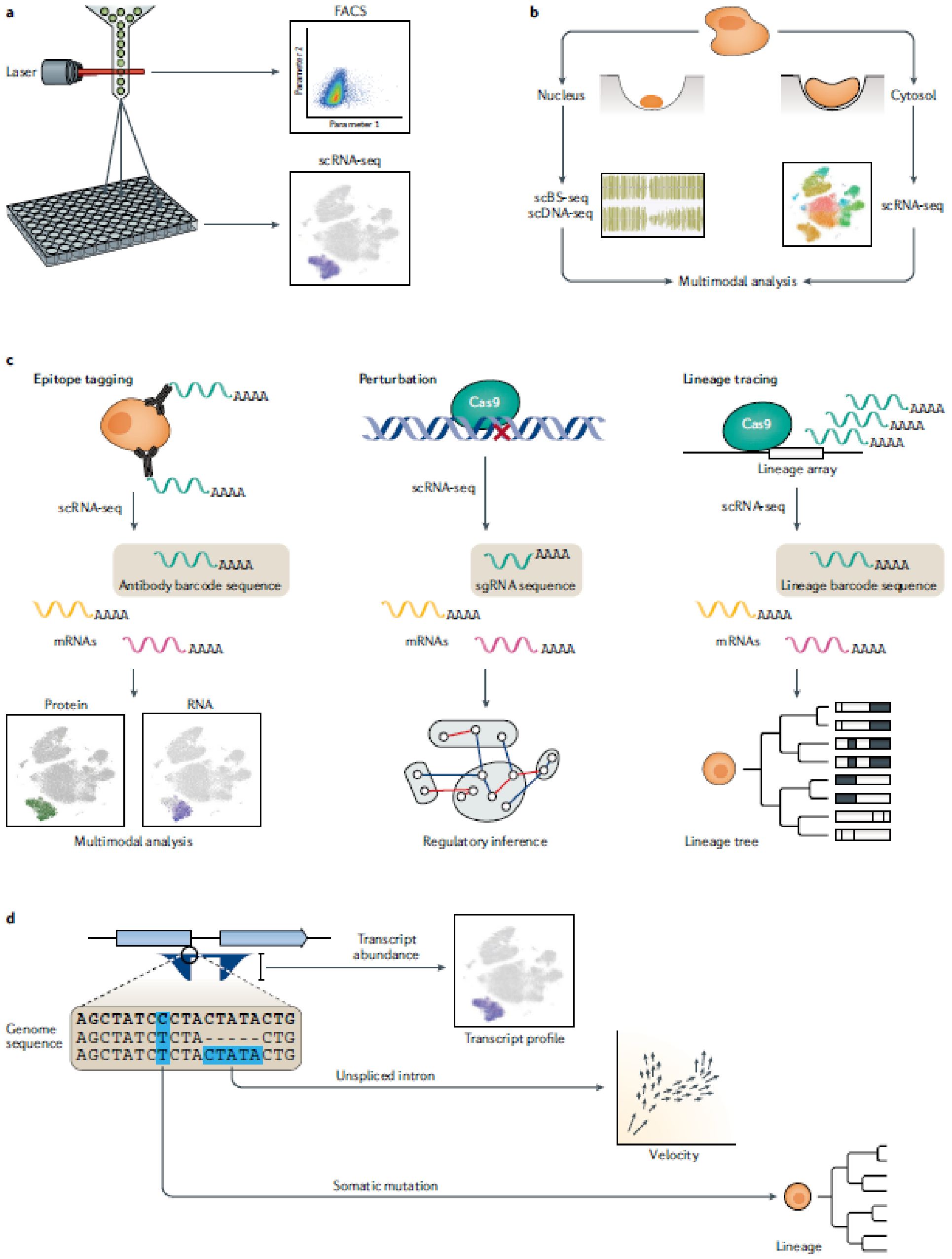
a
Laser
FACS
Parameter 2
Parameter 1
scRNA-seq
b
Nucleus
Cytosol
scBS-seq
scDNA-seq
scRNA-seq
Multimodal analysis
c
Epitope tagging
AAAA
AAAA
scRNA-seq
AAAA
Antibody barcode sequence
AAAA
mRNAs
AAAA
Protein
RNA
Multimodal analysis
Perturbation
Cas9
scRNA-seq
AAAA
sgRNA sequence
AAAA
mRNAs
AAAA
Regulatory inference
Lineage tracing
Cas9
AAAA
AAAA
AAAA
Lineage array
scRNA-seq
AAAA
Lineage barcode sequence
AAAA
mRNAs
AAAA
Lineage tree
d
Transcript abundance
Transcript profile
Genome sequence
AGCTATCCCTACTATACTG
AGCTATCTCTA-----CTG
AGCTATCTCTACTATACTG
Unspliced intron
Velocity
Somatic mutation
Lineage

Computational Analysis for Multiomics

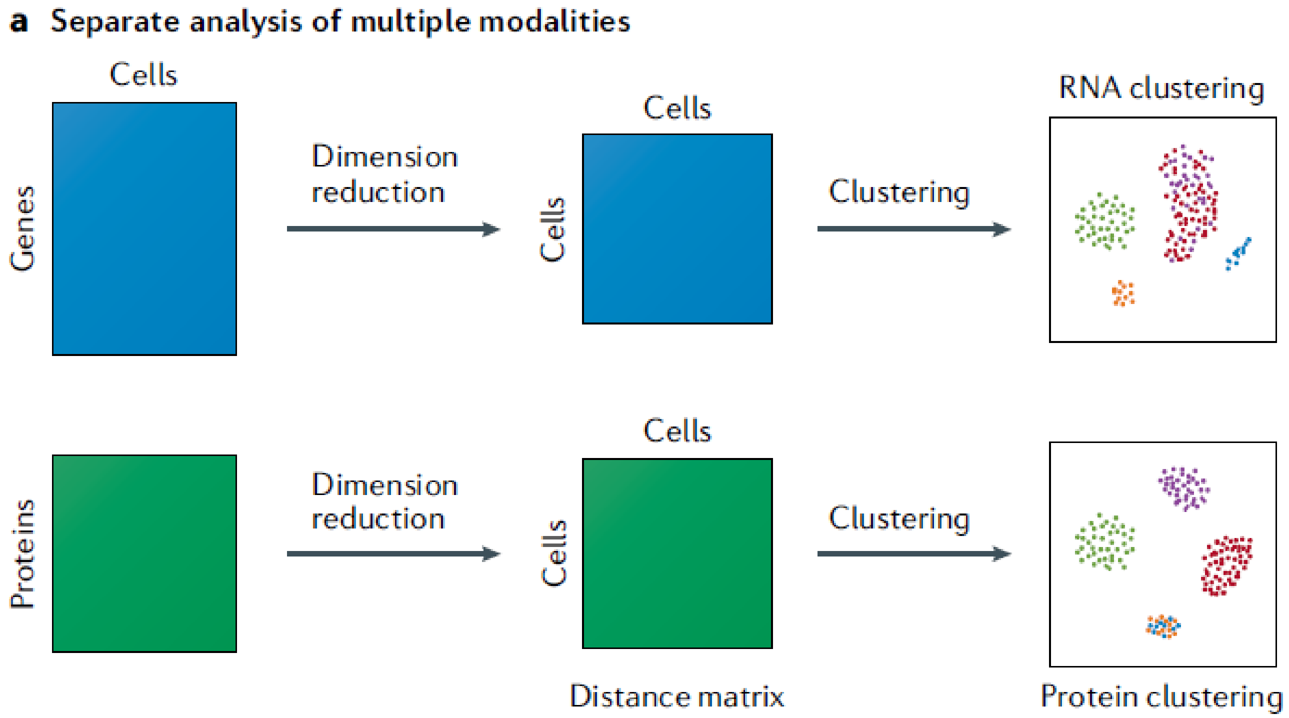

Computational Analysis for Multiomics

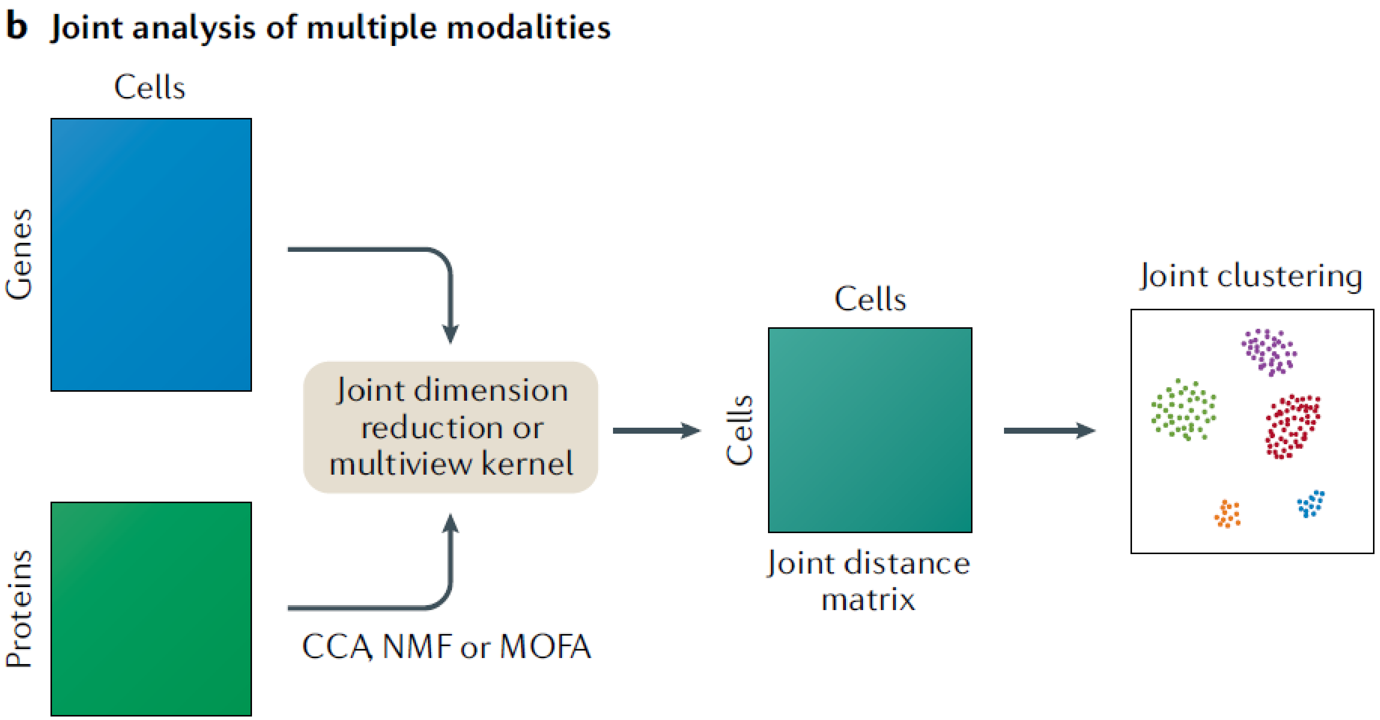

c Multimodal modelling framework

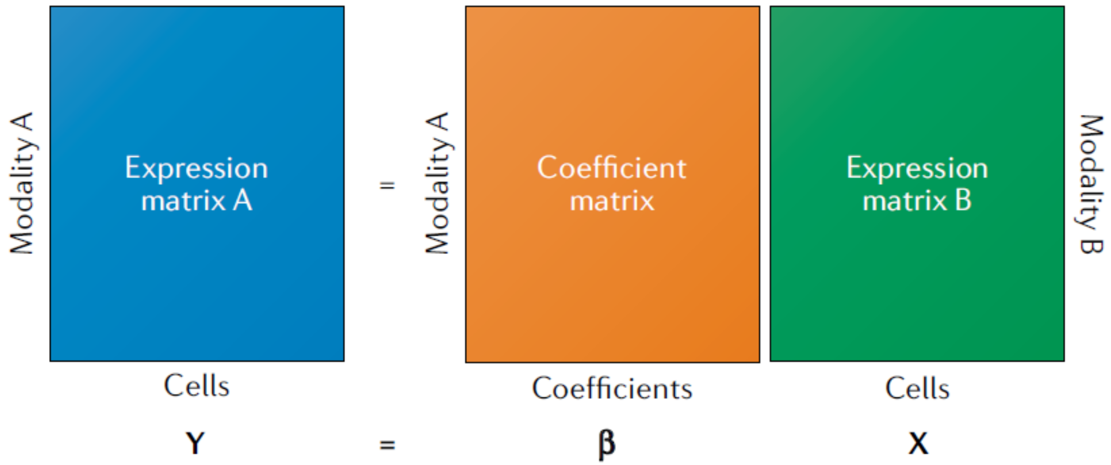

Fig. 3 | **Computational methods for the analysis of multimodal single-cell data.** **a** | Independent analysis of multiple modalities measured from the same group of cells can lead to conflicting identification of clusters of cells. Measurements from one modality may indicate that certain cells are highly similar, while the same cells appear very different when looking at a different modality. In this example, the orange and blue cells form separate clusters when analysed on the basis of their transcriptional profile but cluster together when analysed according to protein measurements. Similarly, the red and purple cells group together based on RNA but separate based on protein. **b** | Joint analysis of multiple modalities measured from the same group of cells can have greater power to identify unique cell states. By taking into account information from multiple modalities, cells can be jointly clustered in a way that outperforms the classifications derived from any one modality alone. In this example, both the red and purple cells and the orange and blue cells form separate groups when protein and RNA information is analysed jointly. **c** | The relationships between data modalities can be studied by building statistical models that aim to explain variance in one modality using a linear combination of components of another modality. CCA, canonical correlation analysis; MOFA, multi-omics factor analysis; NMF, non-negative matrix factorization.

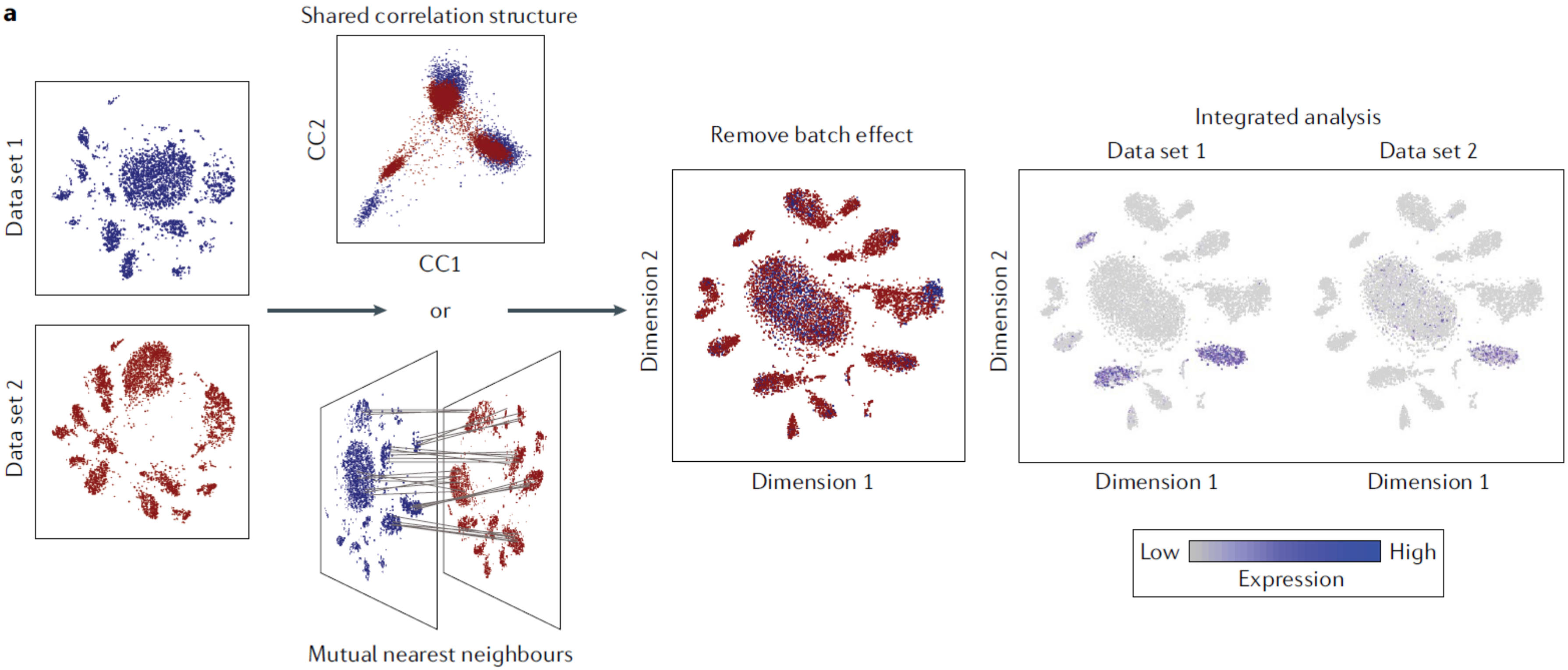
a
Shared correlation structure
CC2
CC1
Data set 1
Data set 2
or
Mutual nearest neighbours
Remove batch effect
Dimension 2
Dimension 1
Integrated analysis
Data set 1
Data set 2
Dimension 2
Dimension 1
Dimension 1
Low
High
Expression

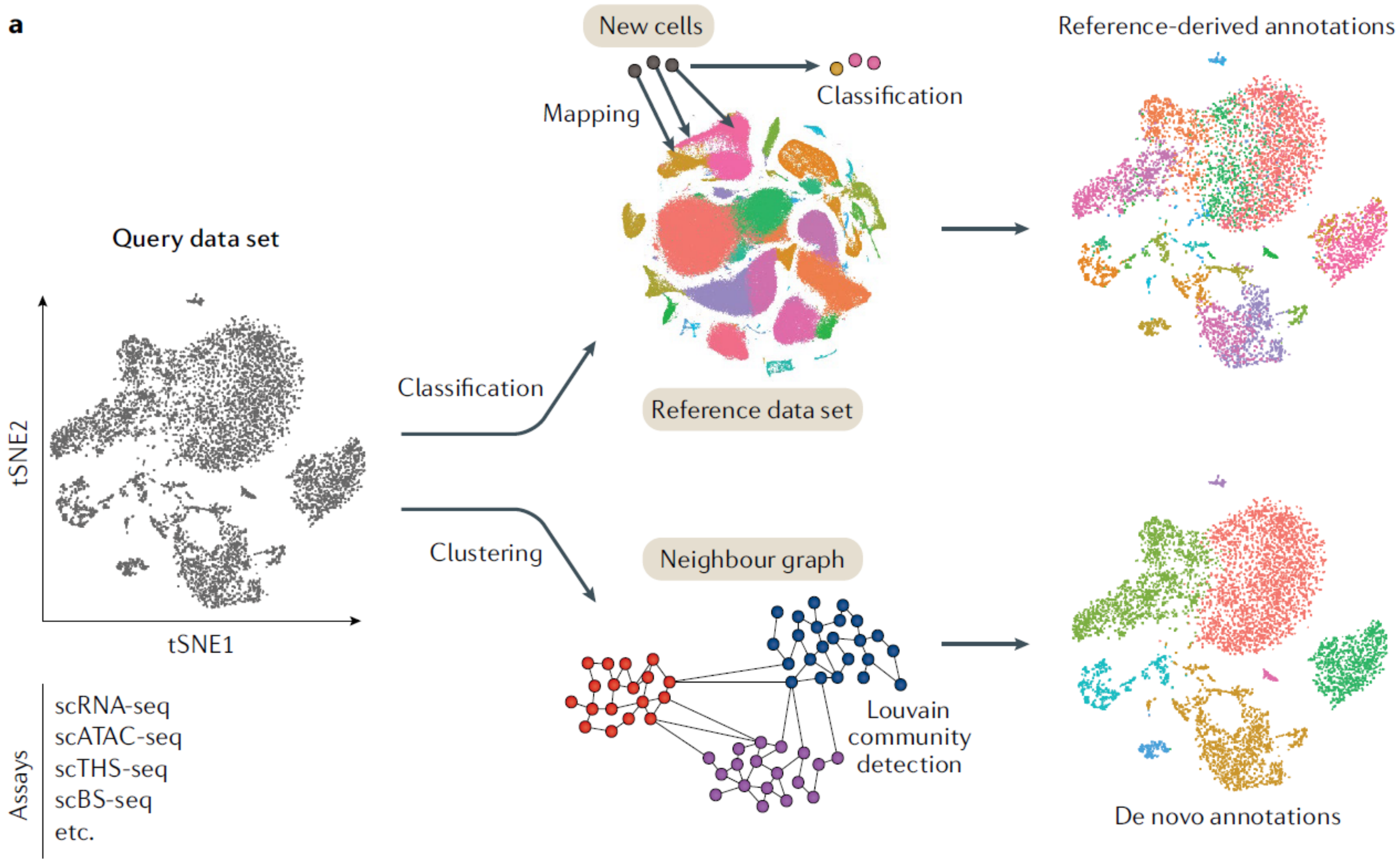
a
New cells
Reference-derived annotations
Mapping
Classification
Query data set
Classification
Reference data set
tSNE2
tSNE1
Clustering
Neighbour graph
Louvain
community
detection
Assays
scRNA-seq
scATAC-seq
scTHS-seq
scBS-seq
etc.
De novo annotations

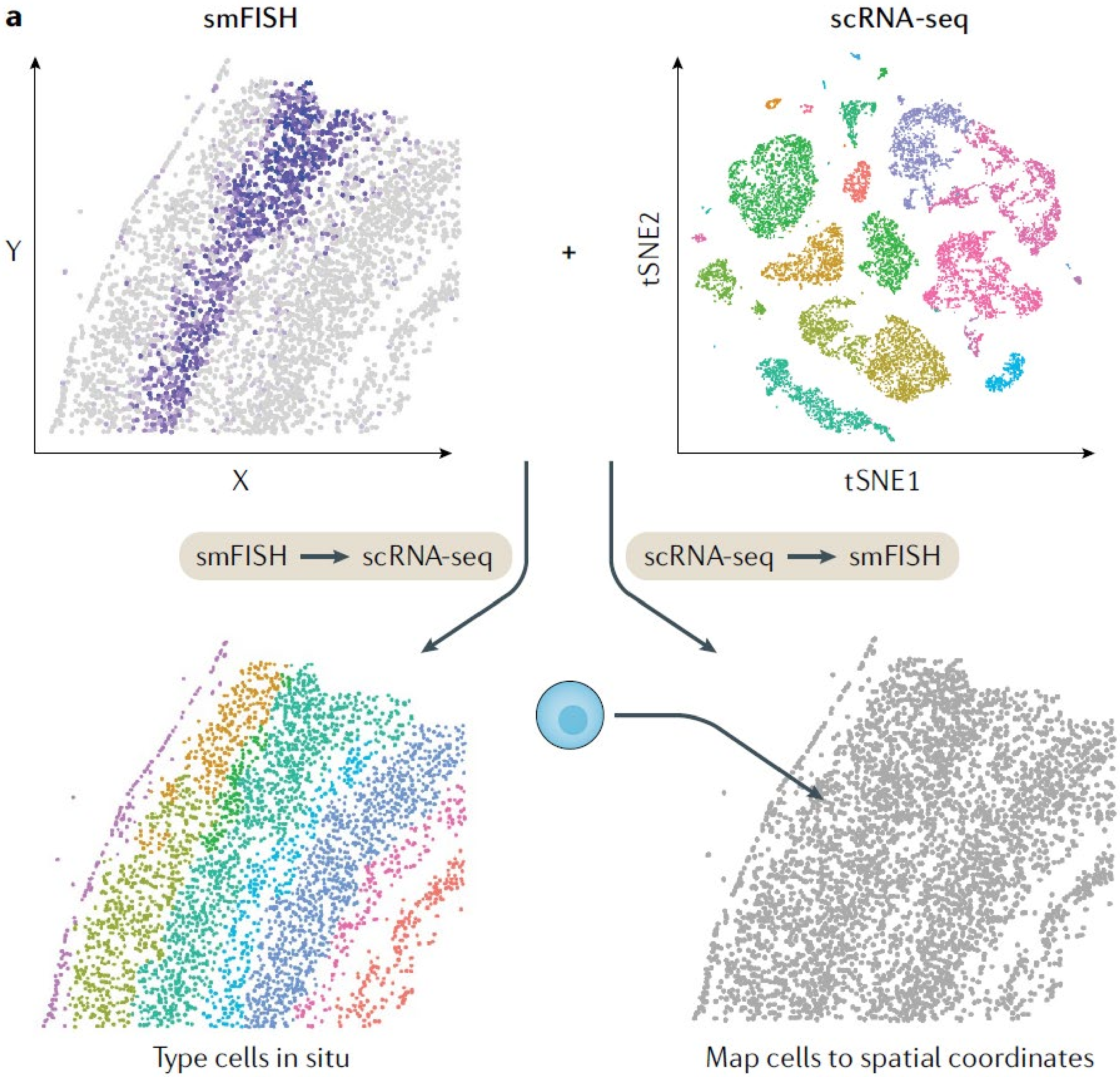
a
smFISH
scRNA-seq
Y
X
+
tSNE2
tSNE1
smFISH → scRNA-seq
scRNA-seq → smFISH
Type cells in situ
Map cells to spatial coordinates

Method of the Year 2020: spatially resolved transcriptomics

Spatially resolved transcriptomics methods are changing the way we understand complex tissues.

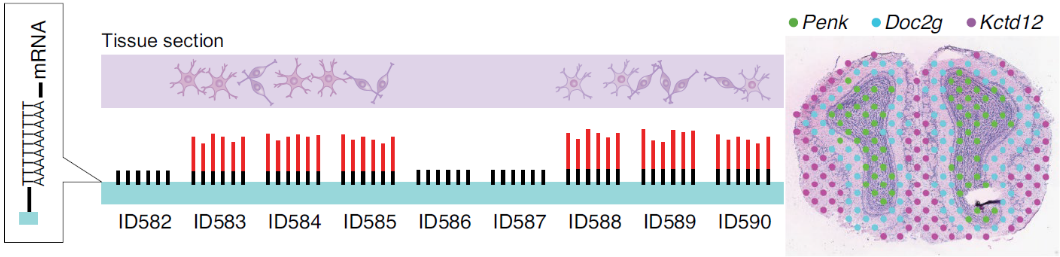

Researchers in Sweden developed an approach in which fixed, stained tissue is imaged, permeabilized and the mRNAs attach to an array of barcoded oligos. The RNAs are reverse-transcribed; the cDNAs are sequenced and yield spatially resolved transcriptomic information. Credit: Adapted with permission from ref. [4], AAAS

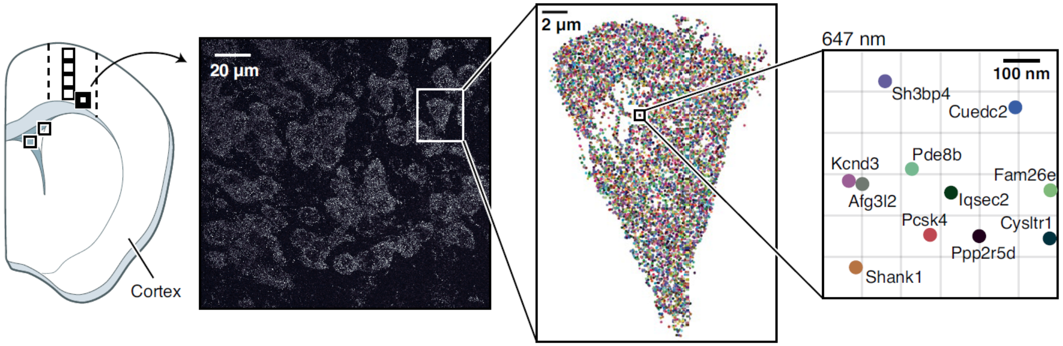

Spatial techniques help with atlas-building by localizing expressed genes. Here, seqFISH+ was used to measure 10,000 genes in mouse cortex. Credit: Cai lab, Caltech, I. Strazhnik; adapted with permission from ref. [6], Springer Nature.

Integrating single-cell and spatial transcriptomics to elucidate intercellular tissue dynamics

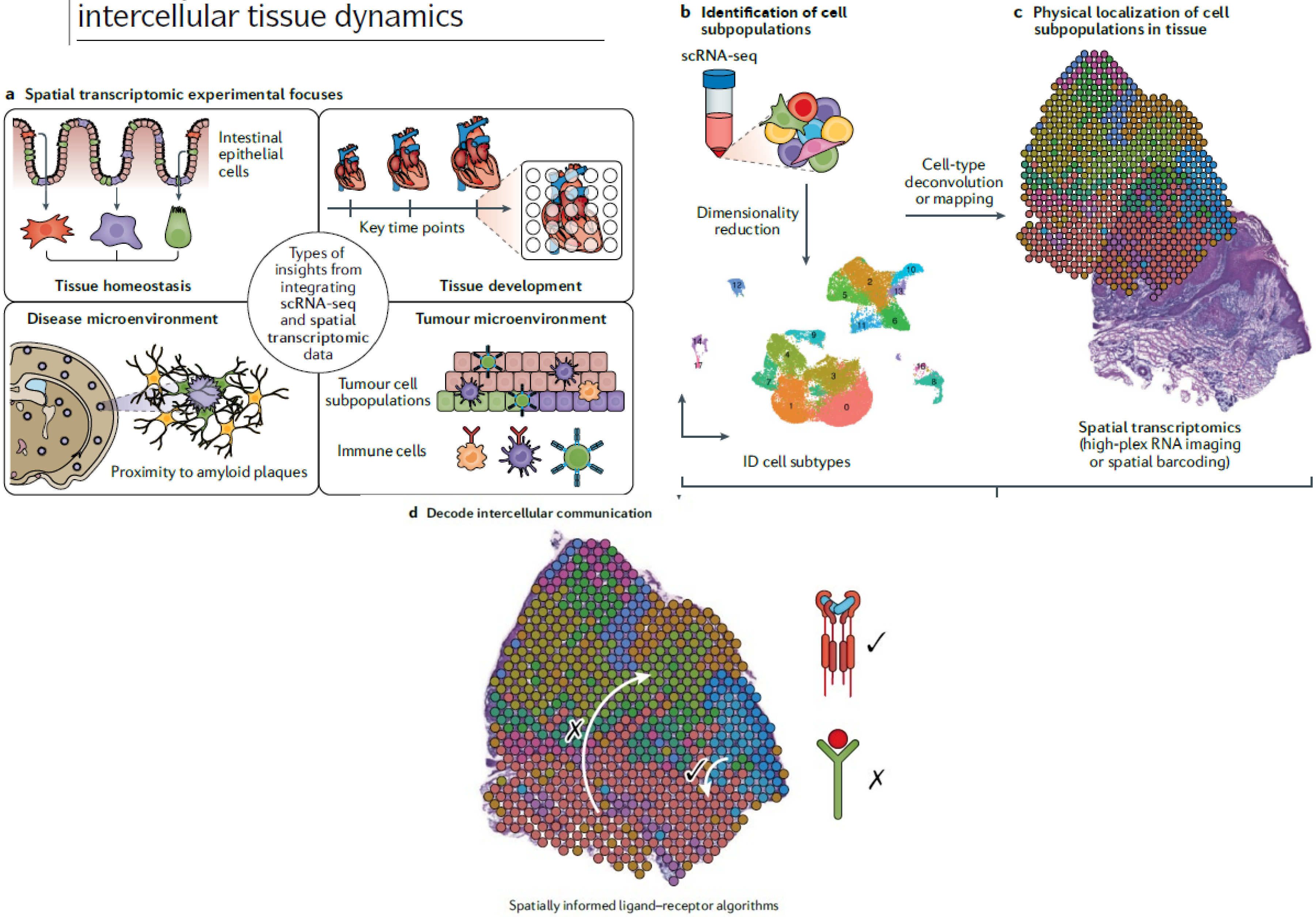

Table 1 | **Widely used spatial transcriptomics techniques and instruments**

Type	Technique	Characteristics	Mechanism notes
High-plex RNA imaging	In situ sequencing for RNA analysis in preserved tissue and cells	25–90 reads per cell[10], 69-gene panel[31]	Genes of interest must be selected to design gene target-specific 'padlock probes'
	STARmap	160-gene panel, ~250 reads per cell	Uses 'padlock probe' mechanism and integrates hydrogel-tissue chemistry for 3D spatial resolution
	Multiplexed error-robust FISH (MERFISH)	135-gene panel, ~100 reads per cell[29]	Each gene has an associated binary code (wherein 1 means fluorescence for a certain part of the sequence, and 0 means no fluorescence)
	Sequential FISH (seqFISH, seqFISH+)	249-gene panel, ~30 reads per cell[13]	Each gene has an associated colour sequence code (24 colour probes per gene) with 60 different pseudo-colour options
Spatial barcoding	Spatial transcriptomics	100 µm diameter capture spot resolution	100 µm from original spatial transcriptomics publication[15]
	Visium spatial gene expression	55 µm diameter	55 µm resolution translates to 3–30 cells per capture spot[16] (original technique[15] is widely accessible through this 10× Genomics Visium Platform: spatialtranscriptomics.com)
	High-definition spatial transcriptomics (HDST)	2 µm diameter	Direct improvement in resolution on spatial transcriptomics[15], but not as accessible
	Slide-seq, Slide-seq v2	10 µm diameter	Uses beads instead of capture spots, with the poly-T oligomers projecting radially around the bead; employs slides

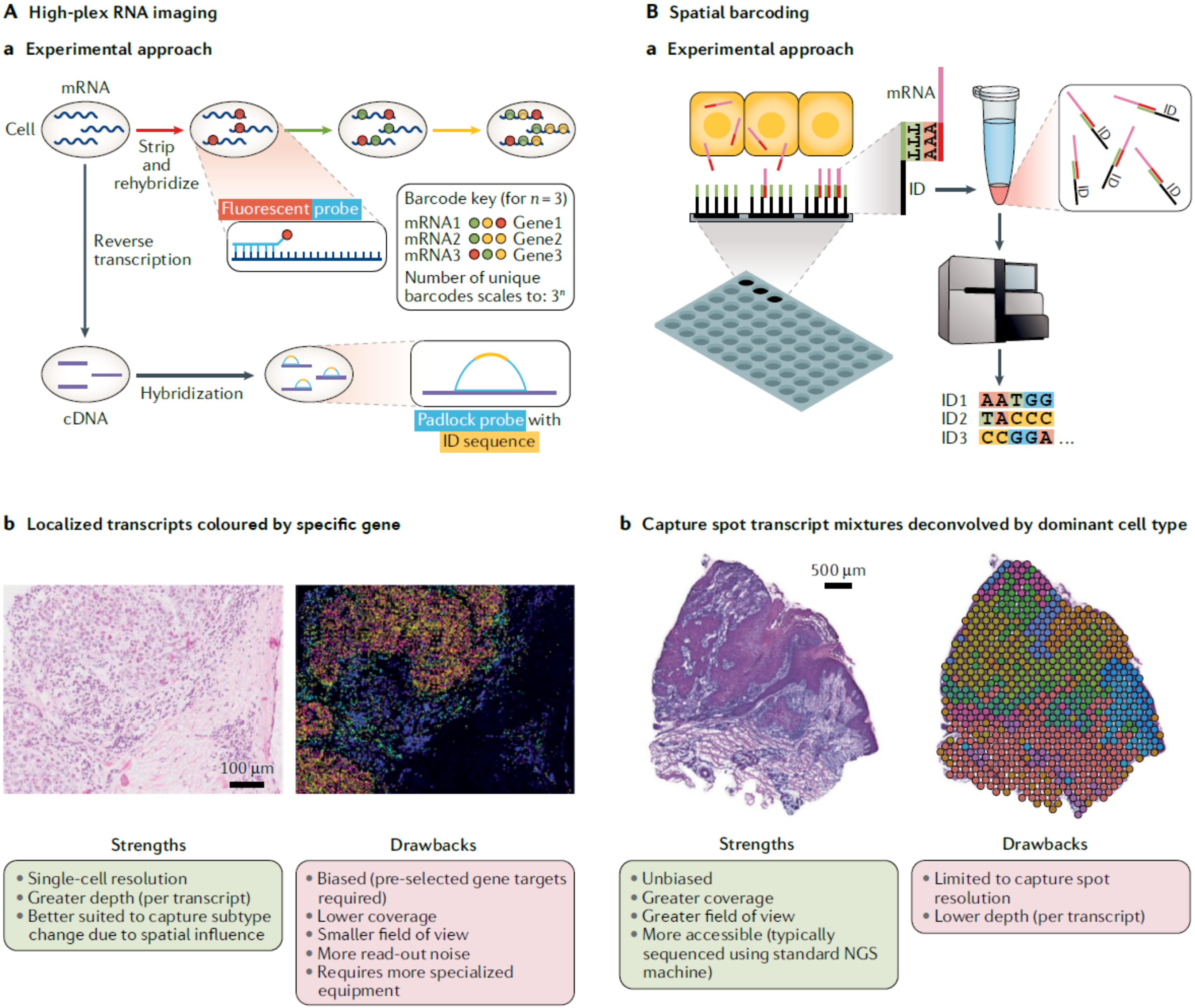

Strengths

- Single-cell resolution
- Greater depth (per transcript)
- Better suited to capture subtype change due to spatial influence

Drawbacks

- Biased (pre-selected gene targets required)
- Lower coverage
- Smaller field of view
- More read-out noise
- Requires more specialized equipment

Strengths

- Unbiased
- Greater coverage
- Greater field of view
- More accessible (typically sequenced using standard NGS machine)

Drawbacks

- Limited to capture spot resolution
- Lower depth (per transcript)

Single-cell atlases: shared and tissue-specific cell types across human organs

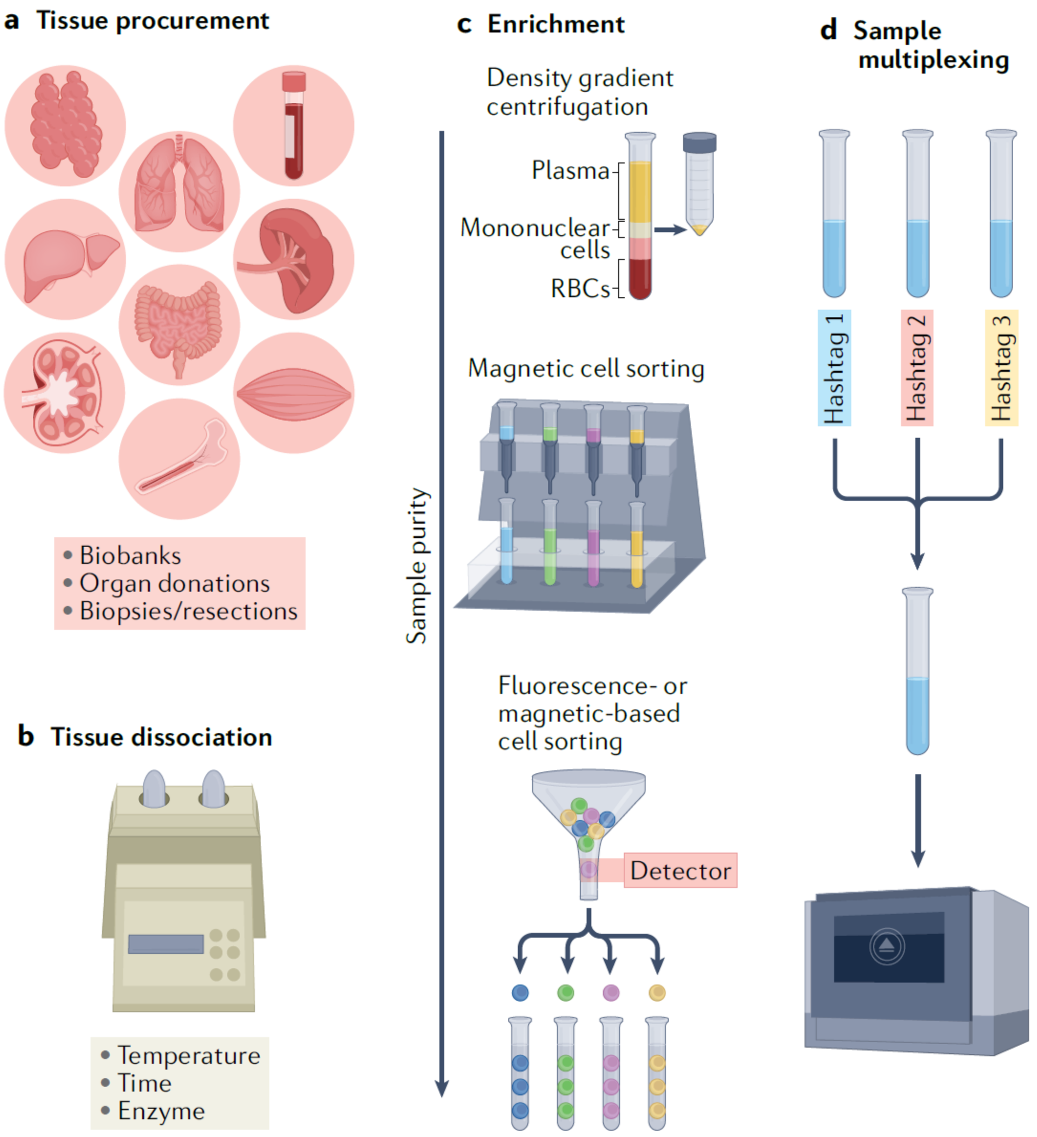

A

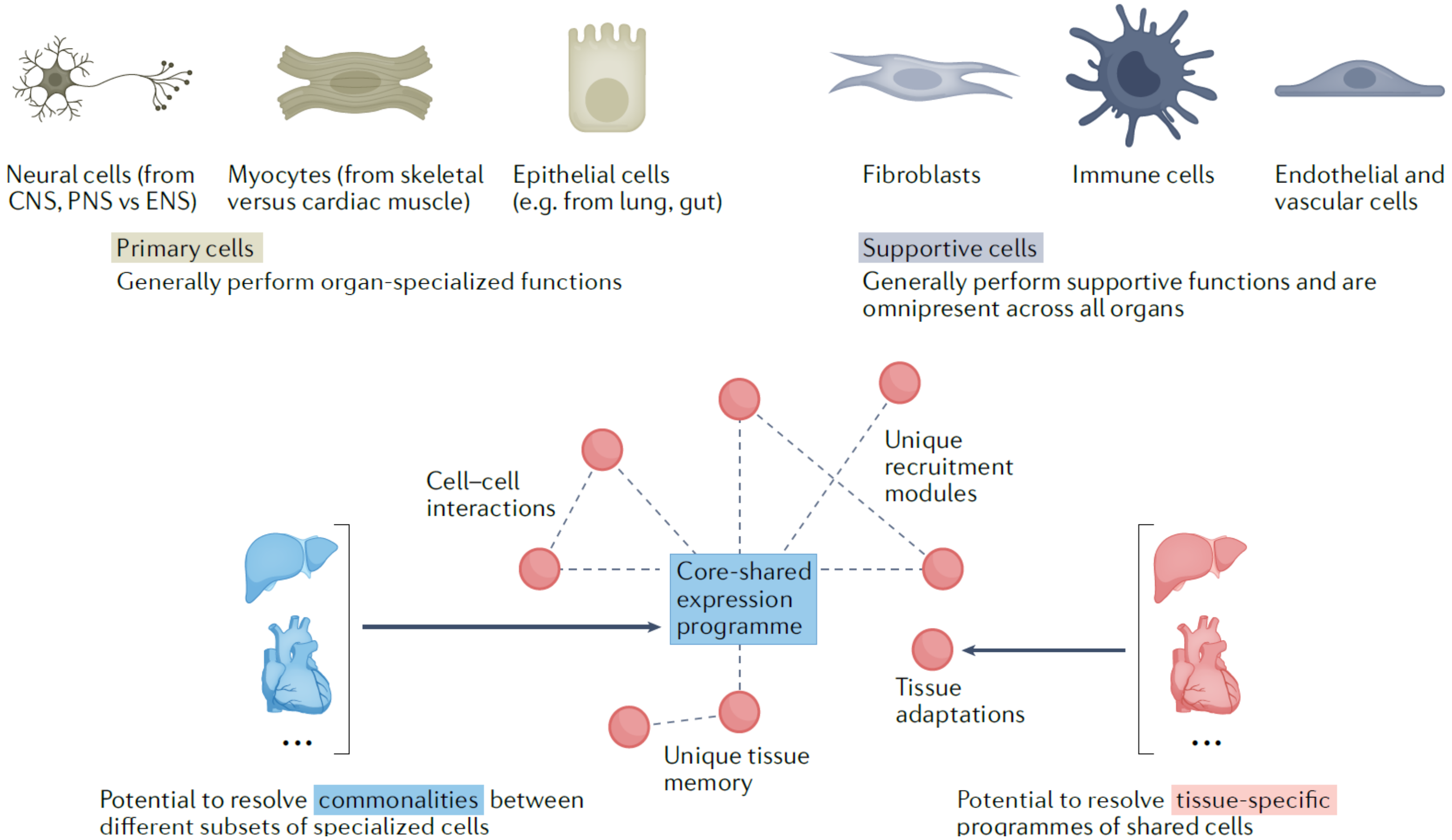

Neural cells (from CNS, PNS vs ENS)

Myocytes (from skeletal versus cardiac muscle)

Epithelial cells (e.g. from lung, gut)

Fibroblasts

Immune cells

Endothelial and vascular cells

Primary cells

Generally perform organ-specialized functions

Supportive cells

Generally perform supportive functions and are omnipresent across all organs

Cell–cell interactions

Unique recruitment modules

Core-shared expression programme

Tissue adaptations

Unique tissue memory

Potential to resolve commonalities between different subsets of specialized cells

Potential to resolve tissue-specific programmes of shared cells

Ba **Tissue-specific disease mechanisms**

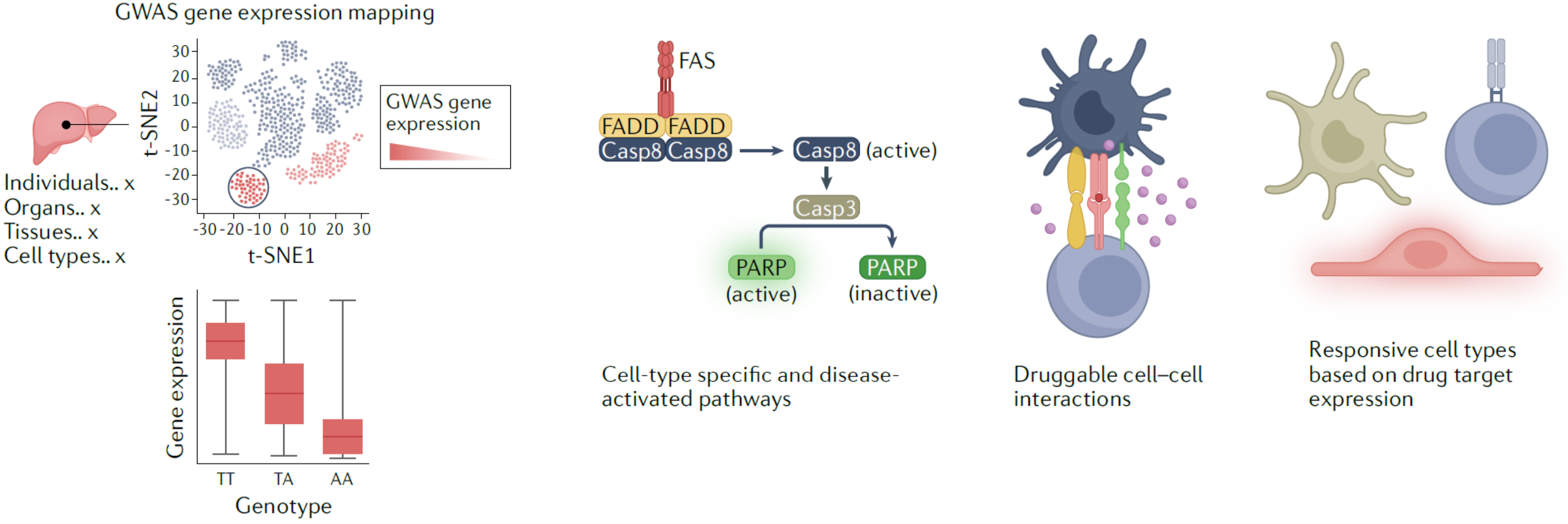

Cell-type specific and disease-activated pathways

Druggable cell–cell interactions

Responsive cell types based on drug target expression

Bb **Therapeutic avenues**

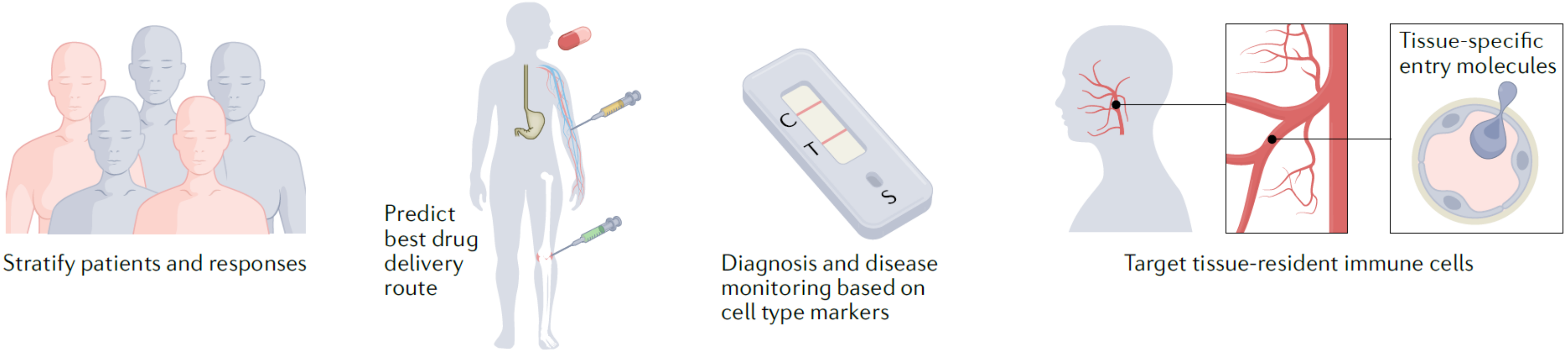

Stratify patients and responses

Predict best drug delivery route

Diagnosis and disease monitoring based on cell type markers

Target tissue-resident immune cells

Super-Resolution Microscopy

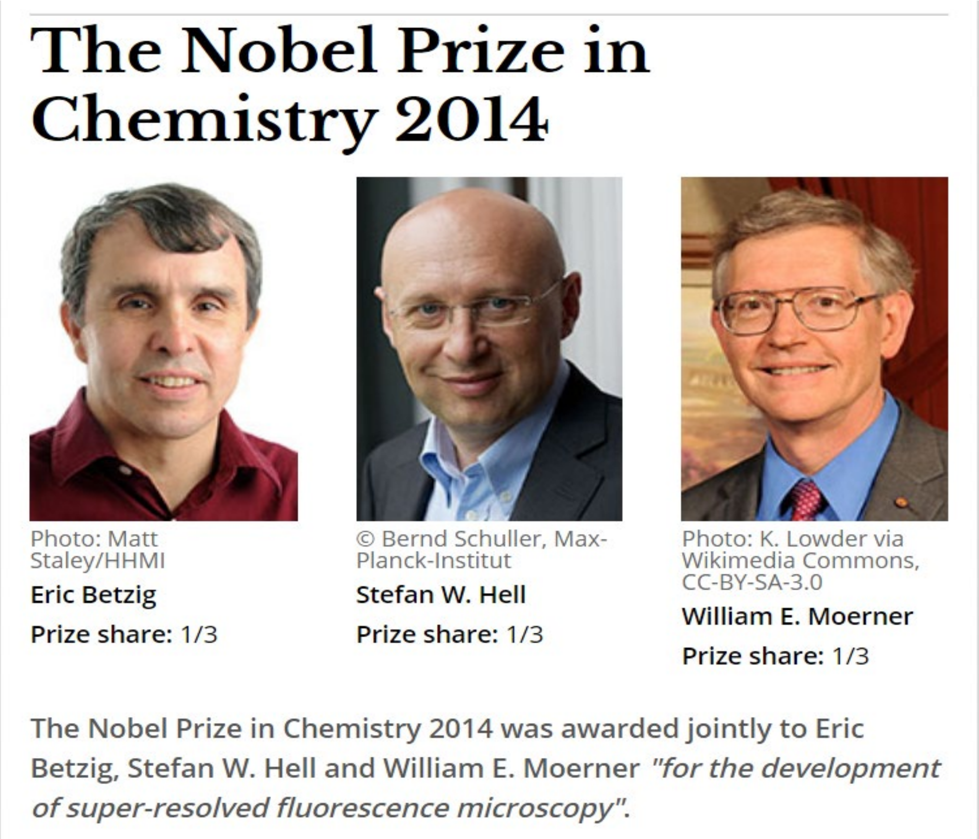

The Nobel Prize in Chemistry 2014

Photo: Matt Staley/HHMI

Eric Betzig

Prize share: 1/3

© Bernd Schuller, Max-Planck-Institut

Stefan W. Hell

Prize share: 1/3

Photo: K. Lowder via Wikimedia Commons, CC-BY-SA-3.0

William E. Moerner

Prize share: 1/3

The Nobel Prize in Chemistry 2014 was awarded jointly to Eric Betzig, Stefan W. Hell and William E. Moerner *"for the development of super-resolved fluorescence microscopy"*.

Two separate principles are rewarded. One enables the method *stimulated emission depletion (STED) microscopy,* developed by Stefan Hell in 2000.

Eric Betzig and William Moerner, working separately, laid the foundation for the second method, *single-molecule microscopy*.

Microscope

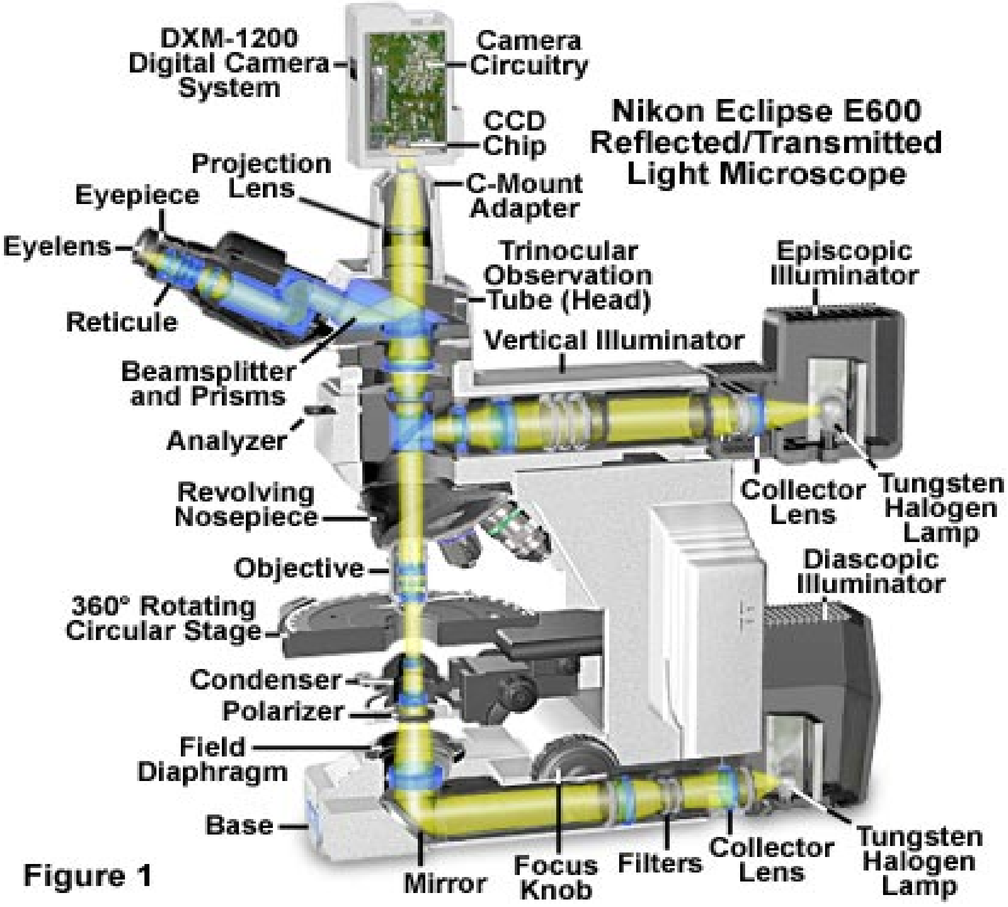

Figure 1

Resolution

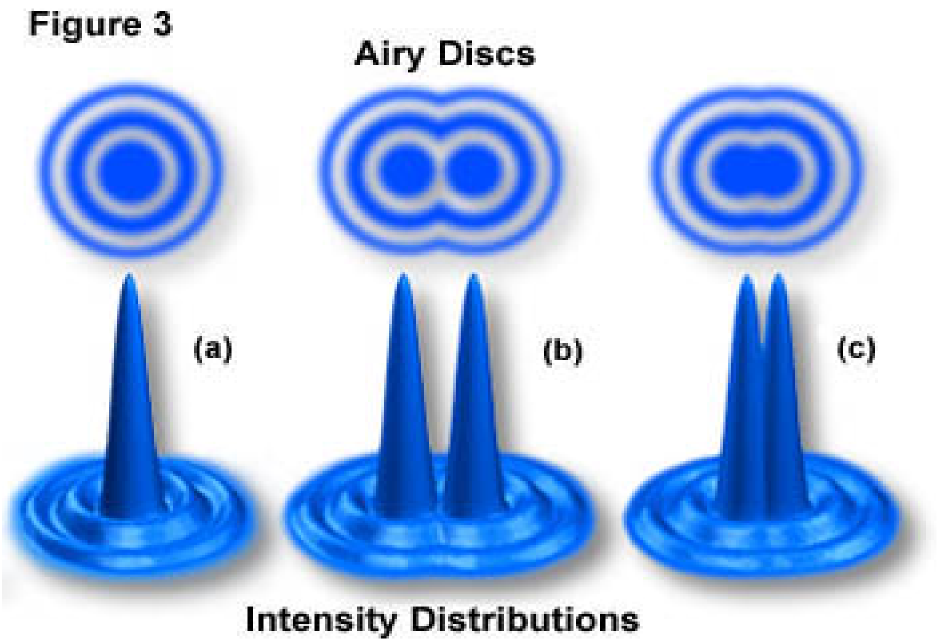

Resolution (r) = $\lambda/(2NA)$ (1)

Resolution (r) = $0.61\lambda/NA$ (2)

Resolution (r) = $1.22\lambda/(NA(obj) + NA(cond))$ (3)

Airy Patterns and the Limit of Resolution

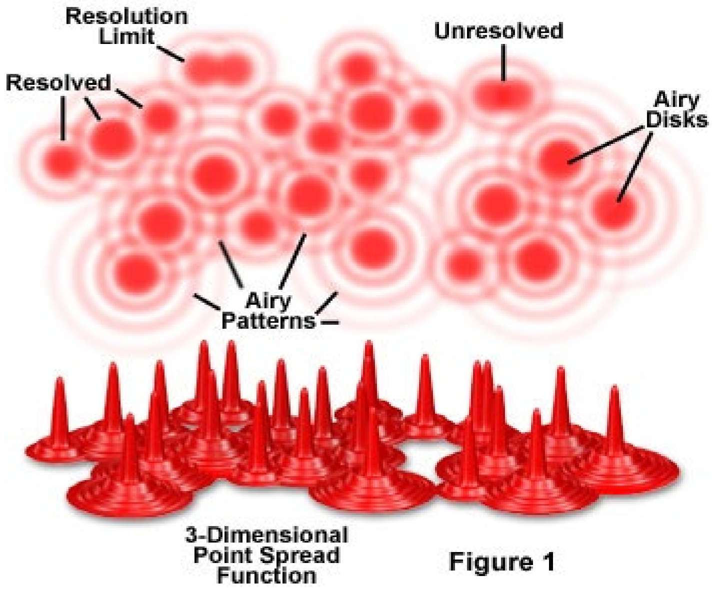

Figure 1

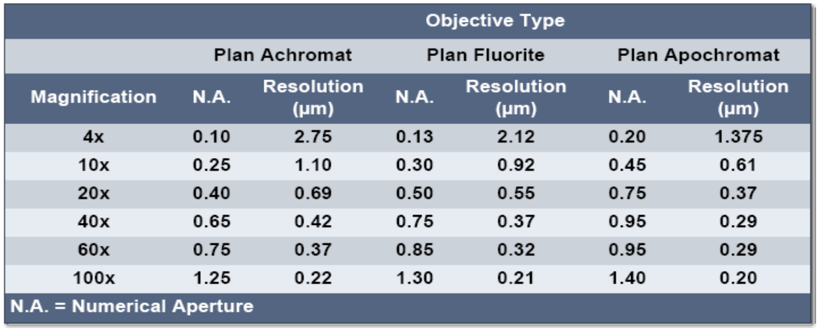

	Objective Type					
	Plan Achromat		Plan Fluorite		Plan Apochromat	
Magnification	N.A.	Resolution (µm)	N.A.	Resolution (µm)	N.A.	Resolution (µm)
4x	0.10	2.75	0.13	2.12	0.20	1.375
10x	0.25	1.10	0.30	0.92	0.45	0.61
20x	0.40	0.69	0.50	0.55	0.75	0.37
40x	0.65	0.42	0.75	0.37	0.95	0.29
60x	0.75	0.37	0.85	0.32	0.95	0.29
100x	1.25	0.22	1.30	0.21	1.40	0.20

N.A. = Numerical Aperture

Resolution versus Wavelength

Wavelength (Nanometers)	Resolution (Micrometers)
360	.19
400	.21
450	.24
500	.26
550	.29
600	.32
650	.34
700	.37

N.A. = 0.95

Diffraction Limit

$$d = \lambda/(2n \sin \alpha)$$

$$, k_0 = 2NA/\lambda_{\mathrm{em}}$$

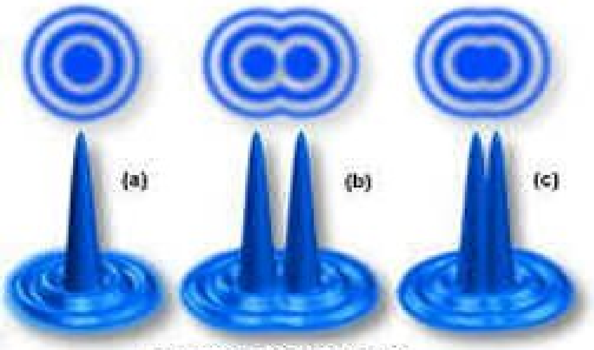

Intensity Distributions

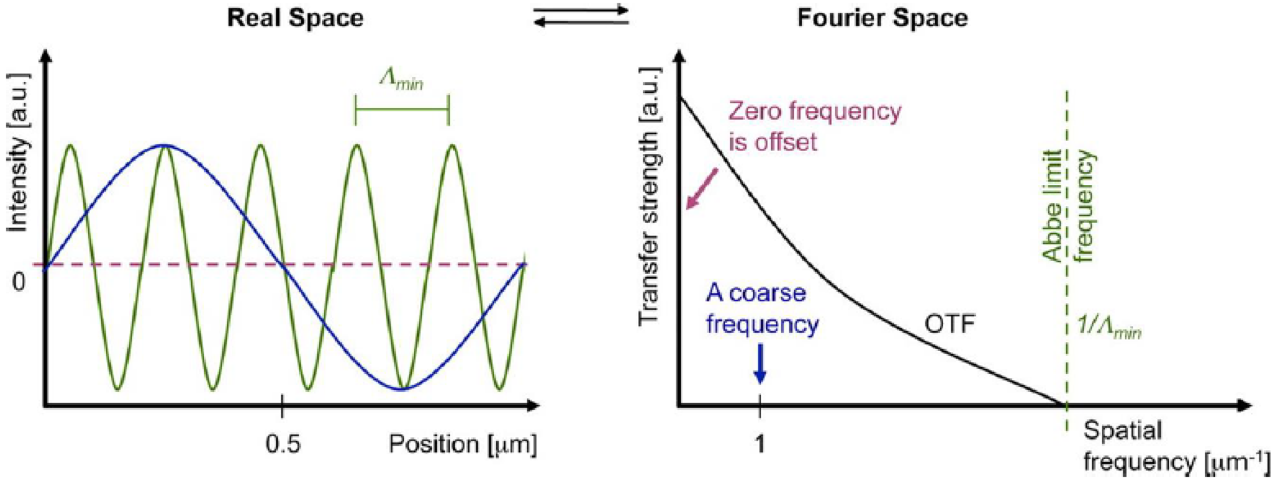

For a homogeneous medium, the solution to the homogeneous equation is of the form

$$H_\omega(k_r, z) = A^+(k_r)\,\mathrm{e}^{\mathrm{i}k_z z} + A^-(k_r)\,\mathrm{e}^{-\mathrm{i}k_z z} \tag{2.98}$$

with k_z being the vertical wavenumber,

$$k_z = \sqrt{k^2 - k_r^2}. \tag{2.99}$$

Since the inverse Hankel transform must be evaluated over a semi-infinite wavenumber domain, we have to choose a definition for the square root for $k_r > k$. We choose the definition

$$k_z = \begin{cases} \sqrt{k^2 - k_r^2}, & k_r \le k \\ \mathrm{i}\sqrt{k_r^2 - k^2}, & k_r > k\,. \end{cases} \tag{2.100}$$

Breaking the Diffraction Barrier: Super-Resolution Imaging of Cells

Bo Huang,[1] Hazen Babcock,[2] and Xiaowei Zhuang[2,3,*]

Cell *143*, December 23, 2010 ©2010 Elsevier Inc. **1047**

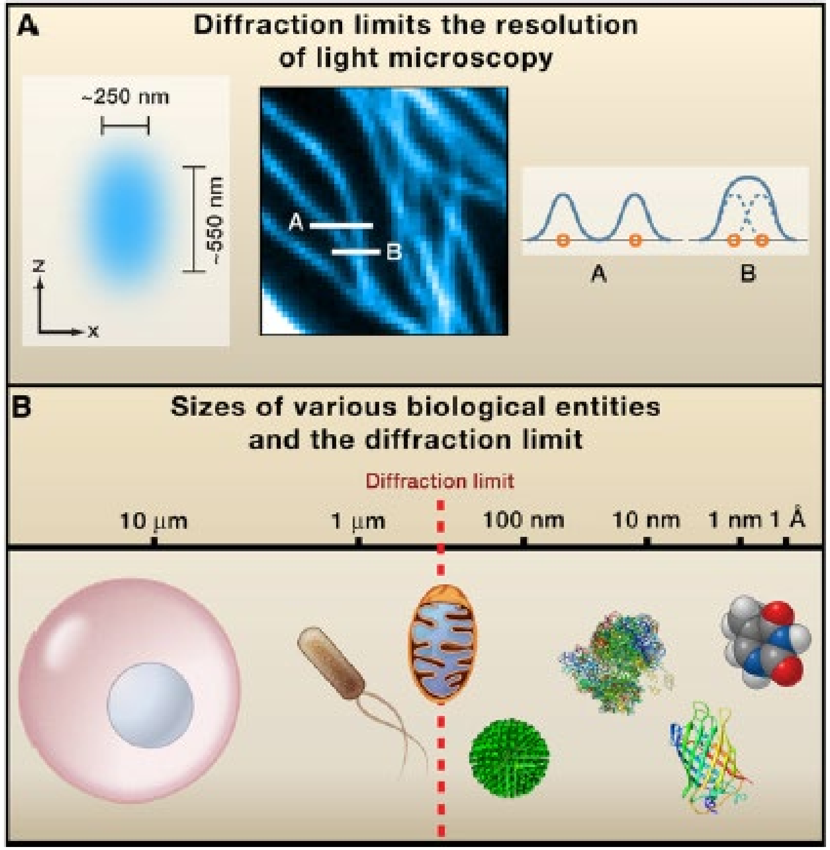

Figure 1. Diffraction-Limited Resolution of Conventional Light Microscopy

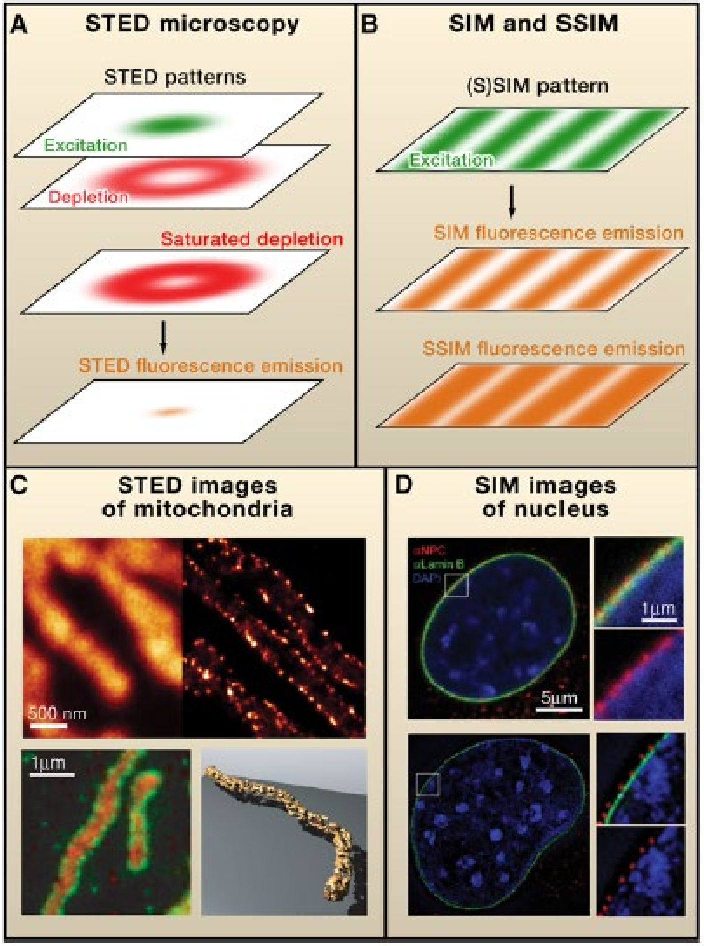

Figure 2. Super-Resolution Fluorescence Microscopy by Patterned Illumination

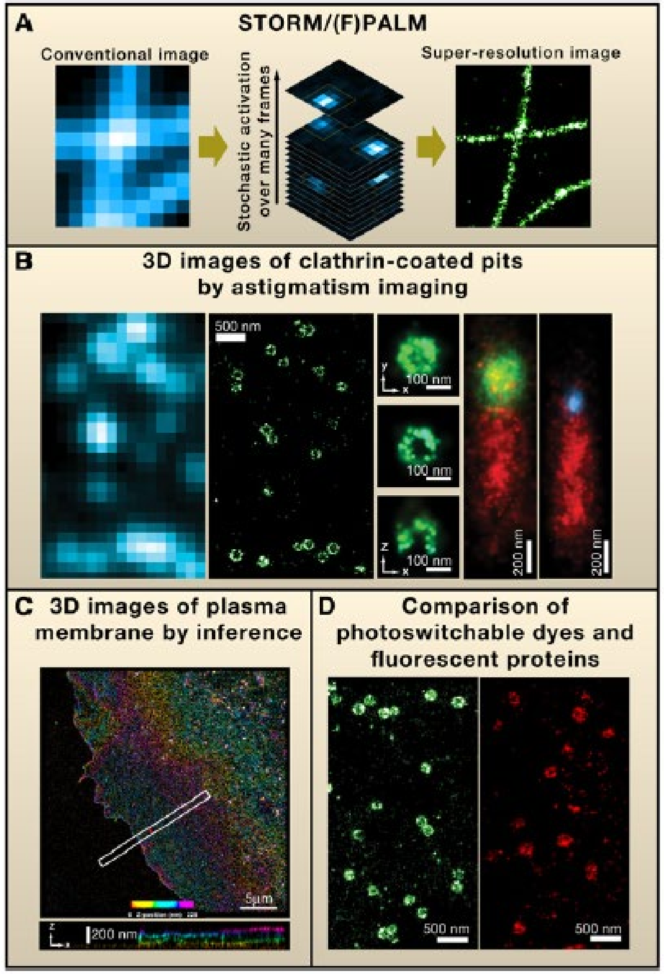

Figure 3. Super-Resolution Fluorescence Microscopy by Single-Molecule Switching

Super-Resolution Microscopy

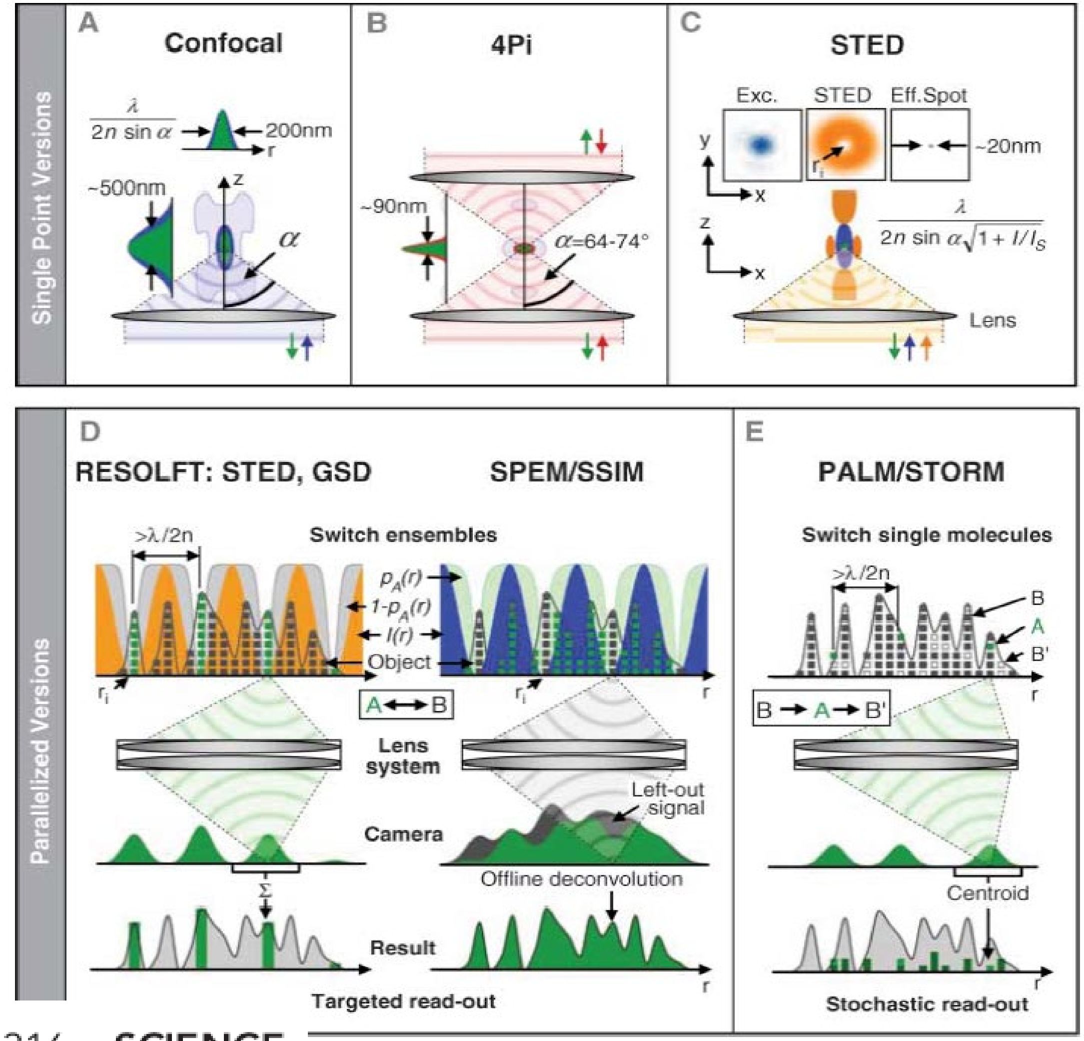

25 MAY 2007 VOL 316 **SCIENCE**

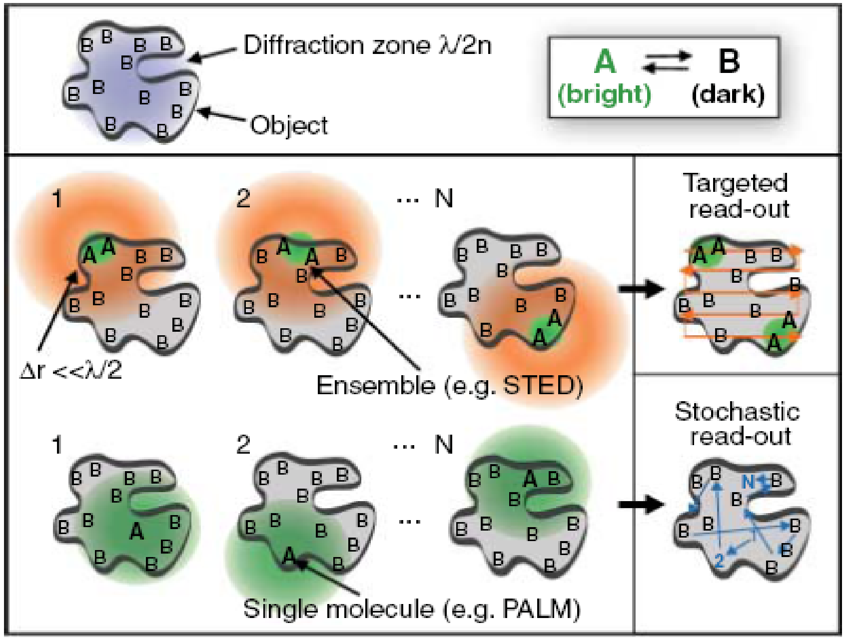

Fig. 2. Targeted versus stochastic time-sequential readout of fluorophore markers of a nanostructured object within the diffraction zone whose lower bound is given by $\lambda/2n$. A and B denote a bright and a dark state, respectively. In the targeted readout mode, one of the two states (here A) is established at a subdiffraction-sized spot at the position of a zero to read out an unknown number of fluorophore molecules. The image is assembled by deliberate translation of the zero. The zero can also be a groove. In the stochastic readout mode, a single switchable fluorophore from a random position within the diffraction zone is switched to a stable state A, while the other molecules remain in B. The coordinate is calculated from the centroid of the diffraction fluorescence spot measured by a pixelated detector. The coordinate pops up stochastically depending on where the interrogated marker molecule is located.

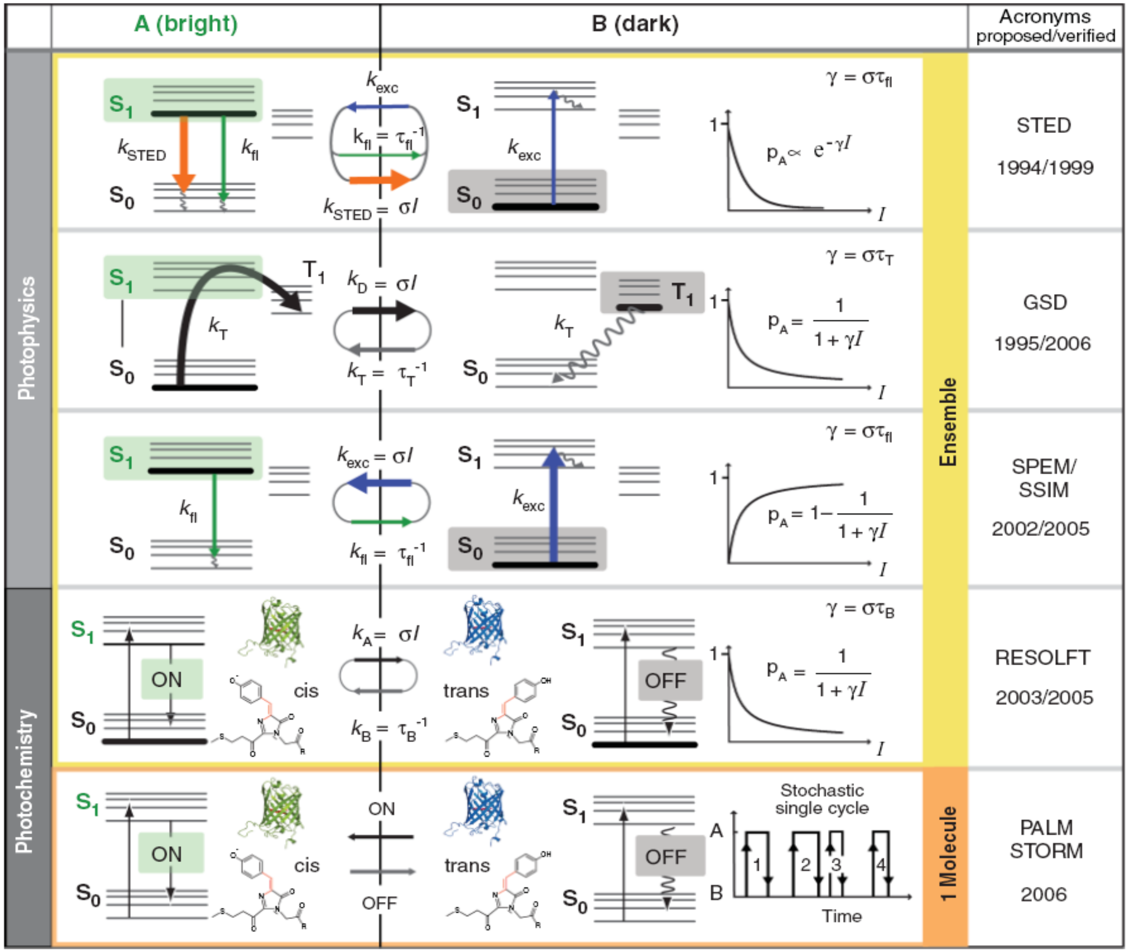

Fig. 3. Bright (**A**) and dark (**B**) molecular states used to break the diffraction barrier. Whereas STED, GSD, and SPEM utilize photophysical transitions, the photoswitching version of the RESOLFT scheme, as well as PALM and STORM, exploit photochemical transitions in which atoms are relocated or bonds formed and broken. PALM and STORM rely on measuring single (or at least identifiable) molecules at a time, whereas the other concepts, although compatible with single-molecule imaging, principally read out ensembles. Ensemble techniques rely on reversible transitions between A and B, as indicated by the rates k. The probability p_A of being in state A depends nonlinearly on the light intensity applied, as indicated by the equations, ensuring that either A or B is confined to a subdiffraction area at a targeted coordinate in space. The $e^{-\gamma I}$ and the $(1 + \gamma I)^{-1}$ dependence entail nonlinearities of infinite order $(\gamma I)^m$; $m \to \infty$. By increasing the lifetime of the chosen states, γ strengthens the nonlinear dependence of p_A, thus enabling huge nonlinearities at low I. This is radically different from m-photon processes that, depending on the concomitant action of m photons and hence just on I^m, are firmly limited to order m (*15*), which in practice is only $m < 4$. Because it operates with single molecules in a known state, the probability concept breaks down in PALM and STORM, but reminiscent of nonlinearity is the optical switching.

REversible **S**aturable **O**ptica**L** **F**luorescence **T**ransitions (RESOLFT)

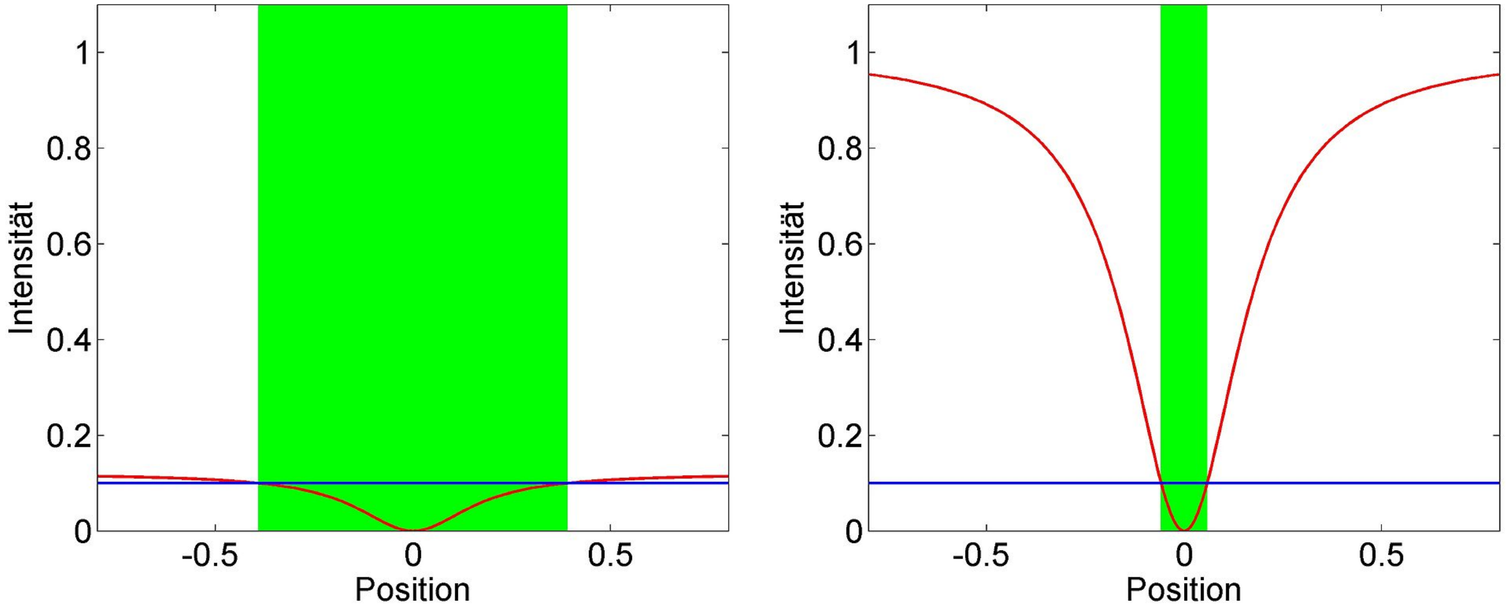

Principle of resolution increase in a RESOLFT microscope. Horizontally a spatial dimensions is drawn. The red line corresponds to the spatially variable intensity of the light beam which drives molecules from a certain state (green) to another state (white). The blue line describes the level of saturation for this transition. Increasing the brightness (right side) of the light beam one can restrict the area, where molecules can reside in their original state (green) to arbitrarily small volumes

Appl. Phys. B 60, 495–497 (1995)

Applied
Physics B Lasers and Optics

Rapid communication

Ground-state-depletion fluorscence microscopy: a concept for breaking the diffraction resolution limit

S.W. Hell, M. Kroug

Department of Medical Physics, University of Turku, and Centre for Biotechnology, P.O. Box 123, FIN-20521 Turku, Finland
(Fax: +358-21/633-8000, E-mail: STEFAN.HELL@utu.fi)

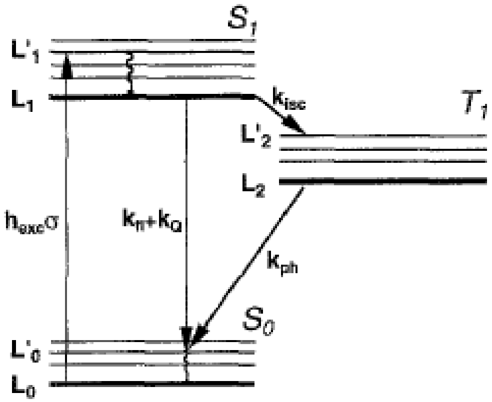

Fig. 1. Energy states of a typical dye: S_0 is the ground state, S_1 is the first singlet state, and T_1 the first triplet state

$$
\begin{aligned}
\frac{dn_0}{dt} &= -h_{\mathrm{exc}}\sigma n_0 + \left(k_{\mathrm{fl}} + k_{\mathrm{Q}}\right) n_1 + k_{\mathrm{ph}} n_2 \ , \\
\frac{dn_1}{dt} &= +h_{\mathrm{exc}}\sigma n_0 - \left(k_{\mathrm{fl}} + k_{\mathrm{Q}}\right) n_1 - k_{\mathrm{isc}} n_1 \ , \\
\frac{dn_2}{dt} &= +k_{\mathrm{isc}} n_1 - k_{\mathrm{ph}} n_2 \ ,
\end{aligned}
$$

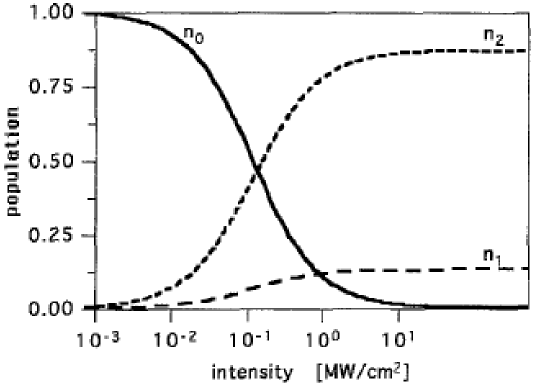

Fig. 2. The population probability of the ground state (n_0), the first singlet state (n_1), and the triplet state (n_2) as a function of the excitation intensity for fluoresceine

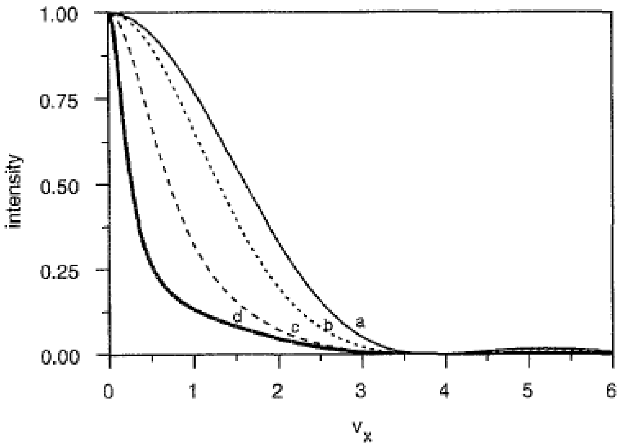

Fig. 4. Calculated effective point-spread function along the axis of the offset for peak intensities of (*b*) 0.01, (*c*) 0.1, and (*d*) 1 MW/cm^2 of the depletion beam as calculated for fluorescein, compared with the point-spread function of a classical scanning fluorescence microscope

tion, as shown in Fig. 5. A comparison of the point-spread-function obtained for a focal intensity of 1 MW/cm^2 with that of a classical scanning fluorescence microscope shows an increase in resolution by a factor of 11. Assuming an excitation wavelength of 400 nm and a numerical aperture of 1.4, one obtains a lateral FWHM of about 15 nm.

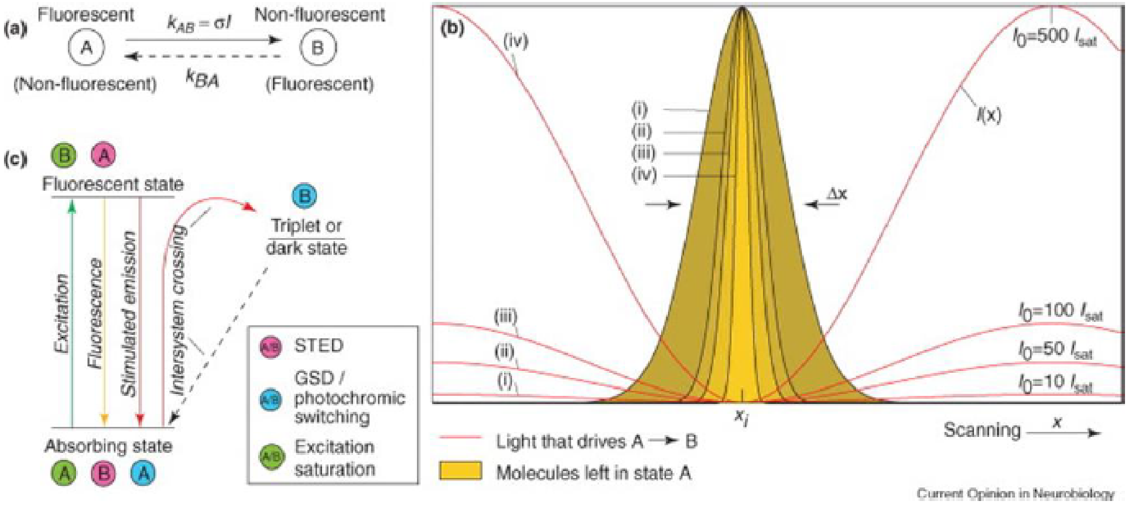

Figure 4: (Hell *et al.*, *Current Opinion in Neurobiology* 2004, 14:599–609). (a) Illustration of the fluorescence depletion principle. (b) Fluorescence density (yellow) as a function of the x-coordinate in the focal plane at STED intensities (I(x), red) with different maximal strengths (I_o). The fluorescence density (yellow) becomes sharper with increasing I_o.

Confocal

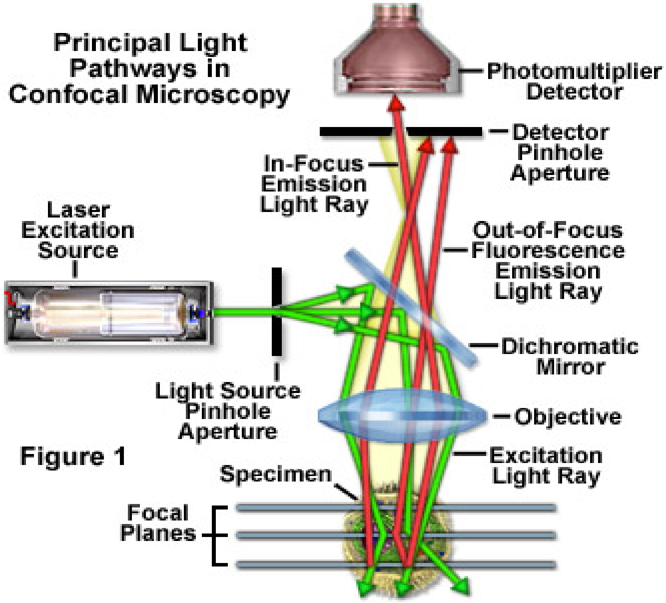
Principal Light Pathways in Confocal Microscopy
Photomultiplier Detector
Detector Pinhole Aperture
In-Focus Emission Light Ray
Laser Excitation Source
Out-of-Focus Fluorescence Emission Light Ray
Dichromatic Mirror
Light Source Pinhole Aperture
Objective
Figure 1
Excitation Light Ray
Specimen
Focal Planes

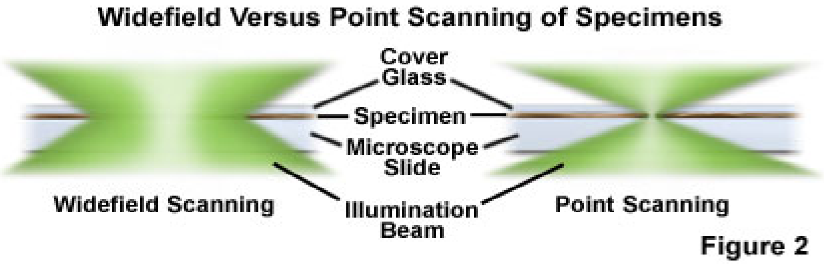
Widefield Versus Point Scanning of Specimens
Cover Glass
Specimen
Microscope Slide
Widefield Scanning
Illumination Beam
Point Scanning
Figure 2

Tracking kinesin-driven movements with nanometre-scale precision

Jeff Gelles*, Bruce J. Schnapp† & Michael P. Sheetz*

NATURE VOL. 331 4 FEBRUARY 1988

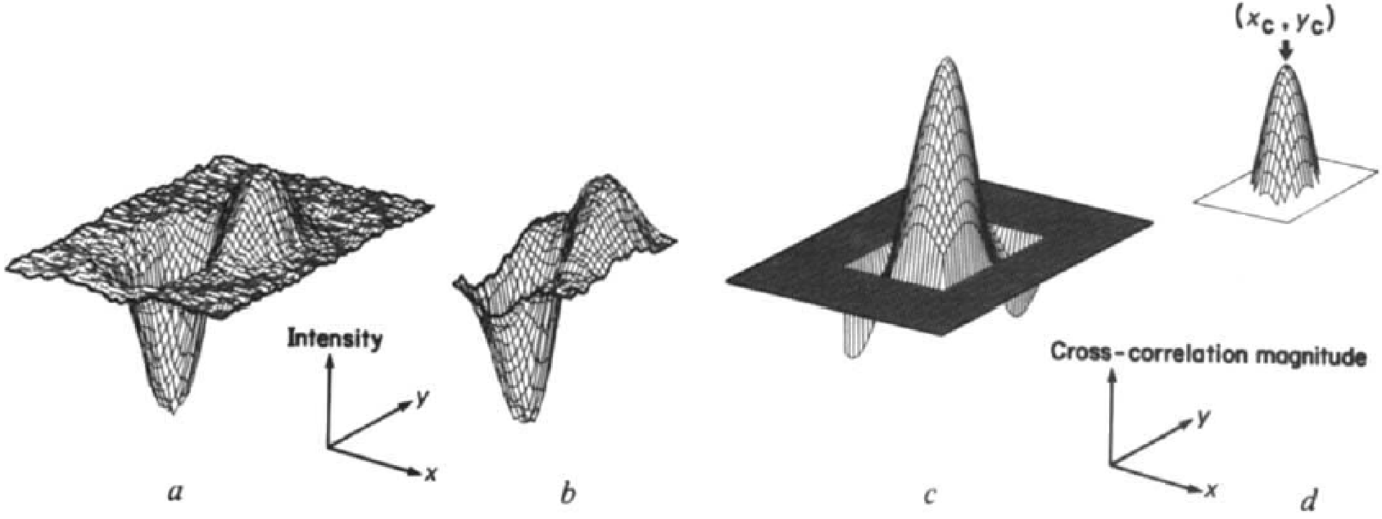

Fig. 1 Stages in the high-precision measurement of relative bead position in a video frame. *a*, Image; *b*, kernel; *c*, cross-correlation of image and kernel; *d*, centroid calculation. The illustrated sequence of computations derives positional information from the entire bead image rather than from an individual point or edge only, and thereby maximizes the precision of the measurement. *a*, A segment of a digitized video frame containing the video-enhanced DIC microscope image of a bead. The DIC image of a single bead consists of apposed bright and dark areas. The segment consists of a 49×63 rectangular matrix of integers, $\mathbf{I}(x, y)$, each of which represents the recorded light intensity at the point (x, y) in the image (x and y are integers). *b*, A 'kernel' segment $\mathbf{K}(x, y)$, consisting entirely of a single bead image. The centre of this segment is taken to be the point (0, 0). The kernel is used as a template or standard; the effect of the calculations below is to find the position in the frame segment shown in *a* for which the surrounding intensity distribution most closely matches that surrounding the centre of the kernel. When a sequence of consecutive video frames is analysed, a single kernel derived from one of the frames is used in the analysis of all of them. The x and y dimensions of the kernel are denoted α and β, respectively; for the case shown here, $\alpha = 27$ pixels and $\beta = 33$ pixels. *c*, Cross-correlation $\mathbf{C}(x, y)$ of the frame segment *a* with a scaled version of the kernel *b*. The cross-corelation calculation

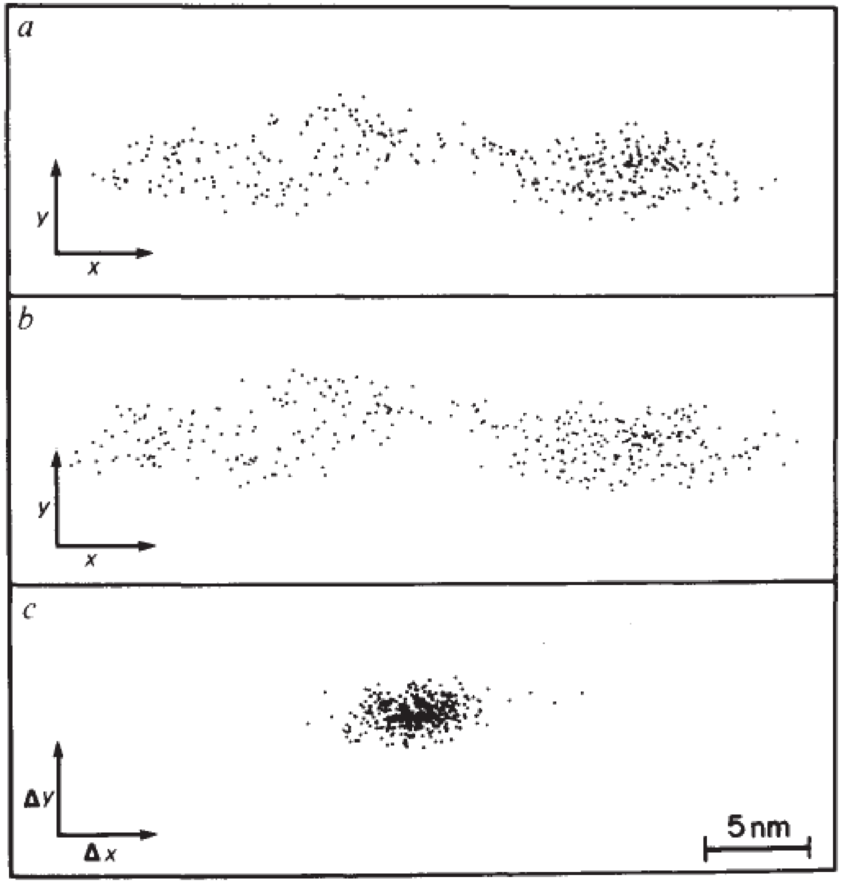

a
y
x
b
y
x
c
Δy
Δx
5 nm

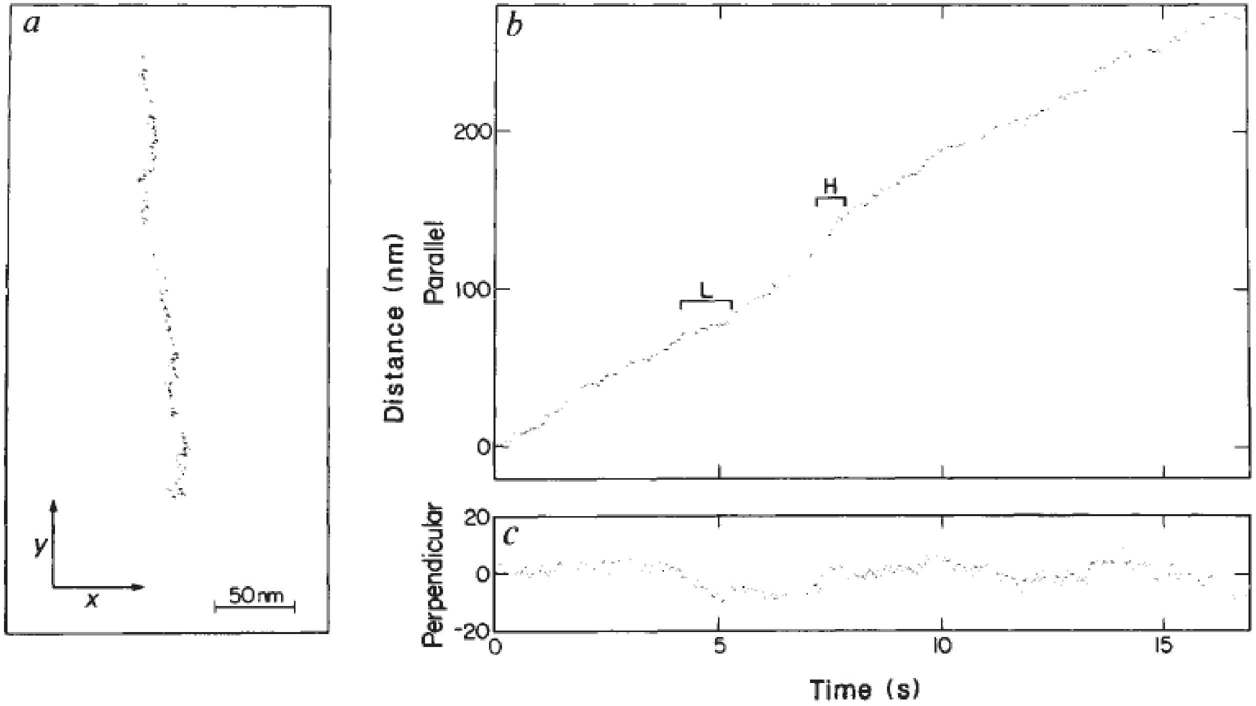

Fig. 3 Motion of a kinesin-coated bead along a microtubule in the presence of 10 μM ATP. *a*, The bead

Fig. 4 Motion of a kinesin-coated bead along a microtubule in the presence of 2.5 μM ATP. The plot shows the projection of the bead position along the microtubule axis as a function of time. The mean velocity along the microtubule axis over the period shown is 3.9 nm s^{-1} (~0.8% of maximal velocity). Forward movement in region A occurs smoothly with a mean velocity of 5.6 nm s^{-1}. Movement in region B occurs in four discrete jumps (arrows) of length 3.7 ± 1.7 nm (mean ± s.d.).

Methods. The sample was identical to that of Fig. 3, except for a lower ATP concentration (2.5 μM). The data-analysis procedure was identical to that of Fig. 3 except that microtubule orientation was determined manually from the positions of video cursors superimposed on the centre of the microtubule image at distances of 0.5 μm on either side of the microtubule segment on which the bead motion occurred.

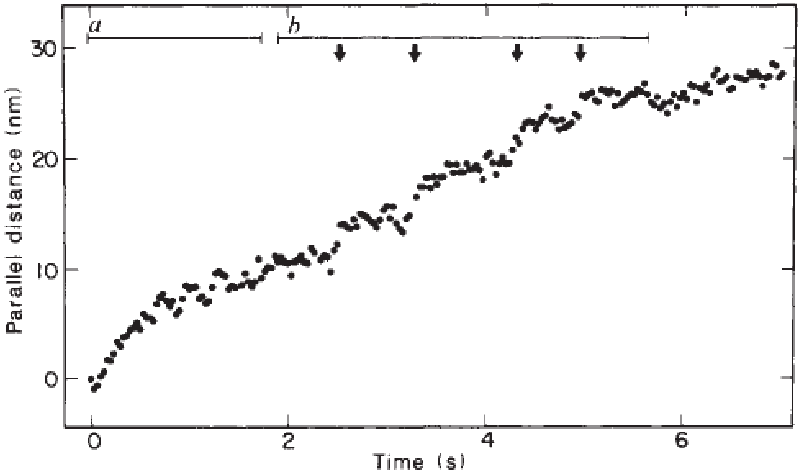

Localization

$$I(x, y) = I_{\text{background}} + A.$$

$$\exp\left\{-{}^{1}/_{2}\left[\left(\frac{x - x_0}{s_x}\right)^2 + \left(\frac{y - y_0}{s_y}\right)^2\right]\right\},$$

$$\sigma_{x,y}^{\mu}$$

$$= \sqrt{\frac{s_{x,y}^{2}}{N_{\text{photons}}} + \frac{a^2}{12.N_{\text{photons}}} + \frac{8.\pi.s_{x,y}^{4}.b^2}{a^2.N_{\text{photons}}}},$$

Fluorescence Imaging with One Nanometer Accuracy (FIONA)

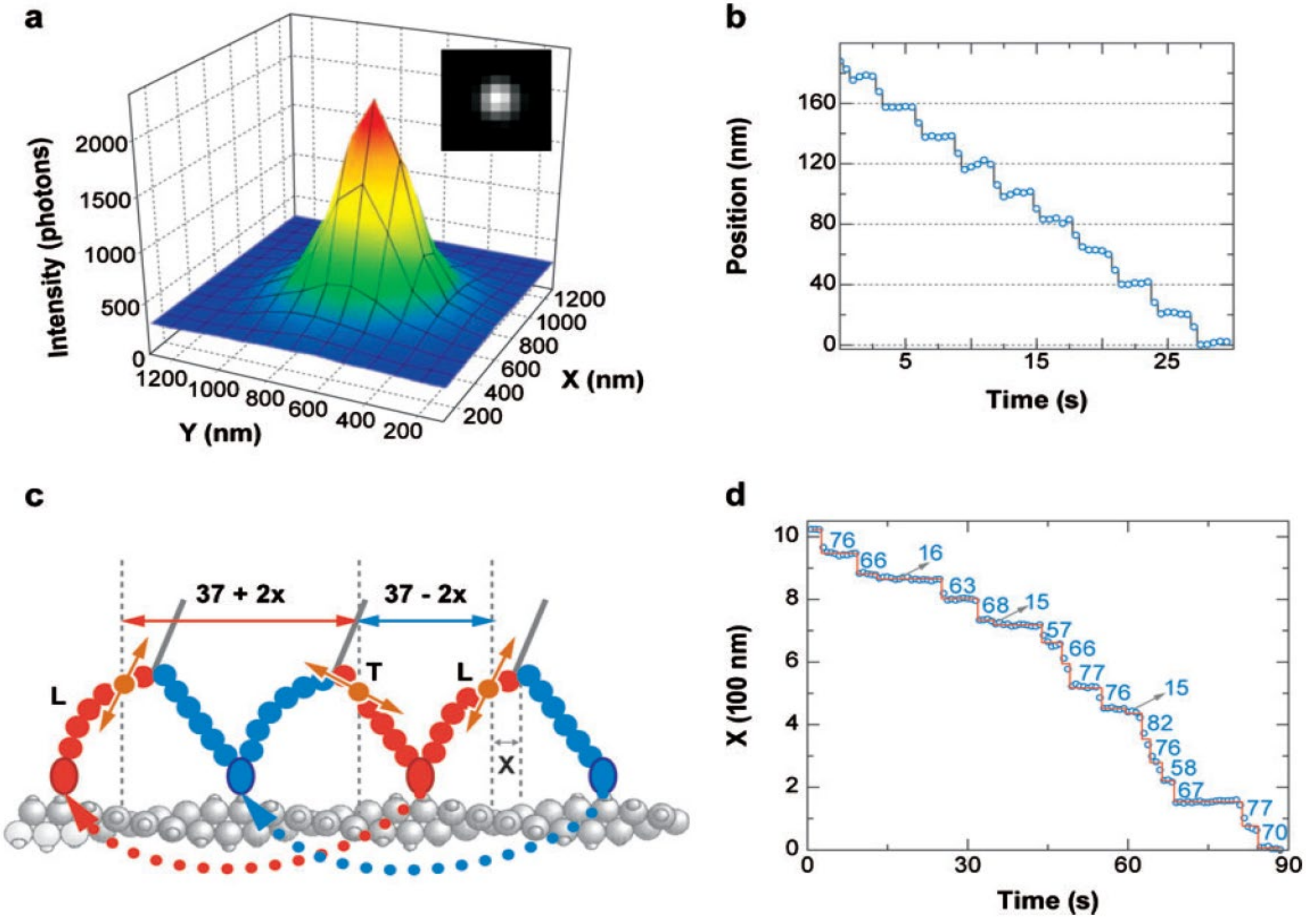

Fluorescence Imaging with One-Nanometer Accuracy (FIONA)

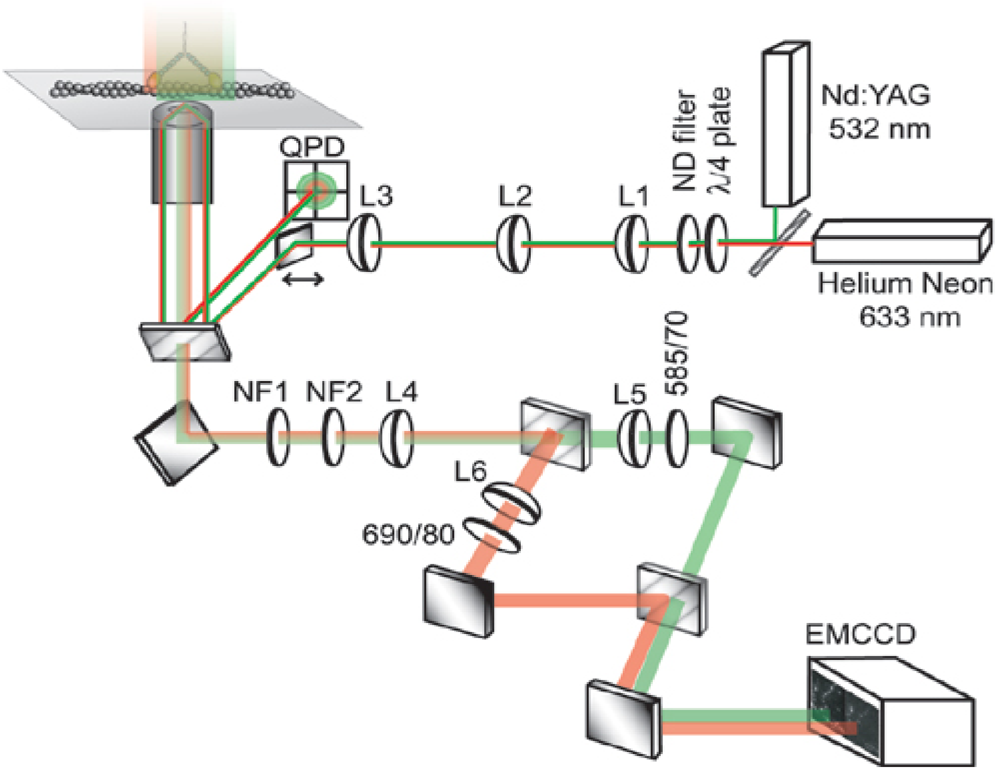

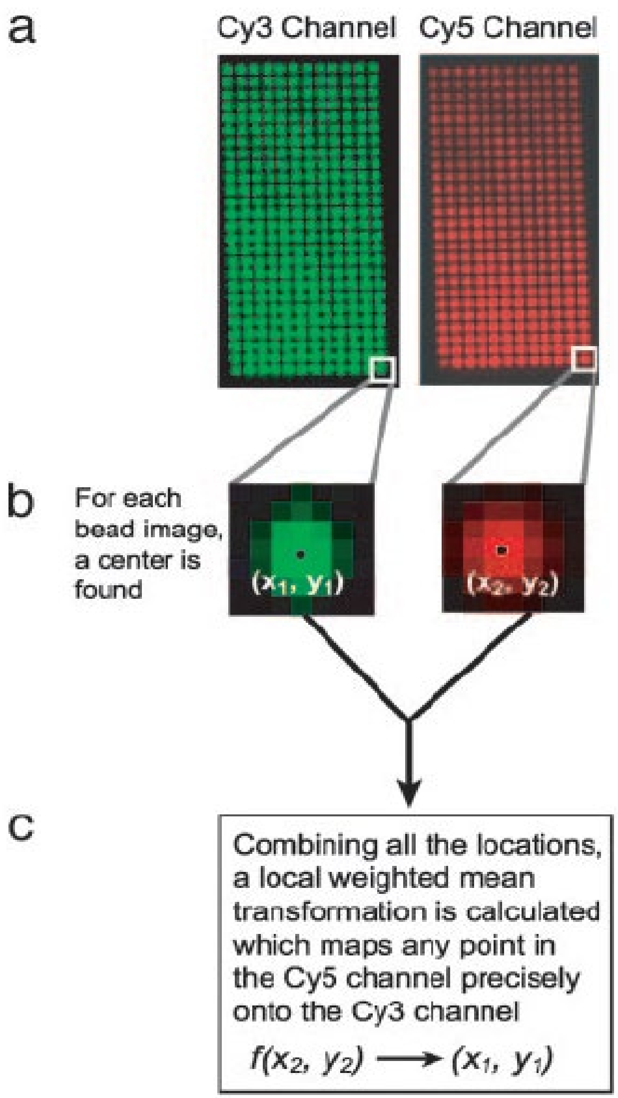

For each bead image, a center is found

Combining all the locations, a local weighted mean transformation is calculated which maps any point in the Cy5 channel precisely onto the Cy3 channel

$$f(x_2, y_2) \longrightarrow (x_1, y_1)$$

PNAS | February 1, 2005 | vol. 102 | no. 5 | 1419–1423

$$f(x, y) = z_0 + A \, \exp\left(\frac{1}{2}\left[\left(\frac{x-\mu_x}{\sigma_x}\right)^2 + \left(\frac{y-\mu_y}{\sigma_y}\right)^2\right]\right)$$

$$\sigma_\mu = \sqrt{(\sigma_x^2 + \sigma_y^2)} \Big/ \sqrt{N_\gamma - 1}.$$

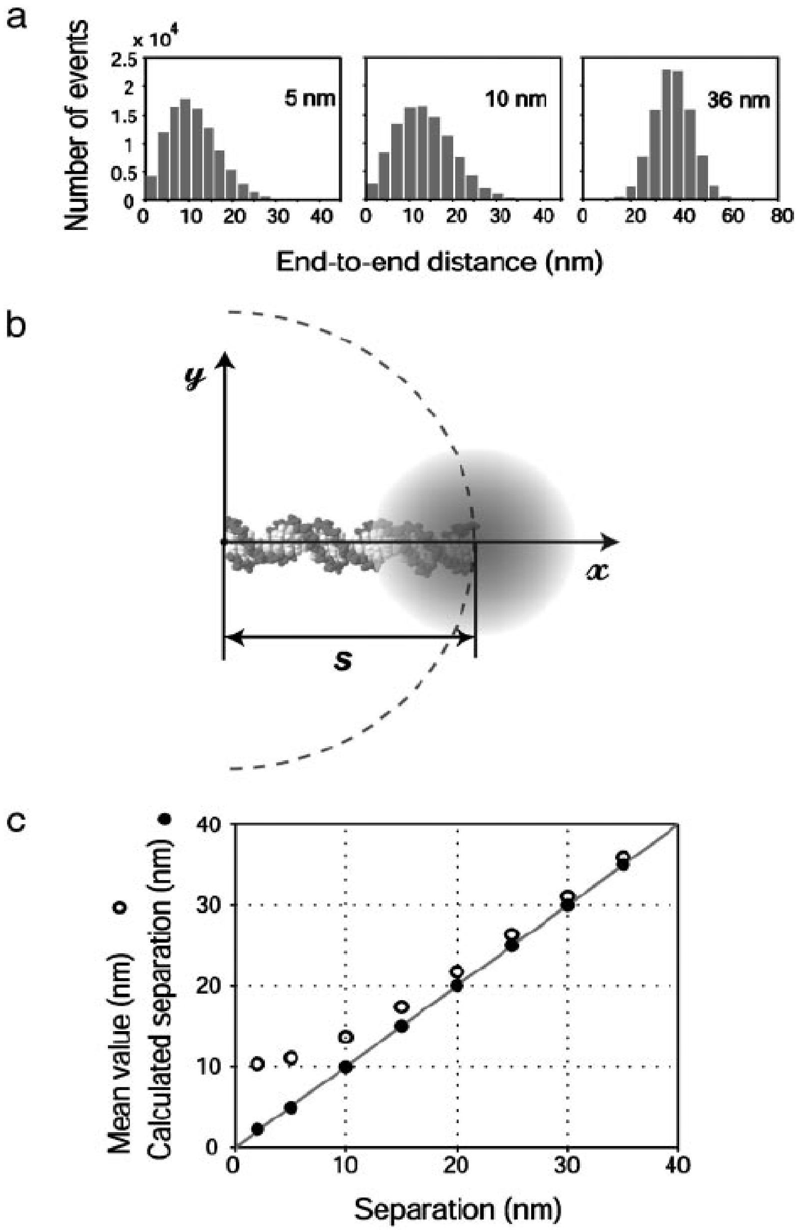

Fig. 2. Determining the accurate end-to-end distance from the skewed distribution of distance measurements. (*a*) The distance probability distribution was calculated by means of Monte Carlo simulations. (*b*) The skew in the histograms toward large values can be understood from a geometric argument. If one end of the DNA molecule is measured to reside at the origin, then only points lying on the circumference of a circle with radius *s* and origin (0, 0) will yield the true end-to-end distance. It is more likely that a point will lie outside of the dashed-line semicircle than inside it, which gives the distance distribution a long tail. (*c*) Despite the non-Gaussian nature of the distance distribution, the end-to-end separation can be calculated using the geometric mean, variance, and localization errors.

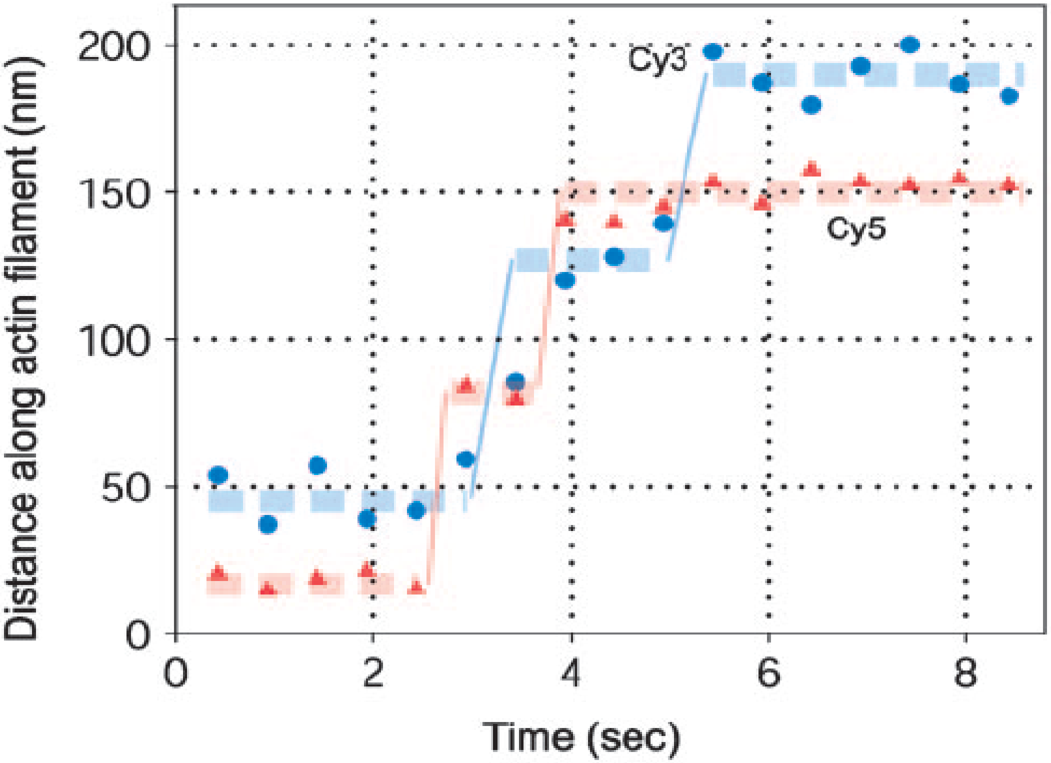

Fig. 4. Time trace of a differentially labeled myosin V molecule walking along an actin filament. The labels (Cy3 and Cy5) are covalently attached to calmodulins that were exchanged onto the myosin V molecule. In this trace, both of the fluorescent probe's locations are taking 72-nm steps, indicating that the calmodulins were exchanged close to the motor domain. The alternating positions of the probes provide a direct observation of myosin V's hand-over-hand walking mechanism.

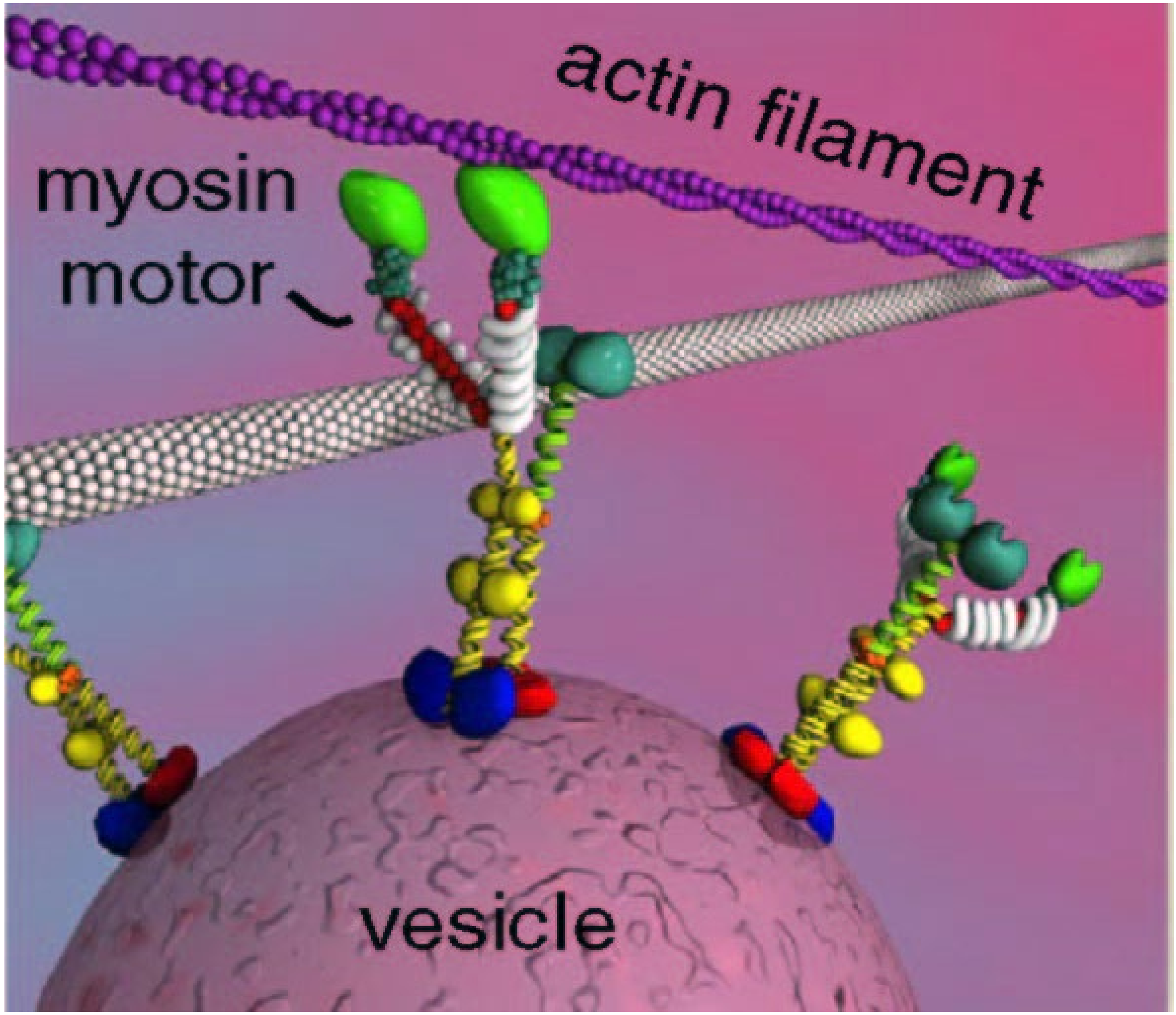
actin filament
myosin motor
vesicle

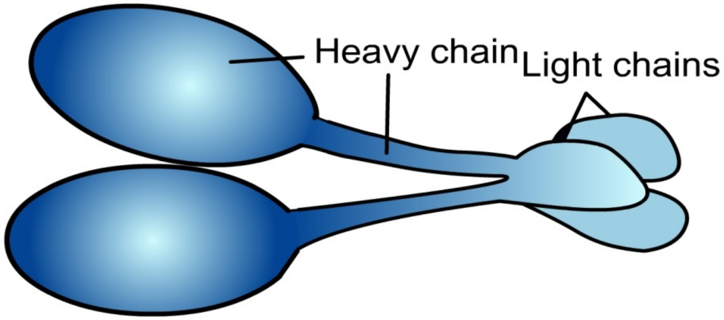
Heavy chain
Light chains

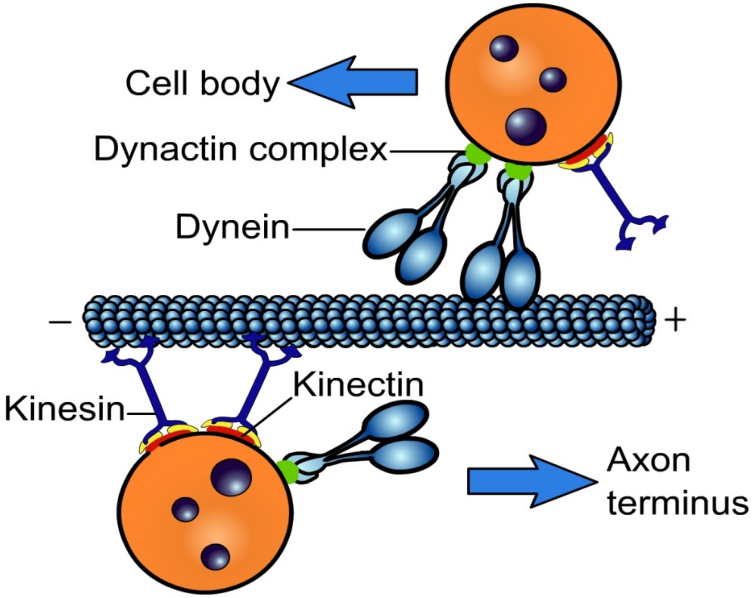
Cell body
Dynactin complex
Dynein
–
+
Kinesin
Kinectin
Axon
terminus

Kinesin and Dynein Move a Peroxisome in Vivo: A Tug-of-War or Coordinated Movement?

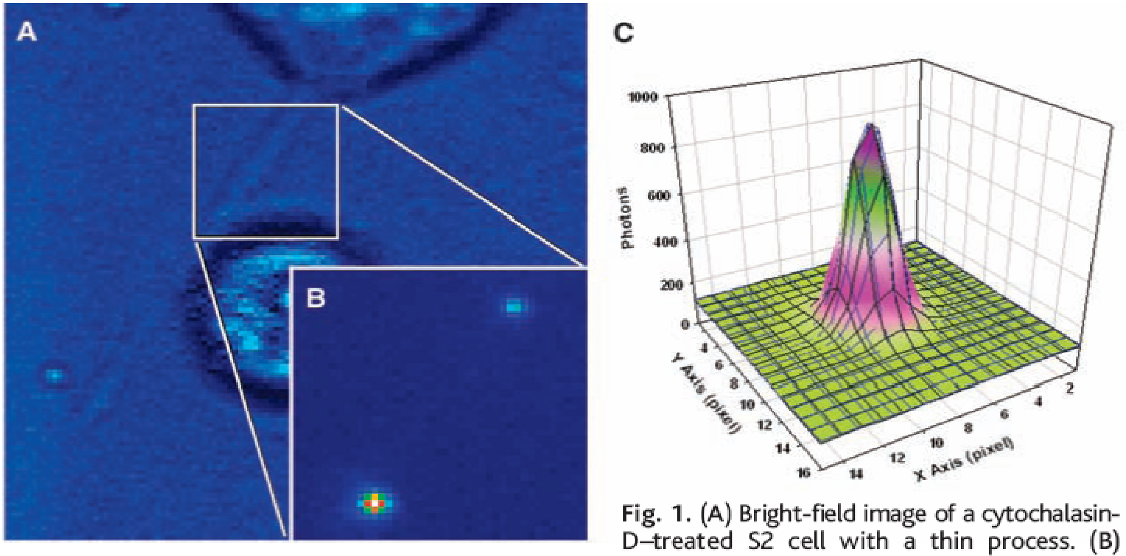

Fig. 1. (A) Bright-field image of a cytochalasin-D–treated S2 cell with a thin process. (B) Fluorescence image of the GFP-labeled peroxisomes within the process. (C) Fluorescence image of a peroxisome can be fit to a two-dimensional Gaussian (correlation coefficient $r^2 = 0.992$), enabling the center to be determined to 1.5 nm within 1.1 ms.

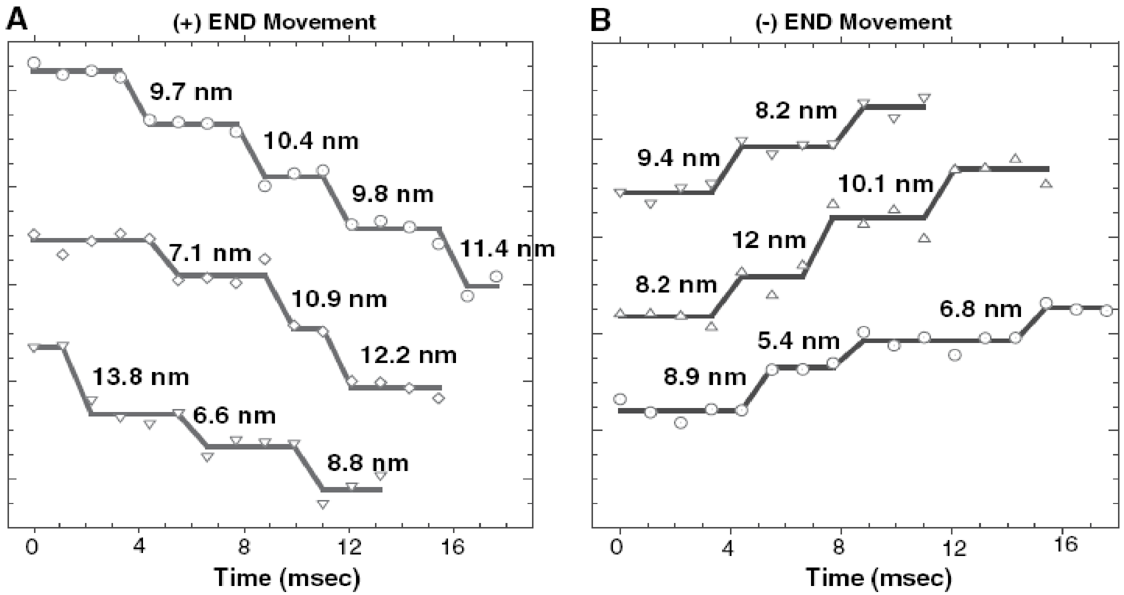

SCIENCE VOL 308 3 JUNE 2005

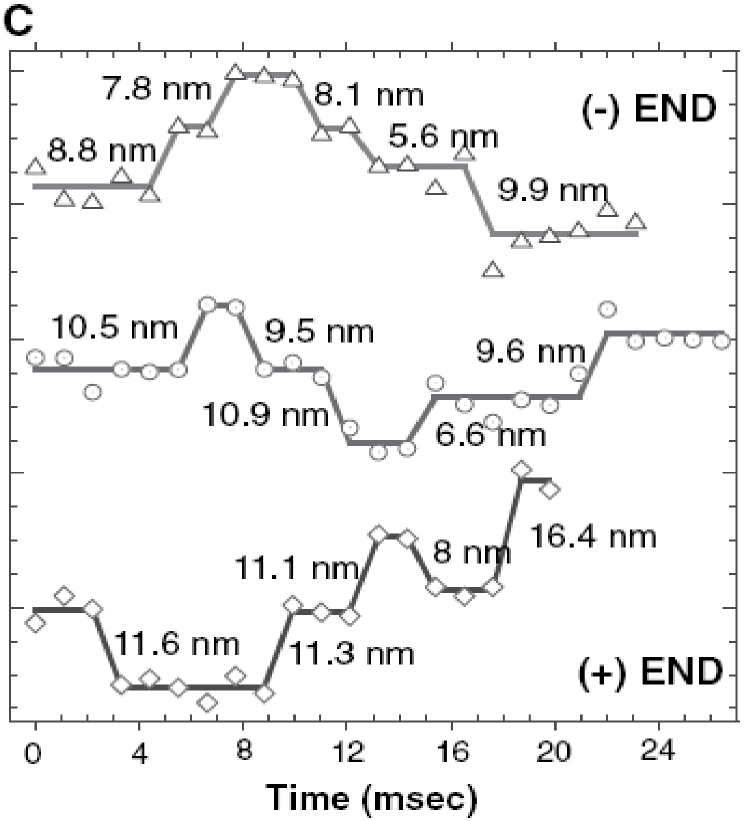

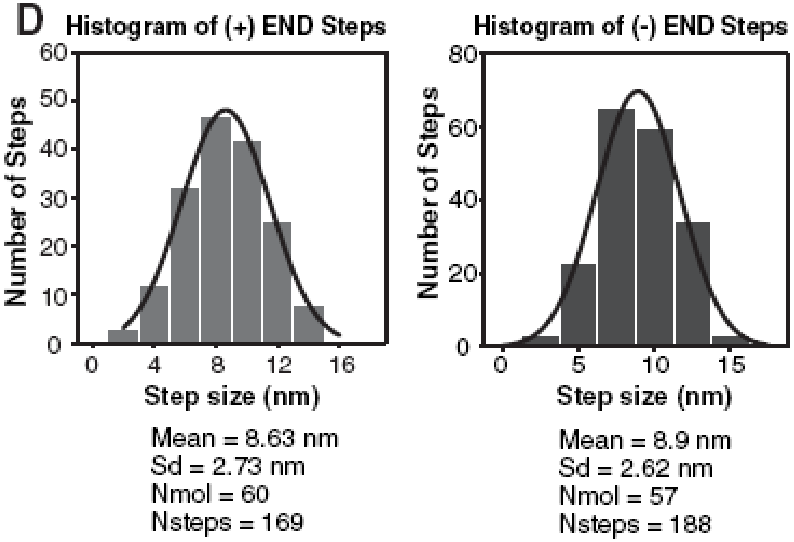

Fig. 2. Step-by-step movement of peroxisomes carried by (A) a single kinesin, (B) a single dynein, and (C) a coordination of kinesin and dynein. (D) Histograms of the individual steps of anterograde (kinesin) and retrograde (dynein) movement. A pairwise displacement of kinesin and dynein, showing the multiples of 8-nm displacement, is shown in fig. S6.

Single-molecule High-Resolution Colocalization (SHREC)

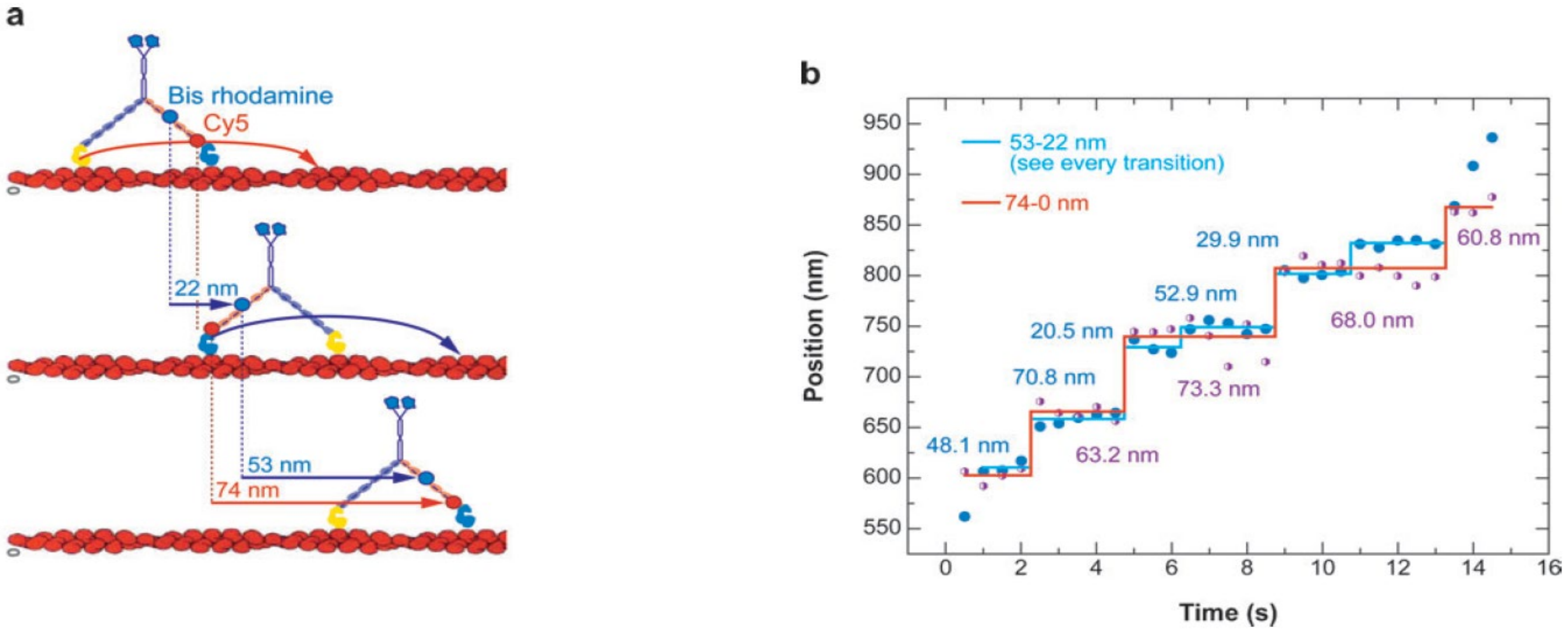

February 1, 1995 / Vol. 20, No. 3 / OPTICS LETTERS 237

Proposed method for molecular optical imaging

E. Betzig

Here an alternative approach is proposed in which multiple discrete features within the same focal volume are spatially resolved in two steps (see Fig. 1). First, each feature is identified and isolated through one or more distinguishing optical characteristics. Second, each feature is localized; that is, its spatial coordinates are determined, on a scale that is small compared with the focal volume, either by measurement of the center of the point-spread function (PSF) associated with each feature[2] or by application of a spatial gradient,[3,4] as discussed below. The complete set of coordinates for all features can then be used to reconstruct the final image in which the relative positions of the features are shown.

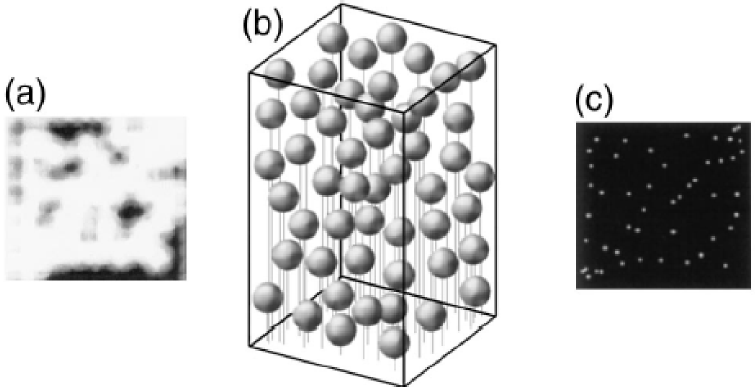

Fig. 1. (a) Field of discrete features as conventionally imaged in m spatial dimensions with a broad PSF. (b) Same features after isolation in $m + n$ dimensions on the basis of n distinguishing optical characteristics. (c) Final image reconstructed at resolution $\delta\mathbf{x}$ given by the uncertainty in the measured position of each isolated feature. In general, $|\delta\mathbf{x}| \ll$ PSF.

Photoactivation localization microscopy (PALM)

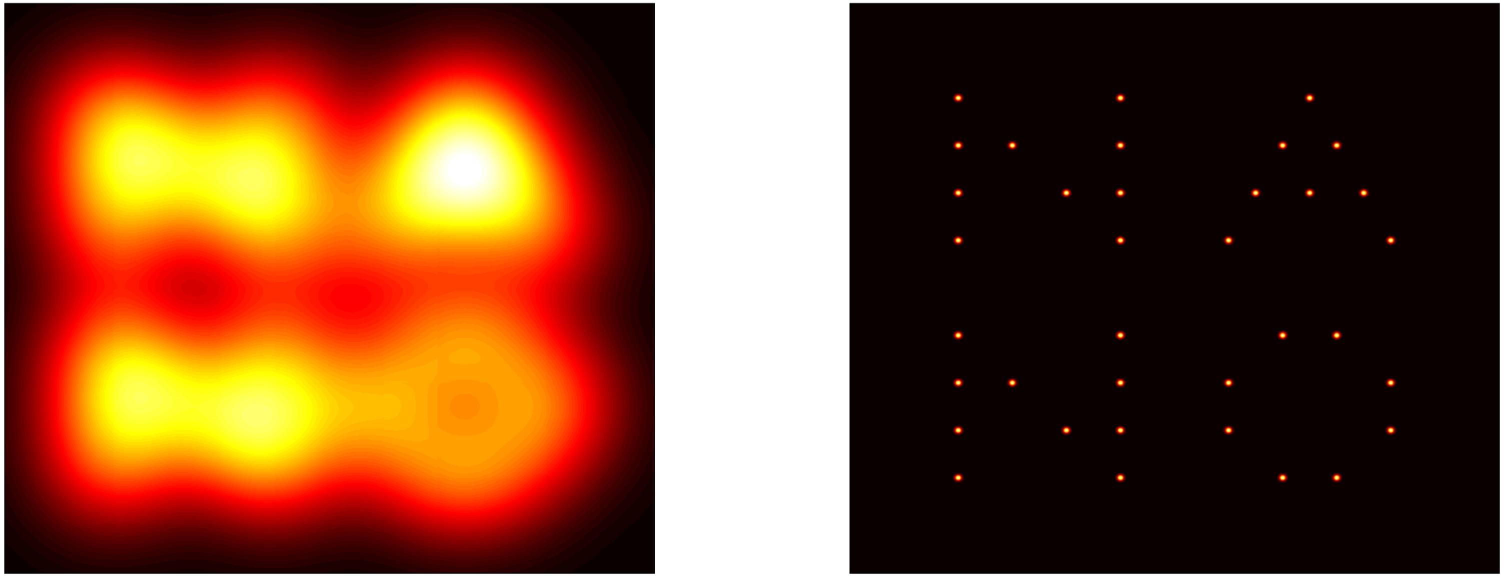

Diffraction-limited system:

Lateral resolution $\Delta xy \approx 0.61\ \lambda$ / N.A.

$\approx$ 200 nm

Axis resolution $\Delta z \approx 2\lambda$ / N.A.^{2}

$\approx$ 450 nm

Mean-squared position error:

$$\left(\sigma_{x,y}^{2}\right)_{m} \approx \frac{s^{2}+a^{2}/12}{N_{m}}+\frac{4\sqrt{\pi}s^{3}b_{m}^{2}}{aN_{m}^{2}}$$

s is the standard deviation of the PSF.
a is the pixel size in the image
N_m is the total number of photons measured from molecule *m*
b_m is the number of background photons collected in the fitting window

Russell E. Thompson, Daniel R. Larson, and Watt W. Webb, **Biophysical Journal** 82, 2775 (2002).
Eric Betzig, et al., **Science** 313, 1642 (2006).

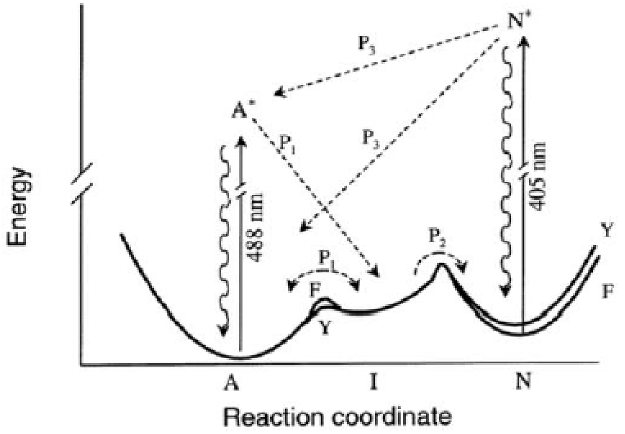

Figure 7: (Dickson *et al.*, 1997, *Nature* 388, 355-358). GFP in state A is excited to A* and returns to A upon photon emission. When I is reached from A, there is no fluorescence until I spontaneously moves to A: blinking. When I moves to N, there is no fluorescence until N is activated to N* by 405 nm excitation and GFP returns to A.

Imaging Intracellular Fluorescent Proteins at Nanometer Resolution

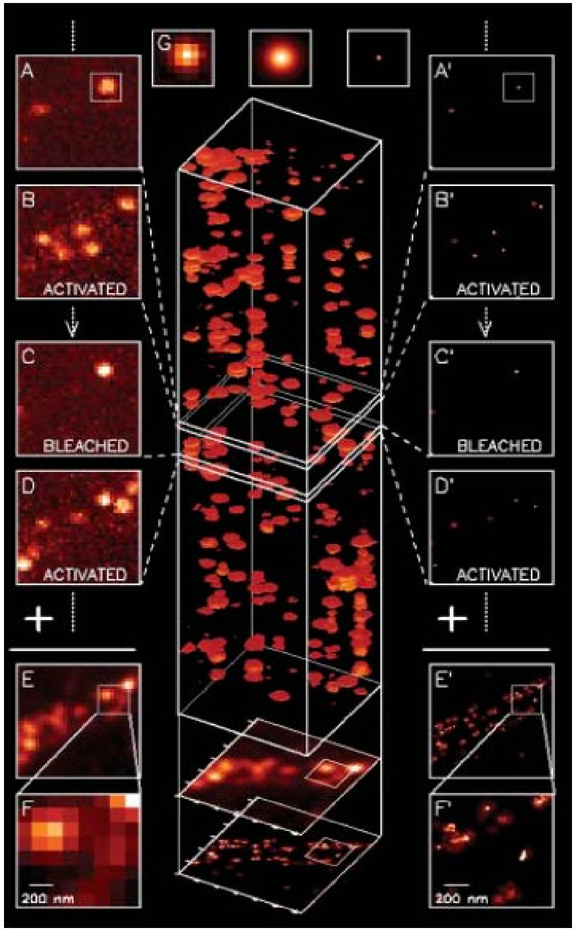

$$(\sigma_{x,y}{}^2)_m \approx \frac{s^2 + a^2/12}{N_m} + \frac{4\sqrt{\pi}\, s^3 b_m{}^2}{aN_m{}^2}$$

15 SEPTEMBER 2006 VOL 313 **SCIENCE**

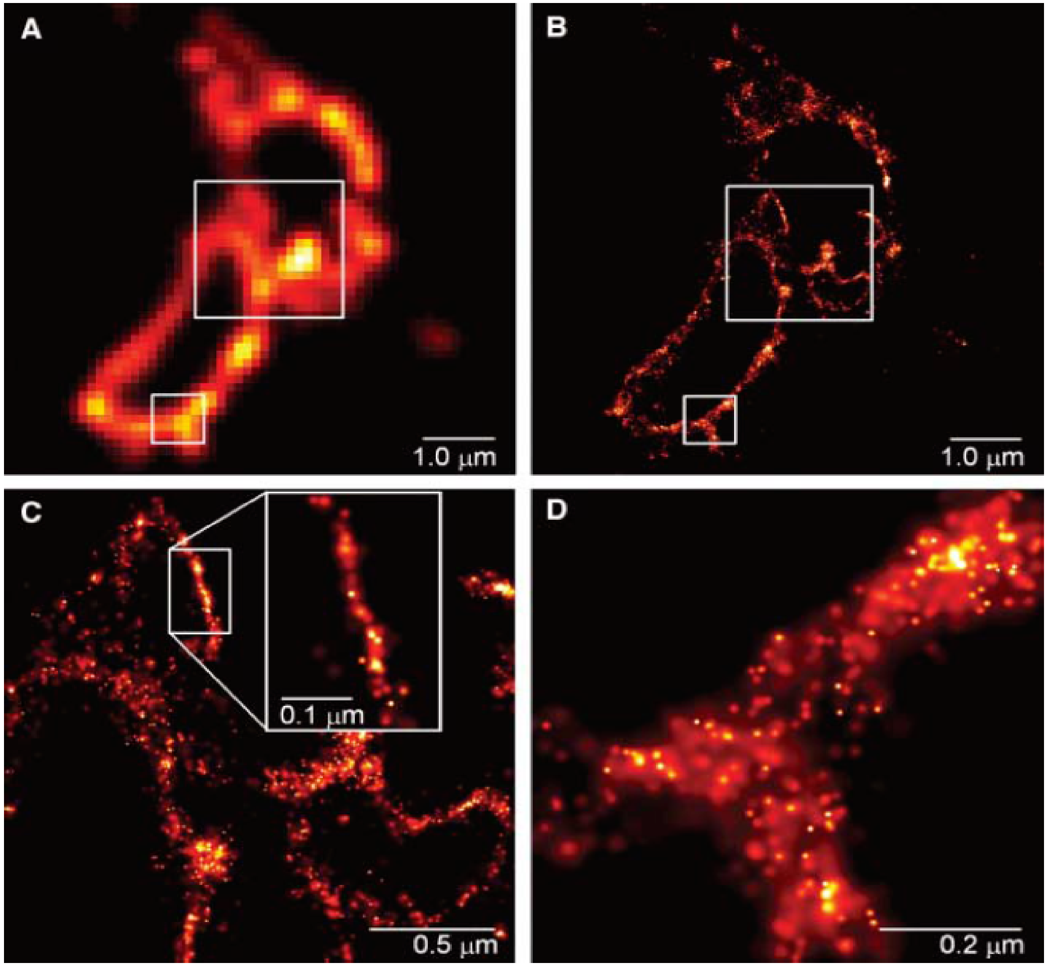

Fig. 2. Comparative summed-molecule TIRF (**A**) and PALM (**B**) images of the same region within a cryo-prepared thin section from a COS-7 cell expressing the lysosomal transmembrane protein CD63 tagged with the PA-FP Kaede. The larger boxed region in (B), when viewed at higher magnification (**C**) reveals smaller associated membranes that may represent interacting lysosomes or late endosomes that are not resolvable by TIRF. In a region where the section is nearly orthogonal to the lysosomal membrane, the most highly localized molecules fall on a line of width ~10 nm (inset). In an obliquely cut region [(**D**), from the smaller boxed region in (B)], the distribution of CD63 within the membrane plane can be discerned.

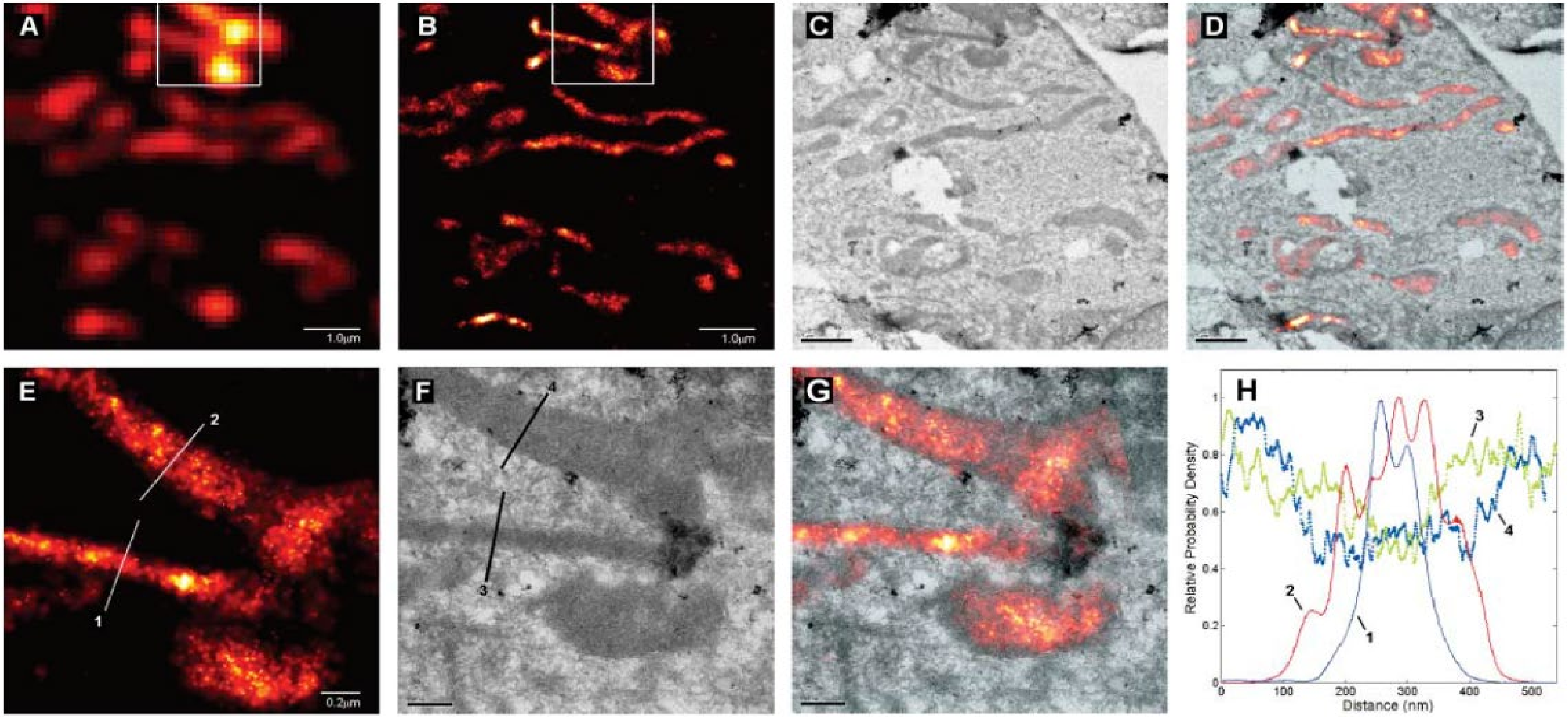

Fig. 3. Comparative summed-molecule TIRF (**A**), PALM (**B**), TEM (**C**), and PALM/TEM overlay (**D**) images of mitochondria in a cryo-prepared thin section from a COS-7 cell expressing dEosFP-tagged cytochrome-C oxidase import sequence. Higher magnification PALM (**E**), TEM (**F**), and overlay (**G**) images within the box in (B) reveal that these matrix reporter molecules extend up to, but not into, the ~20-nm outer mitochondrial membrane. The molecular distribution across two mitochondria along lines 1 and 2 in PALM image (E) are compared in (**H**) to the TEM signal along lines 3 and 4 in (F) across the same mitochondria. Scale bars: 1.0 μm in (A) to (D); 0.2 μm in (E) to (G).

Sub-diffraction-limit imaging by stochastic optical reconstruction microscopy (STORM)

Michael J Rust[1,5], Mark Bates[2,5] & Xiaowei Zhuang[1,3,4]

NATURE METHODS

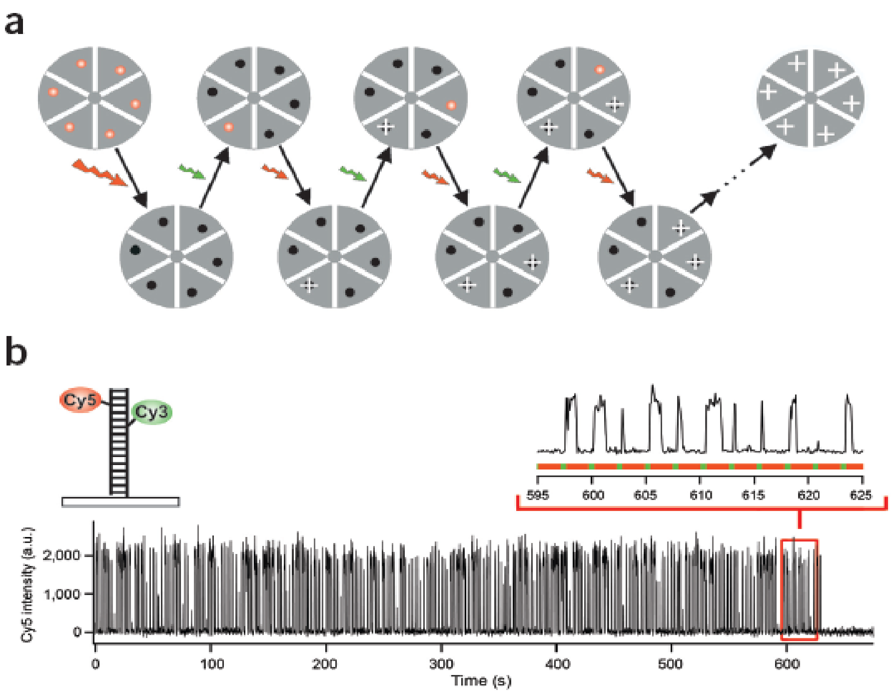

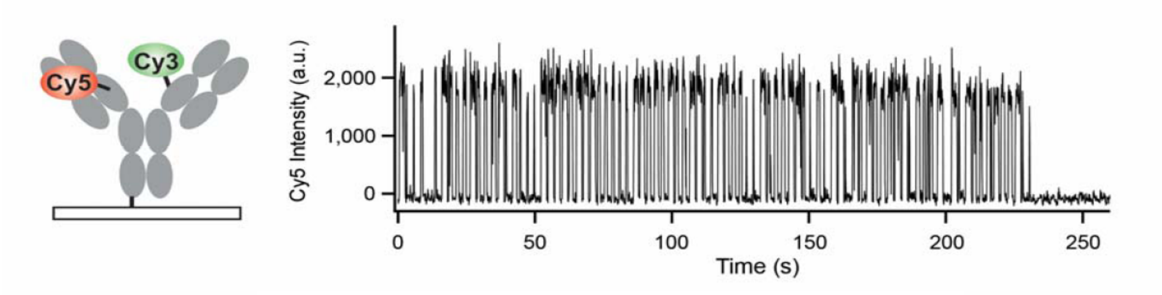

2.2 : 1 for Cy3 and 0.1 : 1 for Cy5

Goat anti-mouse secondary antibody labeled with the cyanine switch exhibits photoswitching behavior similar to switch-labeled DNA. The antibody was labeled with Cy3 and Cy5 (as described in **Supplementary Methods** online) and bound to a quartz slide coated with unlabeled mouse anti-transferrin primary antibody. The trace shows the Cy5 fluorescence intensity detected from a single labeled antibody as it switches on and off until permanent photobleaching occurs after 230 seconds. A red laser (633 nm, 30 W/cm^2) is used to excite fluorescence from Cy5 and to switch Cy5 to the dark state. A green laser (532 nm, 1 W/cm^2) is used to switch the Cy5 back to the fluorescent state. The sample was excited with a sequence of alternating green and red laser pulses (0.5 s green followed by 2 s red).

$$I(x,y) = A + I_0 e^{\left[-(x'/a)^2-(y'/b)^2\right]/2}$$

$$x' = (x - x_0)\cos\theta - (y - y_0)\sin\theta$$
$$y' = (x - x_0)\sin\theta + (y - y_0)\cos\theta$$

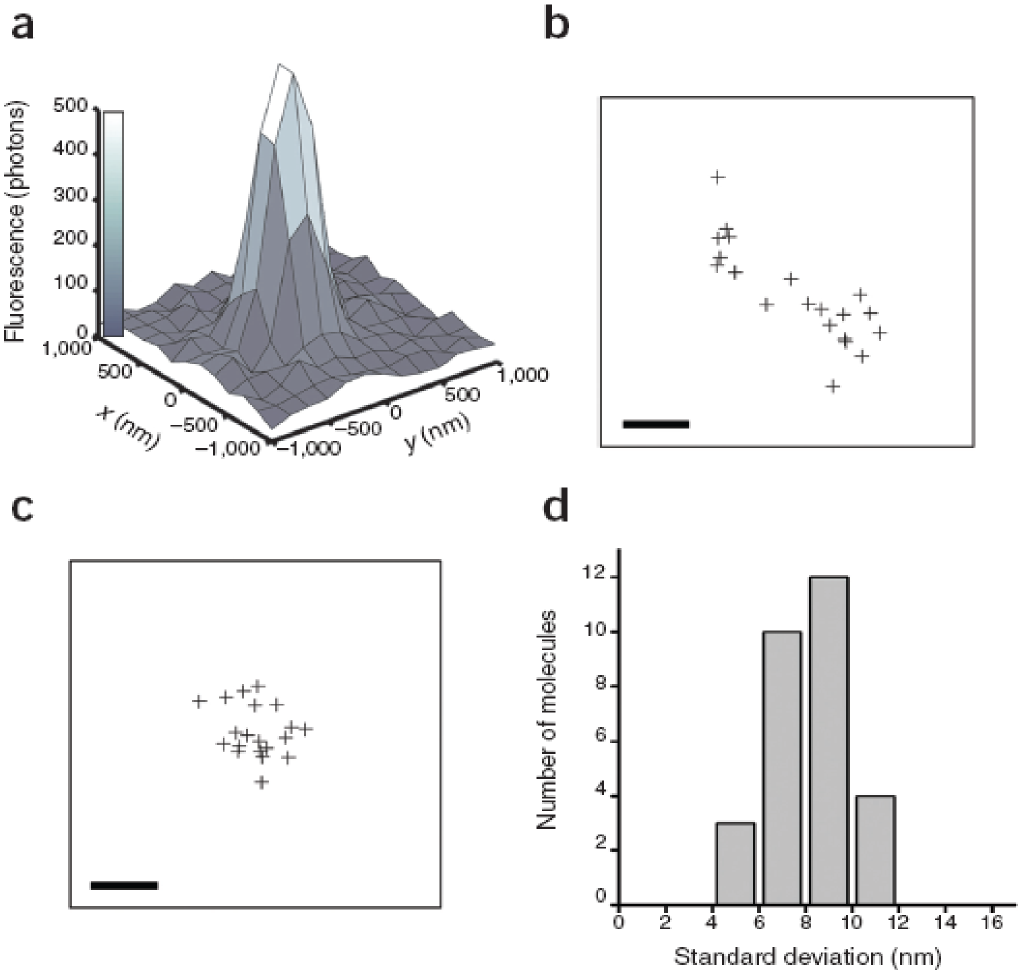

Figure 2 | The high localization accuracy of individual switches during each switching cycle defines the intrinsic resolution of STORM. (**a**) The point spread function (PSF) of the emission from a single switch on DNA during a single switching cycle. Fitting the PSF to a two-dimensional Gaussian (not shown) gives the centroid position of the PSF. (**b**,**c**) The centroid positions of an individual switch determined in 20 successive imaging cycles before (**b**) and after (**c**) correction for sample drift. Scale bars, 20 nm. (**d**) A histogram of the standard deviation of centroid positions. The standard deviation is determined as $(\sigma_x + \sigma_y) / 2$ for each switch using 20 imaging cycles, where σ_x and σ_y are the standard deviations of the centroid positions in the *x* and *y* dimensions. This histogram was constructed from 29 switches.

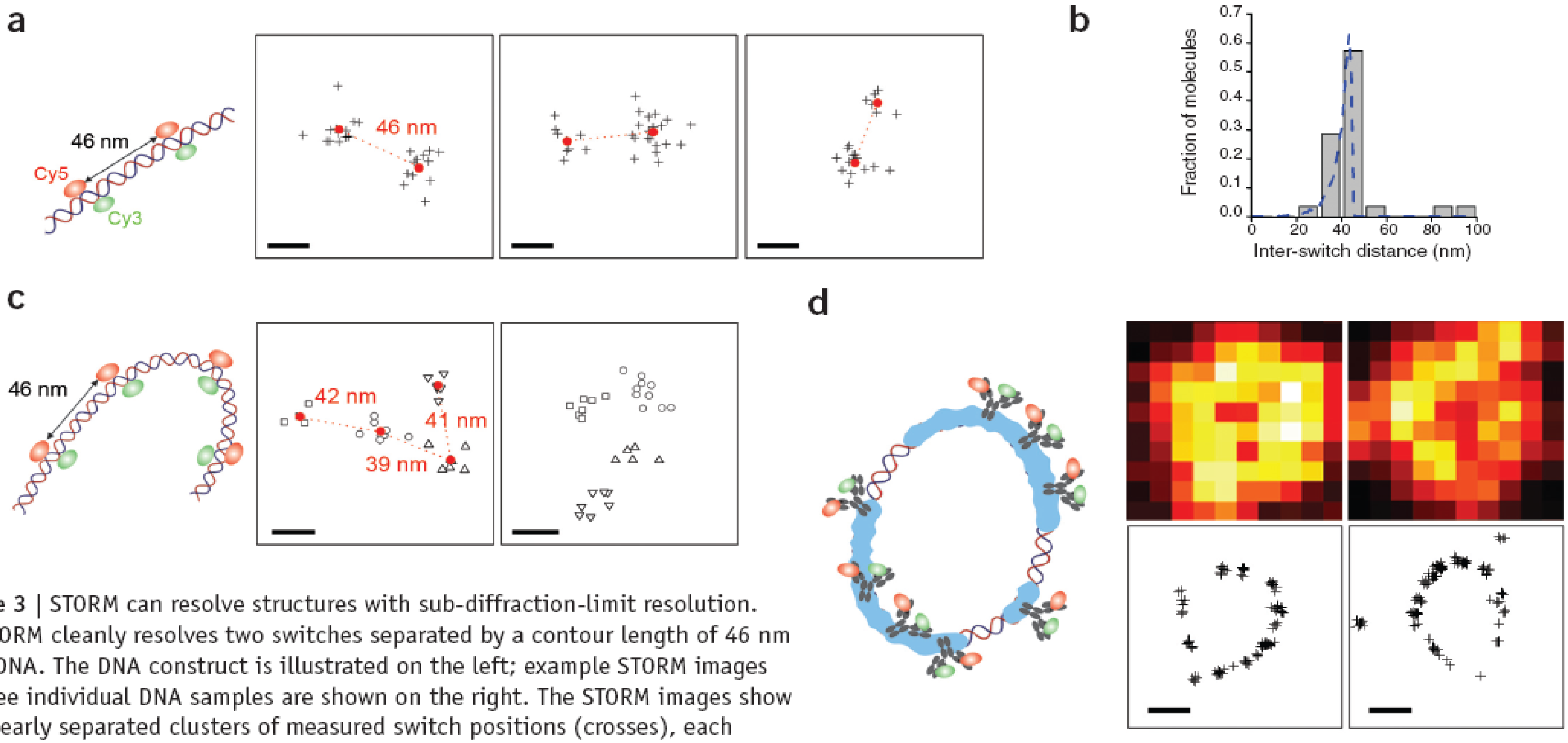

Figure 3 | STORM can resolve structures with sub-diffraction-limit resolution. (**a**) STORM cleanly resolves two switches separated by a contour length of 46 nm on dsDNA. The DNA construct is illustrated on the left; example STORM images of three individual DNA samples are shown on the right. The STORM images show two clearly separated clusters of measured switch positions (crosses), each corresponding to a single switch. The center-of-mass position of each cluster is marked by a red dot. The inter-switch distances are 46 nm, 44 nm and 34 nm for these three examples. Scale bars, 20 nm. (**b**) Comparison between the inter-switch distances measured using STORM (columns) and the predicted distance distribution considering the flexibility of DNA (dashed line). (**c**) STORM images of four switches attached to a dsDNA, pair-wise separated by a contour length of 46 nm. The measured switch positions are clustered by an automated algorithm and different clusters are indicated by different symbols. Scale bars, 20 nm. (**d**) STORM images of RecA-coated circular plasmid DNA. Indirect immunofluorescence images with switch-labeled secondary antibody taken by a total internal reflection microscope (top); the reconstructed STORM images of the same filaments (bottom). Scale bars, 300 nm.

Multicolor Super-Resolution Imaging with Photo-Switchable Fluorescent Probes

SCIENCE VOL 317 21 SEPTEMBER 2007

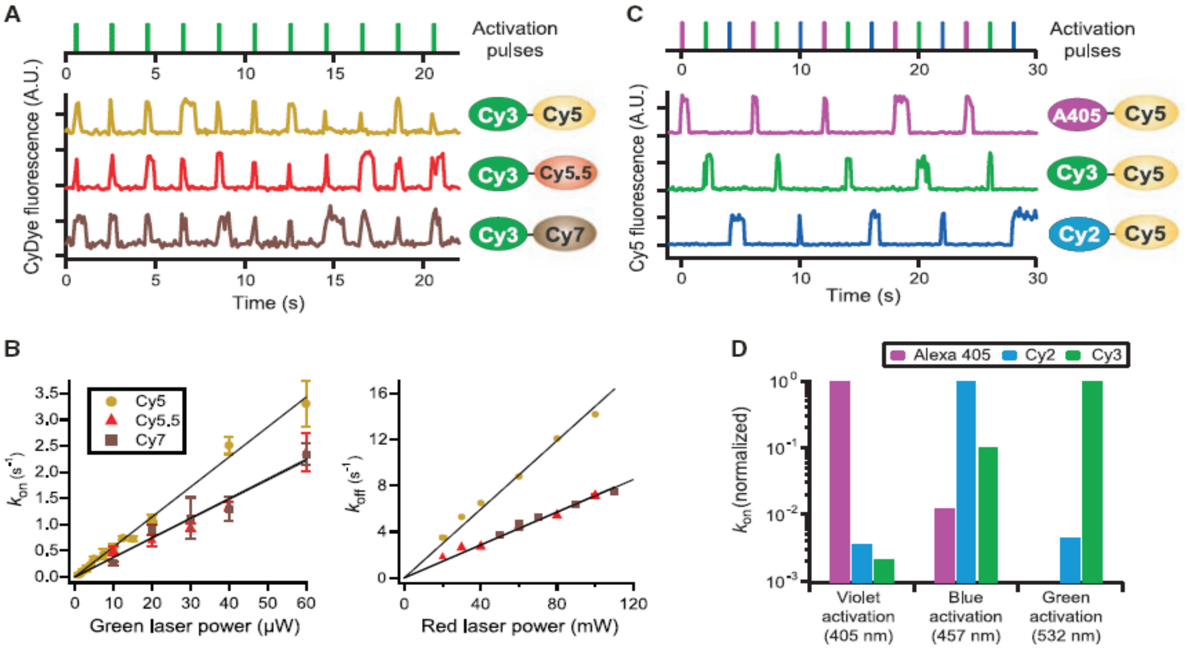

Fig. 1. Photo-switchable probes constructed from activator-reporter pairs. (**A**) Spectrally distinct reporters exhibit photo-switching behavior. The lower panel shows the fluorescence time traces of three photo-switchable reporters Cy5 (dark yellow line), Cy5.5 (red line), and Cy7 (brown line), each paired with a Cy3 dye as the activator on a DNA construct. The upper panel shows the green laser pulses (532 nm) used to activate the reporters. The red laser (657 nm) was continuously on, serving to excite fluorescence from the reporters and to switch them to the dark state. Traces were shifted relative to each other for clarity. (**B**) Switching rate constants k_{on} and k_{off} of the Cy3-Cy5, Cy3-Cy5.5, and Cy3-Cy7 pairs as a function of green and red laser power. Error bars indicate SEM from about three data sets. The laser power to intensity calibration may vary between different samples because of moderate differences in the laser spot size at the sample. (**C**) The same reporter can be activated by spectrally distinct activators. The lower panel shows the fluorescence time traces of Cy5 paired with three different activators, Alexa 405 (magenta line), Cy2 (blue line), and Cy3 (green line). The upper panel shows the violet (405 nm, magenta line), blue (457 nm, blue line), and green (532 nm, green line) activation pulses. (**D**) Normalized activation rate constants of the three dye pairs at three activation wavelengths: 405, 457, and 532 nm. The k_{on} values of Alexa 405-Cy5, Cy2-Cy5, and Cy3-Cy5 were used for normalization at 405, 457, and 532 nm, respectively. The absolute activation rates were rapid for each pair at its corresponding optimal wavelength, with values of 10 s^{-1} or greater at only a few hundred μW of laser power. The activation rate of the Alexa 405-Cy5 pair by the 532-nm laser was too small to be measured reliably.

Fig. 2. Three-color STORM imaging of a model DNA sample. (**A**) Three-color STORM image of three different DNA constructs labeled with Alexa 405-Cy5, Cy2-Cy5, or Cy3-Cy5 mixed at a high surface density on a microscope slide. The image was plotted by rendering each localization as a Gaussian peak, the width of which was scaled with the theoretical localization accuracy given by the number of photons detected (*26*). Each colored spot in this image represents a cluster of localizations from a single DNA molecule. A conventional fluorescence image of the same area is shown in fig. S3 for comparison. (**B** and **C**) Higher-magnification views of the boxed regions in (A) show several examples of closely spaced DNA molecules. Each localization was plotted as a cross, colored according to the following code: If the molecule was activated by a 405-, 457-, or 532-nm laser pulse, the color of the cross was assigned as blue, green, or red, respectively. (**D**) The localization distributions of the blue, green, or red clusters. The two-dimensional histograms of localizations were generated by aligning multiple (50 to 60) clusters by their center of mass. The histograms were fit to a Gaussian profile to determine their FWHM.

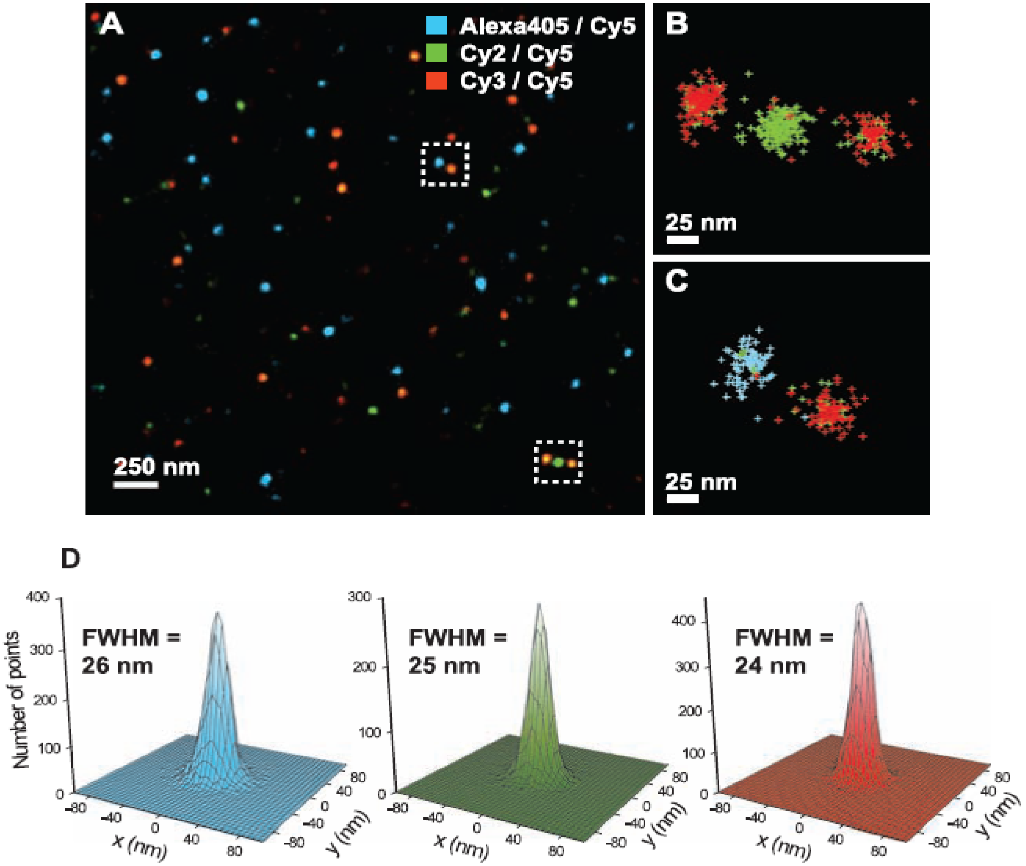

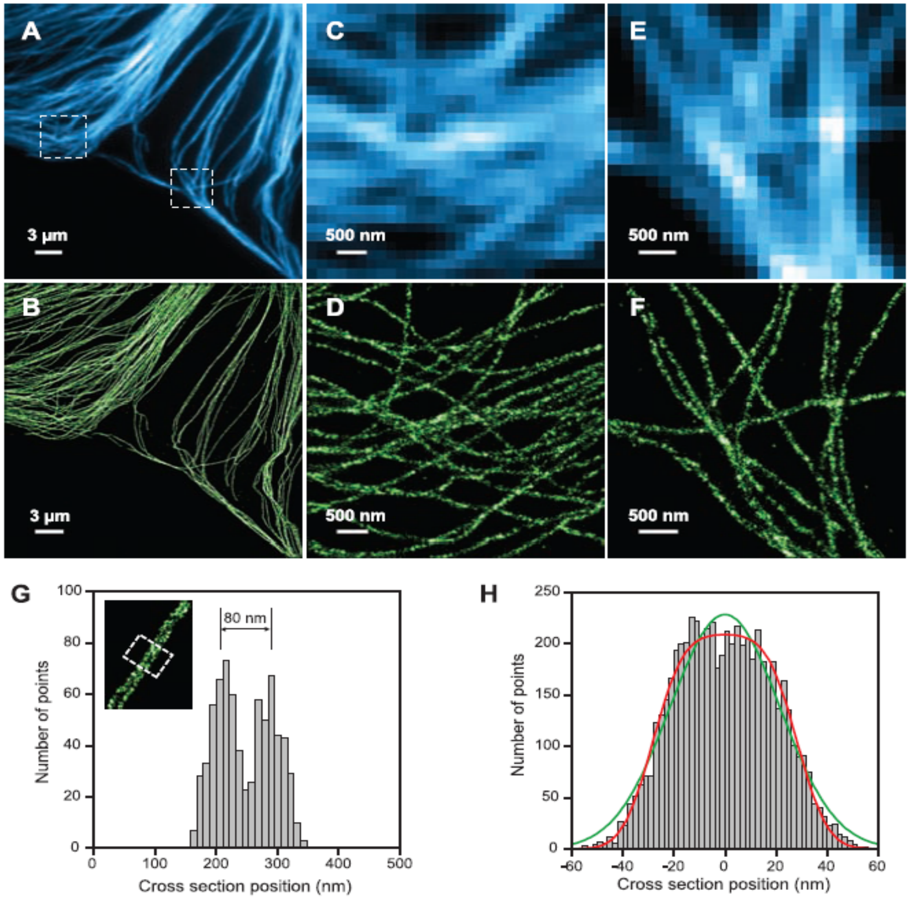

Fig. 3. STORM imaging of microtubules in a mammalian cell. (**A**) Conventional immunofluorescence image of microtubules in a large area of a BS-C-1 cell. (**B**) STORM image of the same area. (**C** and **E**) Conventional and (**D** and **F**) STORM images corresponding to the boxed regions in (A). (**G**) Cross-sectional profiles of two nearby microtubule filaments in the cell. The inset shows the STORM image, and the histogram shows the cross-sectional distribution of localizations within the small regions specified by the white box. (**H**) Cross-sectional profile of a microtubule segment determined from the STORM image. A relatively long segment (~7 µm) was chosen to obtain good statistics. The histogram shows the cross-sectional distribution of localizations. The green line is a single Gaussian fit with FWHM = 51 nm. The red line shows the fit obtained by convolving a rectangular function of width = *d* with a Gaussian function of FWHM = *r*. The fit yields *d* = 56 nm and *r* = 22 nm, corresponding to the antibody-coated microtubule width and the imaging resolution, respectively.

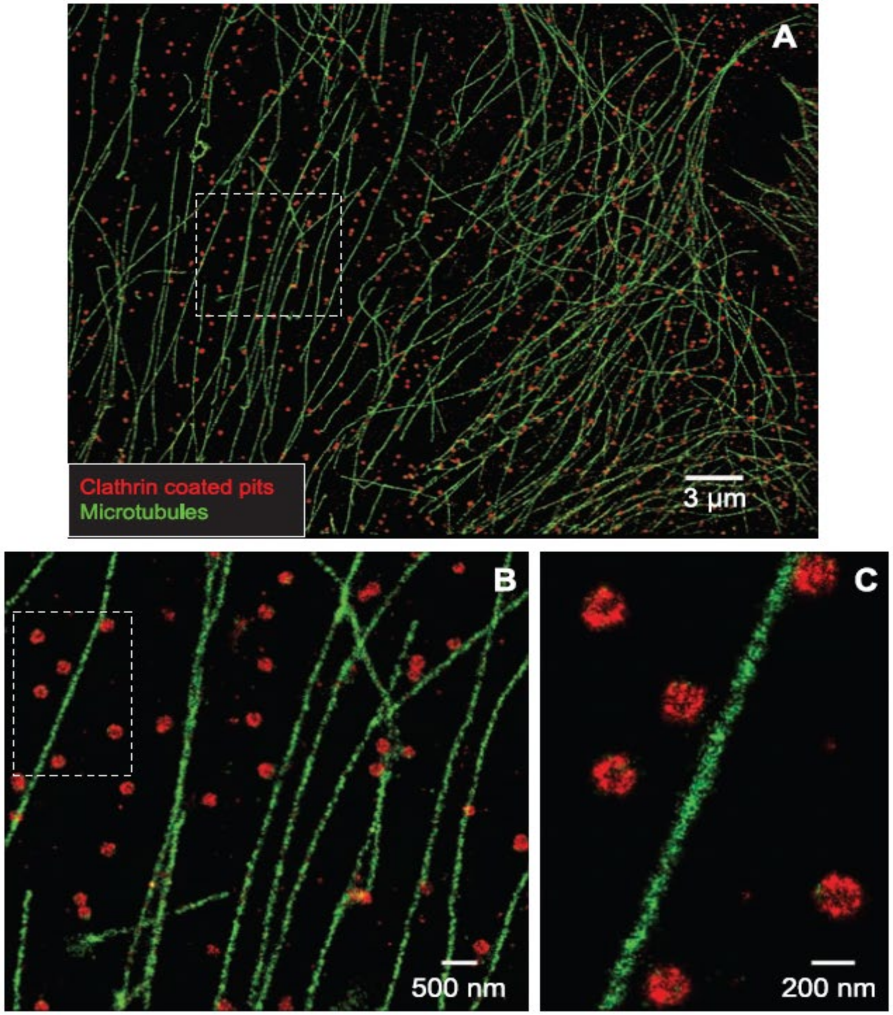

Fig. 4. Two-color STORM imaging of microtubules and CCPs in a mammalian cell. (**A**) STORM image of a large area of a BS-C-1 cell. The secondary antibodies used for microtubule staining were labeled with Cy2 and Alexa 647, and those for clathrin were labeled with Cy3 and Alexa 647. The 457- and 532-nm laser pulses were used to selectively activate the two pairs. Each localization was false colored according to the following code: green for 457-nm activation and red for 532-nm activation. (**B**) STORM image corresponding to the boxed region in (A) shown at a higher magnification. (**C**) Further magnified view of the boxed region in (B).

Three-Dimensional Super-Resolution Imaging by Stochastic Optical Reconstruction Microscopy

8 FEBRUARY 2008 VOL 319 **SCIENCE**

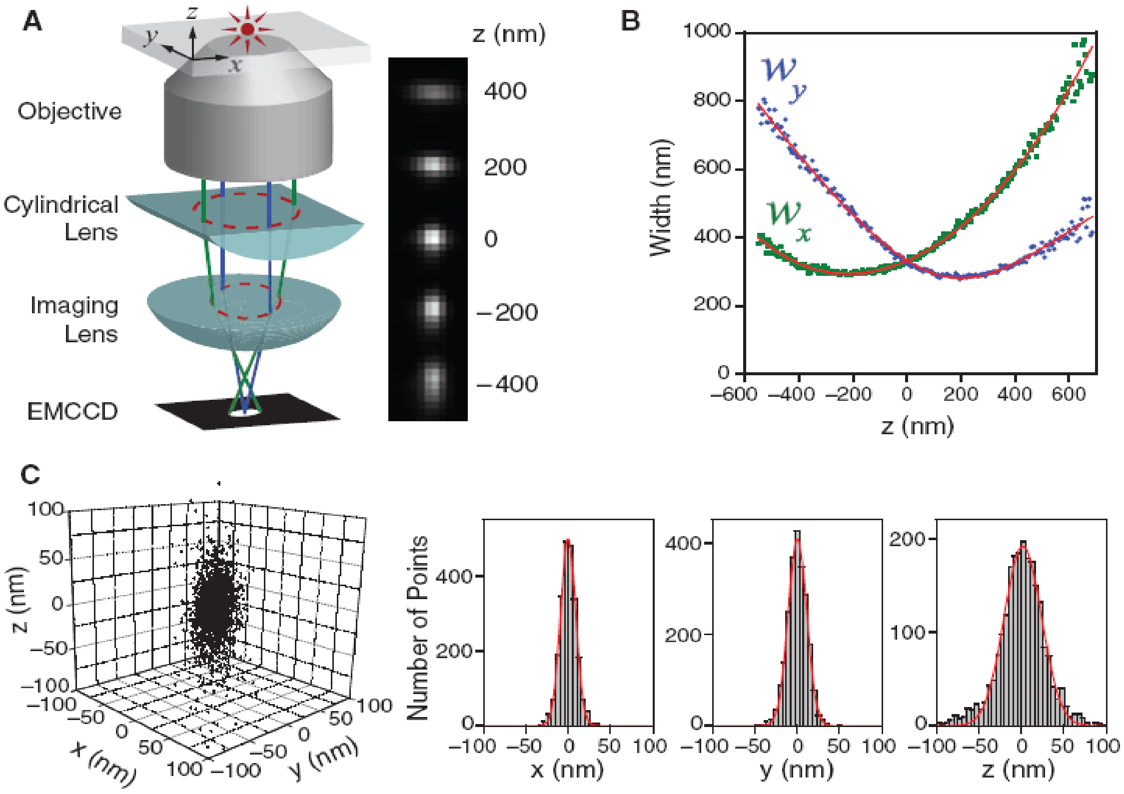

Fig. 1. The scheme of 3D STORM. (**A**) Three-dimensional localization of individual fluorophores. The simplified optical diagram illustrates the principle of determining the z coordinate of a fluorescent object from the ellipticity of its image by introducing a cylindrical lens into the imaging path. The right panel shows images of a fluorophore at various z positions. EMCCD, electron-multiplying charge-coupled device. (**B**) Calibration curve of image widths w_x and w_y as a function of z obtained from single Alexa 647 molecules. Each data point represents the average value obtained from six molecules. The data were fit to a defocusing function (red curve) as described in (*27*). (**C**) Three-dimensional localization distribution of single molecules. Each molecule gives a cluster of localizations due to repetitive activation of the same molecule. Localizations from 145 clusters were aligned by their center of mass to generate the overall 3D presentation of the localization distribution (left panel). Histograms of the distribution in x, y, and z (right panels) were fit to a Gaussian function, yielding standard deviations of 9 nm in x, 11 nm in y, and 22 nm in z.

Fig. 2. Three-dimensional STORM imaging of microtubules in a cell. (**A**) Conventional indirect immunofluorescence image of microtubules in a large area of a BS-C-1 cell. (**B**) The 3D STORM image of the same area, with the *z*-position information color-coded according to the color scale bar. Each localization is depicted in the STORM image as a Gaussian peak, the width of which is determined by the number of photons detected (*5*). (**C** to **E**) The *x-y*, *x-z*, and *y-z* cross sections of a small region of the cell outlined by the white box in (B), showing five microtubule filaments. Movie S1 shows the 3D representation of this region, with the viewing angle rotated to show different perspectives (*27*). (**F**) The *z* profile of two microtubules crossing in the *x-y* projection but separated by 102 nm in *z*, from a region indicated by the arrow in (B). The histogram shows the distribution of *z* coordinates of the localizations, fit to two Gaussians with identical widths (FWHM = 66 nm) and a separation of 102 nm (red curve). The apparent width of 66 nm agrees quantitatively with the convolution of our imaging resolution in *z* (represented by a Gaussian function with FWHM of 55 nm) and the previously measured width of antibody-coated microtubules (represented by a uniform distribution with a width of 56 nm) (*5*).

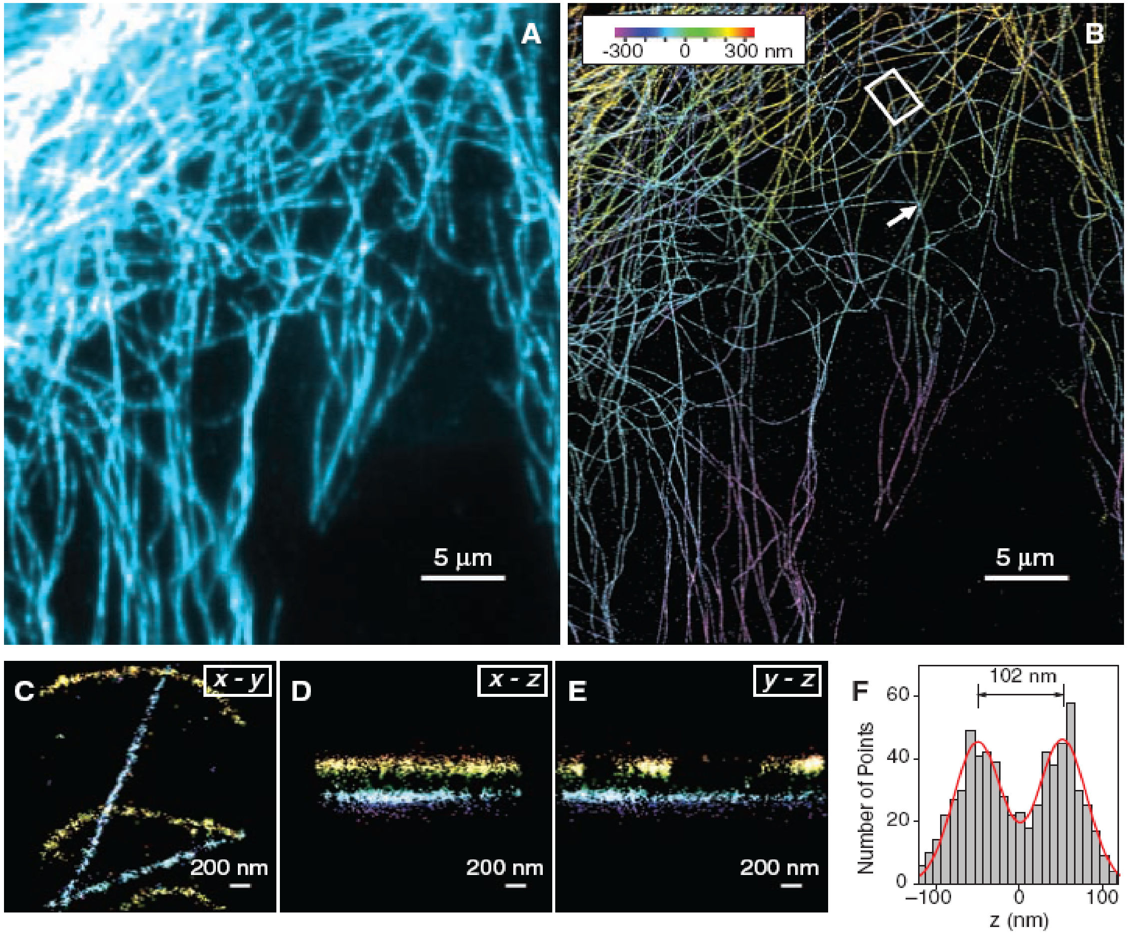

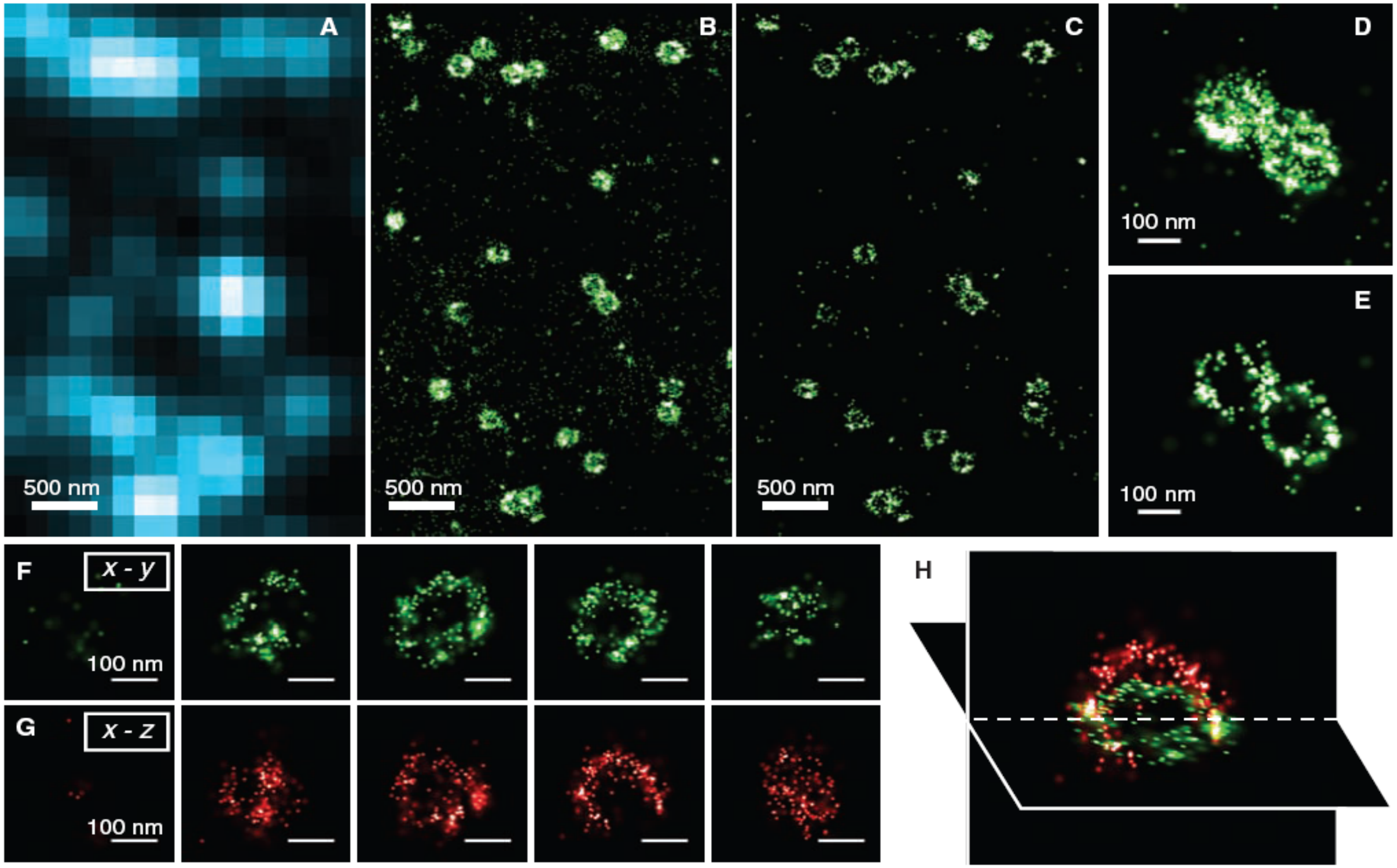

Fig. 3. Three-dimensional STORM imaging of clathrin-coated pits in a cell. (**A**) Conventional direct immunofluorescence image of clathrin in a region of a BS-C-1 cell. (**B**) The 2D STORM image of the same area, with all localizations at different *z* positions included. (**C**) An *x-y* cross section (50 nm thick in *z*) of the same area, showing the ring-like structure of the periphery of the CCPs at the plasma membrane. (**D** and **E**) Magnified view of two nearby CCPs in 2D STORM (D) and their *x-y* cross section (100 nm thick) in the 3D image (E). (**F** to **H**) Serial *x-y* cross sections (each 50 nm thick in *z*) (F) and *x-z* cross sections (each 50 nm thick in *y*) (G) of a CCP, and an *x-y* and *x-z* cross section presented in 3D perspective (H), showing the half-spherical cage-like structure of the pit.

Direct stochastic optical reconstruction microscopy (dSTORM)

Reversible photoswitching mechanism of standard fluorophores

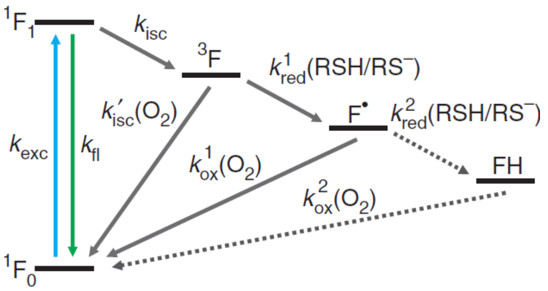

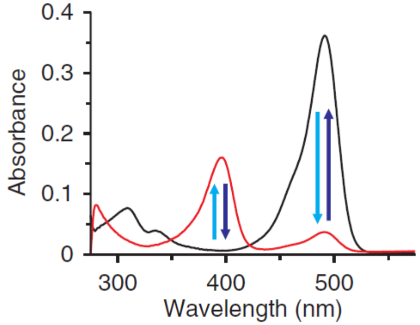

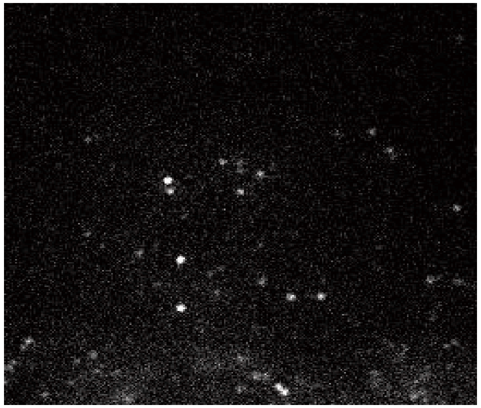

Localization imaging concept

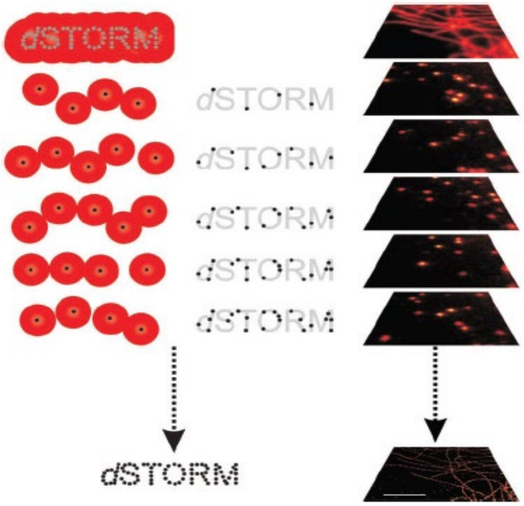

Multicolor imaging

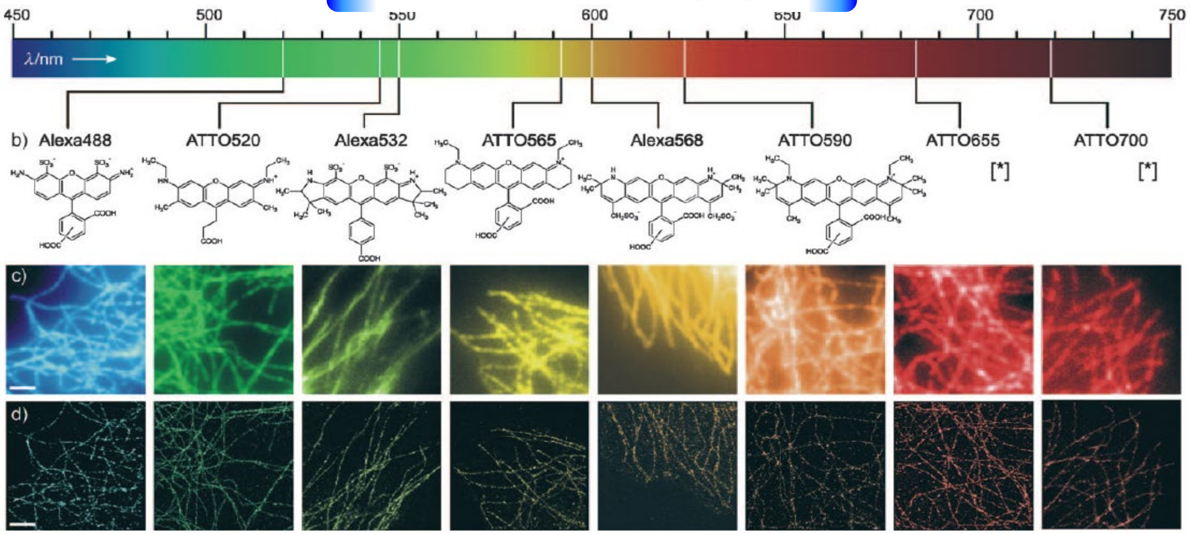

Angew. Chem. Int. Ed. 2008, 2009, Nature protocols 2011

Focal adhesion complexes on HS and pattern ECM surface

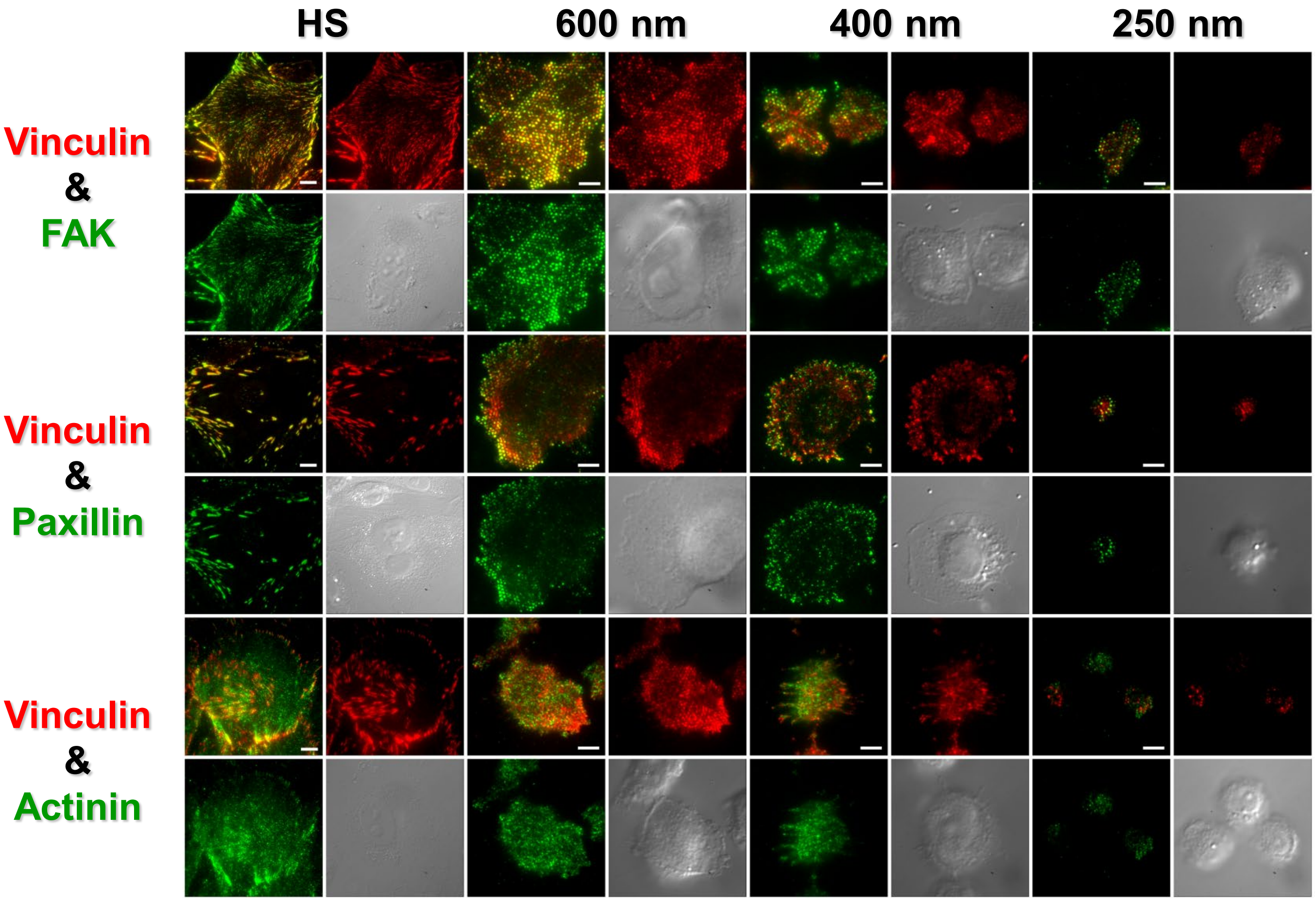

Multicolor superresolution fluorescence imaging

Objective

1. Characteristic distance between focal adhesion complexes.
2. Cross-correlation between different focal adhesion complexes.
3. Number of focal adhesion complexes at different adhesion types.

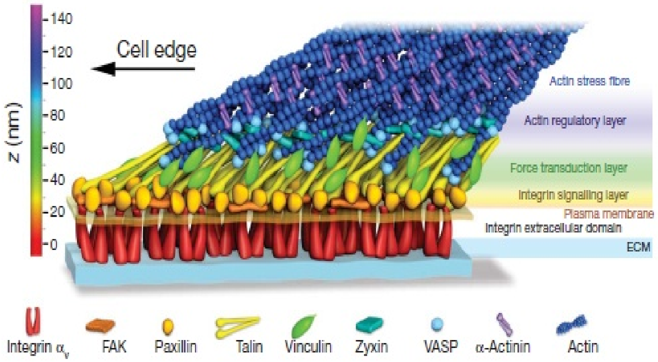

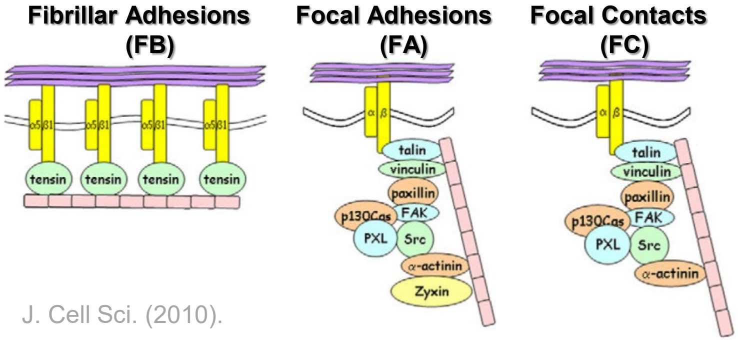

J. Cell Sci. (2010).

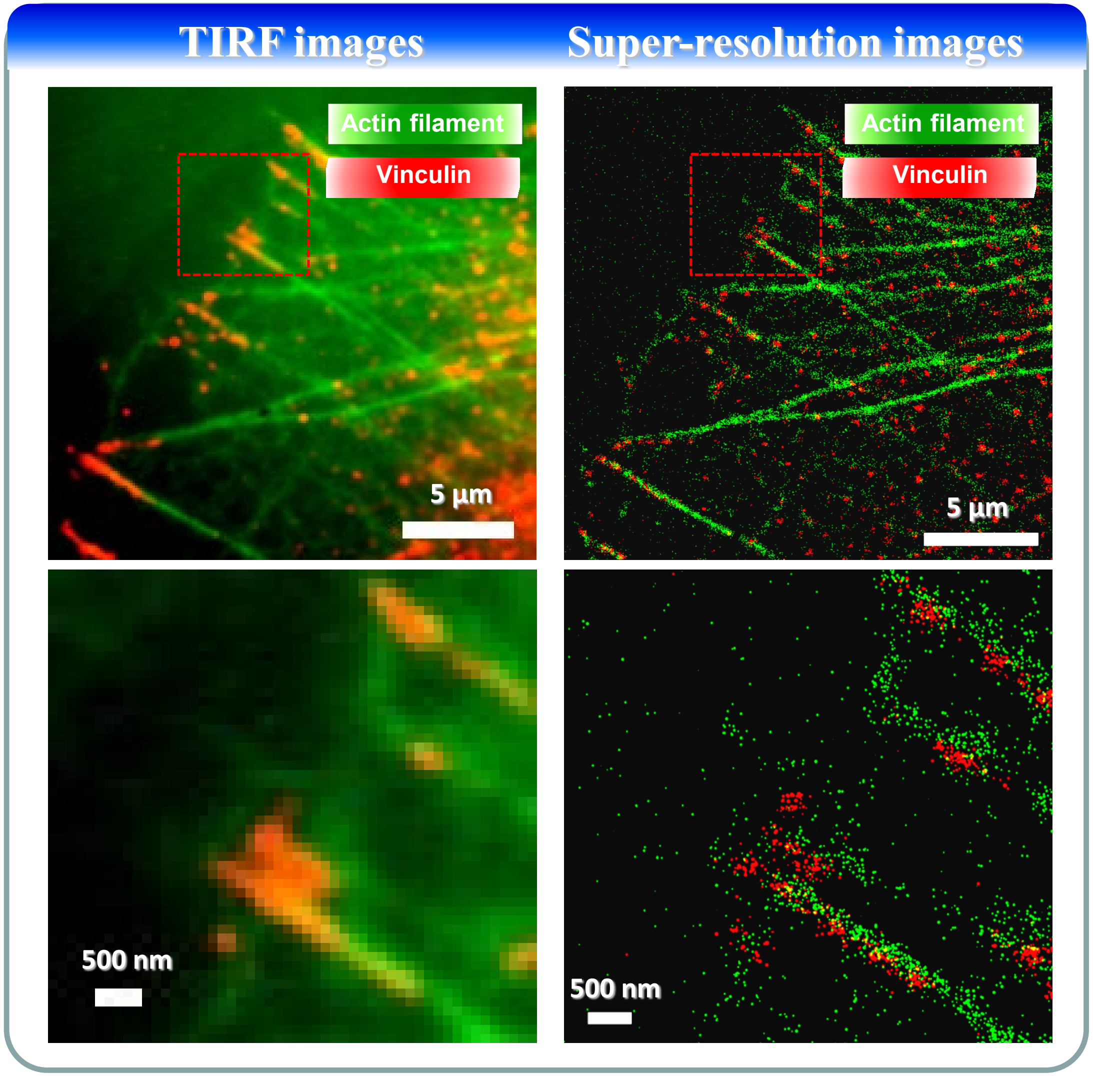

Pair correlation analysis

$$g(r) = \left\langle \frac{\rho(r)}{\bar{\rho}} \right\rangle$$

$\rho(r)$ *is the density of molecules at distance.*

r from a given molecule.

$\bar{\rho}$ *is the average* density of molecules, with this ratio averaged over the entire ensemble of molecules.

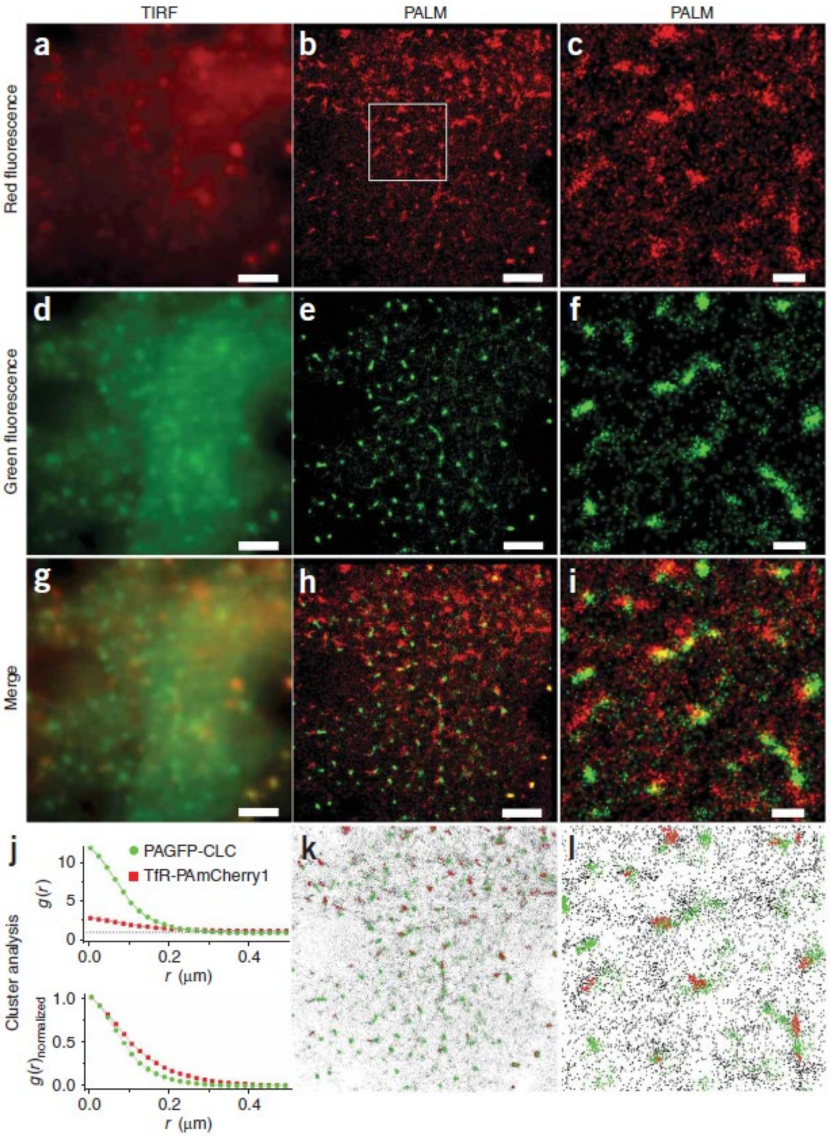

Nature methods 6, (2009)

4 Pi

Schematic of the 4Pi microscope

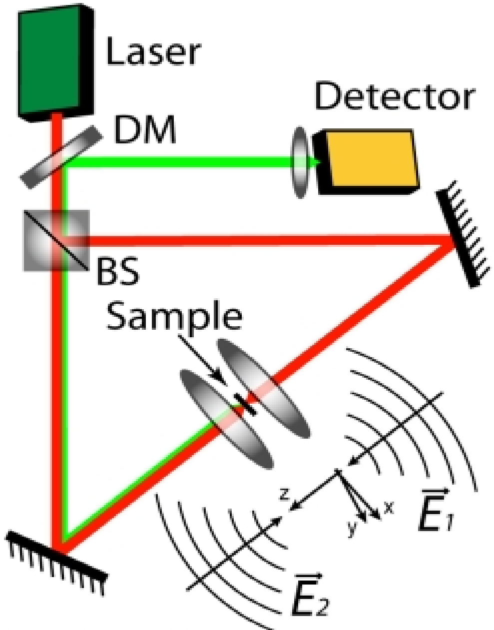

Theoretical and Computational Biophysics Group
Beckman Institute
University of Illinois at Urbana-Champaign

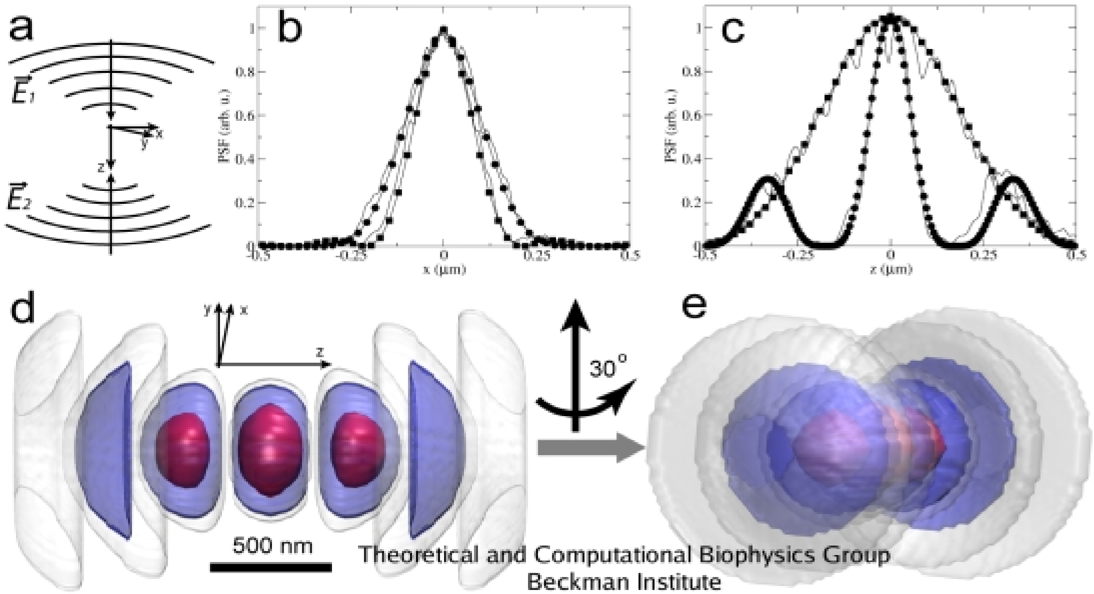

Theoretical and Computational Biophysics Group
Beckman Institute
University of Illinois at Urbana-Champaign

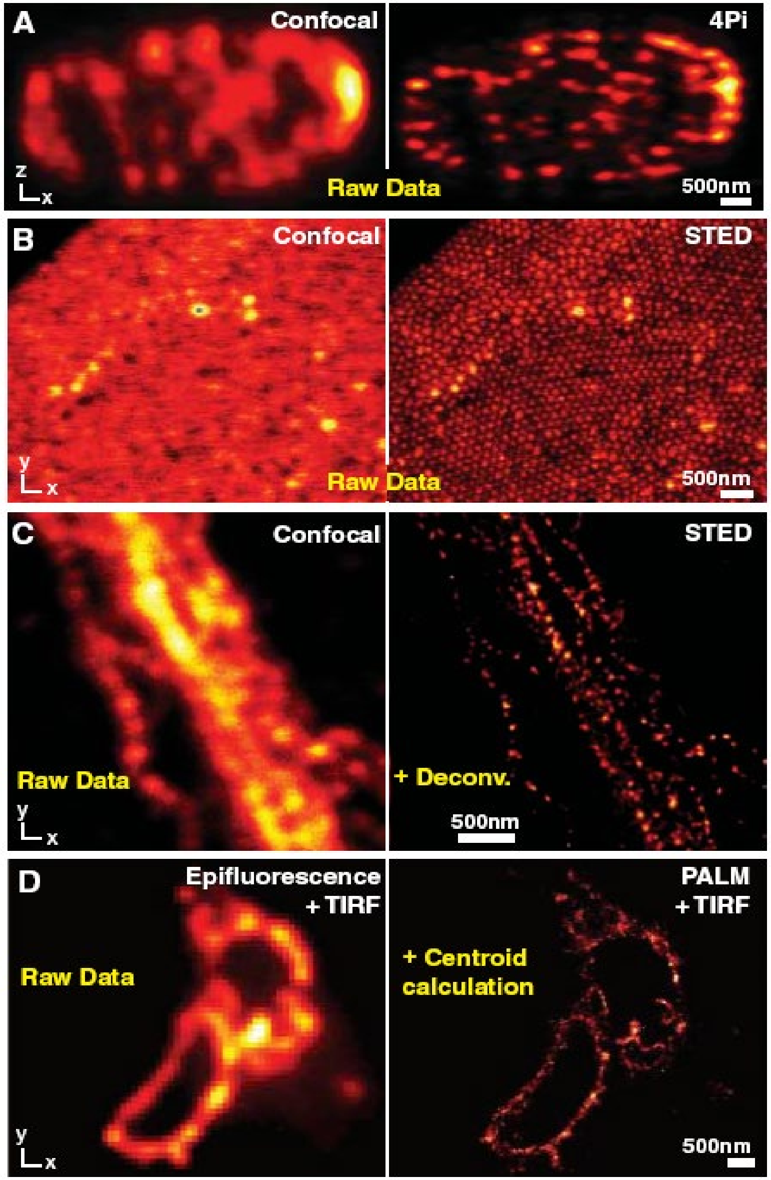

Fig. 4. Side-by-side comparisons. (**A**) Confocal versus 4Pi axial (*xz*) image of microtubules in a neuron: 4Pi image displays 140-nm *z* resolution; lens of $\alpha = 74°$ and with two-photon excitation at 800 nm. The plain 4Pi image is due to a narrow solitary peak without lobes; mathematical lobe-removal is not required. (**B**) Unlike the confocal reference, the STED image reveals the spatial order of self-assembled fused silica nanobeads containing a fluorescence core (*45*). (**C**) Neurofilaments in human neuroblastoma recorded in the confocal mode (left) and with STED after nonlinear deconvolution (right) displaying a focal plane resolution of 20 to 30 nm (*39*). (**D**) Epifluorescence versus PALM recording of a cryoprepared section from a mammalian cell expressing a lysosomal transmembrane protein tagged with a photoswitchable protein; both images were recorded with a TIRF setup. PALM resolution ranges between 20 and 60 nm, whereas individual protein localizations can be 2 nm (*12*).

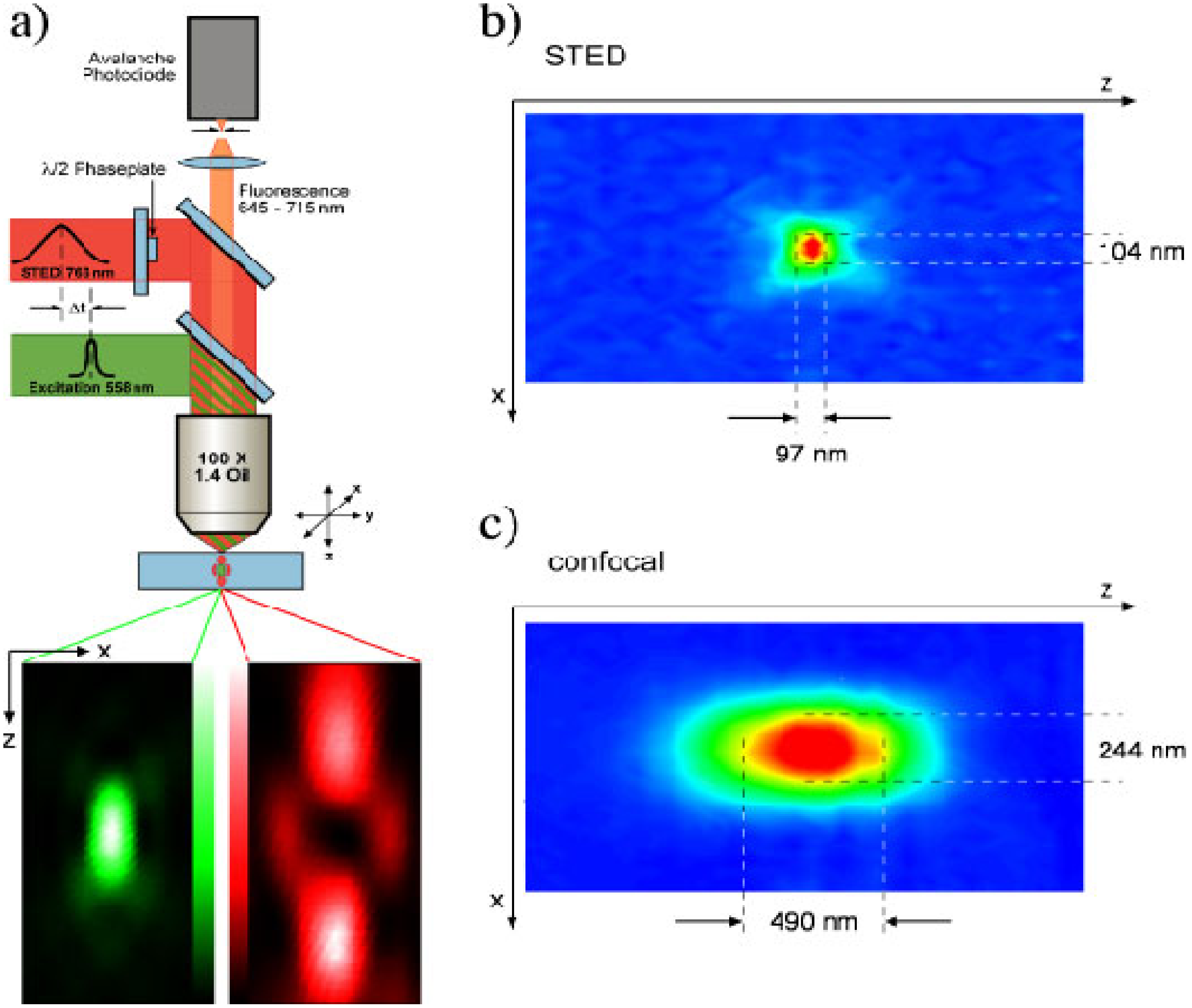
a)
Avalanche Photodiode
λ/2 Phaseplate
Fluorescence 645 - 715 nm
STED 763 nm
Δt
Excitation 558 nm
100 x 1.4 Oil
x
y
z
x
z
b)
STED
z
x
104 nm
97 nm
c)
confocal
z
x
244 nm
490 nm

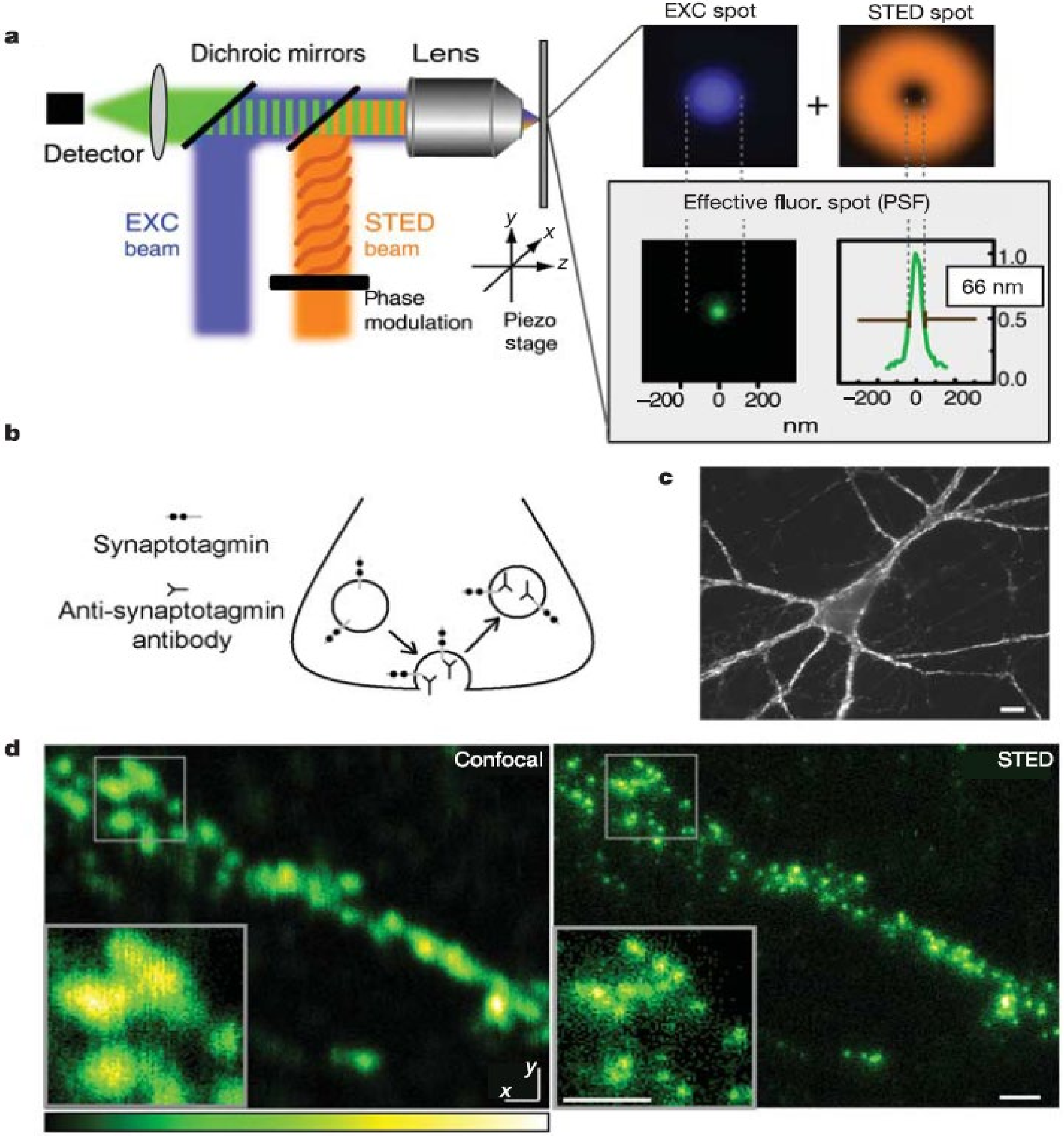
a
Dichroic mirrors
Lens
Detector
EXC beam
STED beam
Phase modulation
y
x
z
Piezo stage
EXC spot
+
STED spot
Effective fluor. spot (PSF)
66 nm
1.0
0.5
0.0
−200
0
200
nm
b
Synaptotagmin
Anti-synaptotagmin antibody
c
d
Confocal
STED
y
x

STED microscopy with continuous wave beams

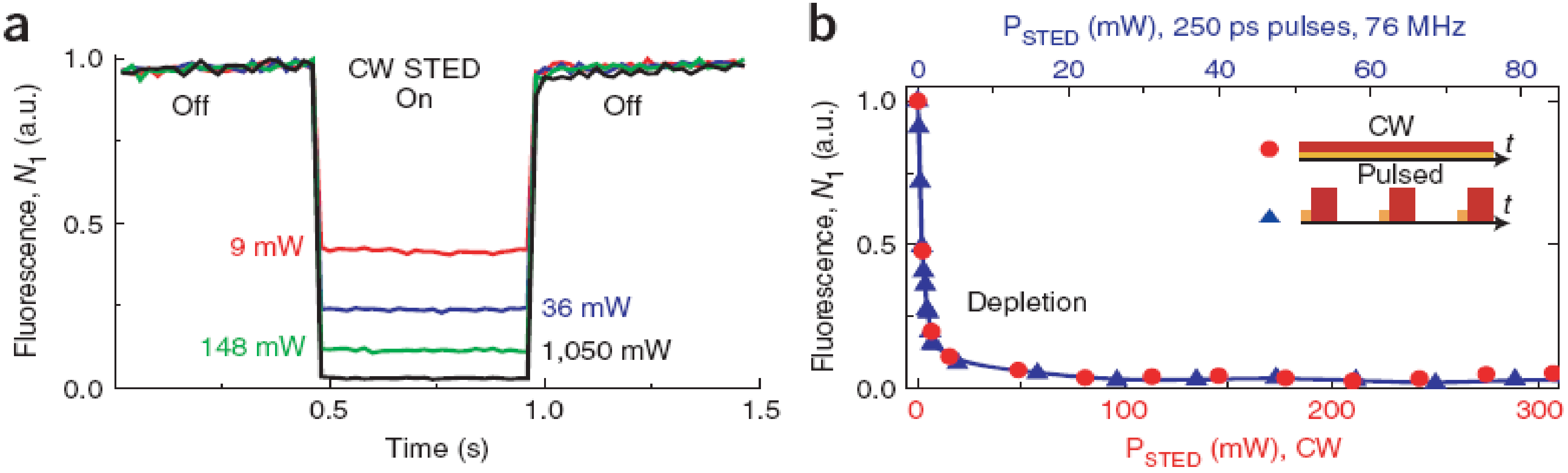

NATURE METHODS | VOL.4 NO.11 | NOVEMBER 2007 | 915

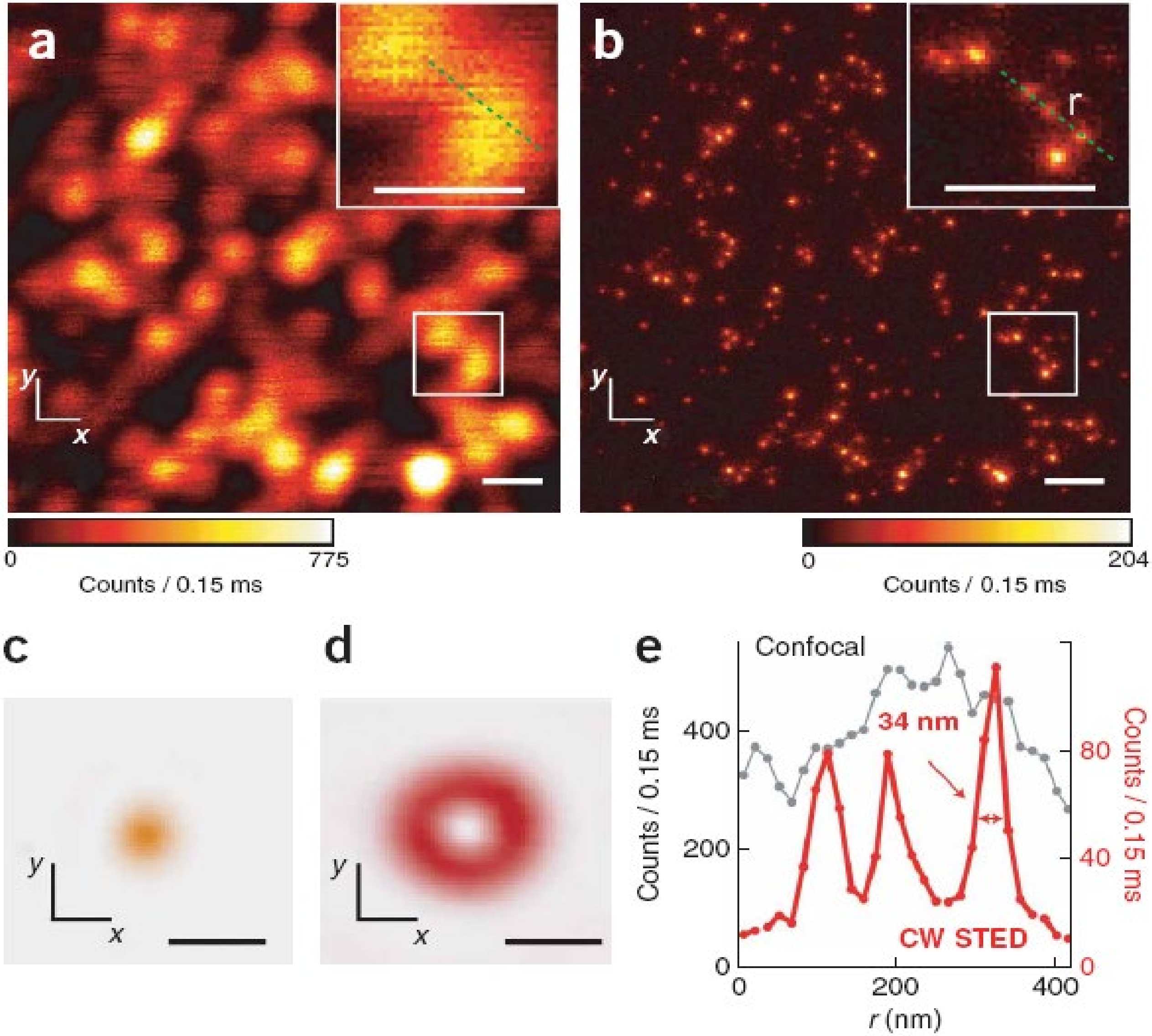
a
b
y
x
y
x
r
0
775
Counts / 0.15 ms
0
204
Counts / 0.15 ms
c
d
e
y
x
y
x
Confocal
34 nm
CW STED
Counts / 0.15 ms
0
200
400
Counts / 0.15 ms
0
40
80
0
200
400
r (nm)

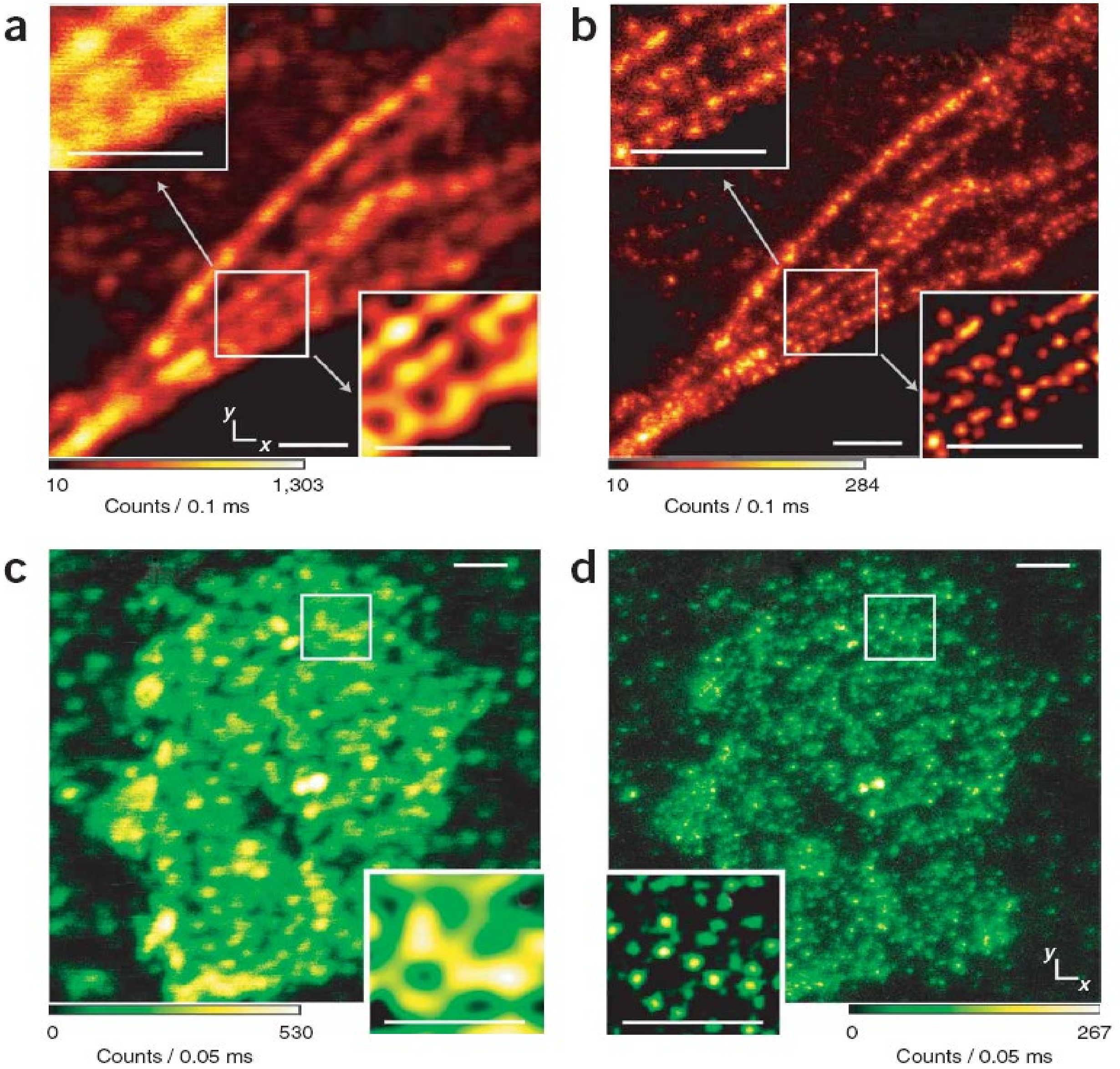
a
y
x
10
1,303
Counts / 0.1 ms
b
10
284
Counts / 0.1 ms
c
0
530
Counts / 0.05 ms
d
y
x
0
267
Counts / 0.05 ms

Journal of Microscopy, Vol. 198, Pt 2, May 2000, pp. 82–87.
Received 12 January 2000; accepted 3 March 2000

SHORT COMMUNICATION

Surpassing the lateral resolution limit by a factor of two using structured illumination microscopy

M. G. L. GUSTAFSSON
Department of Biochemistry and Biophysics, University of California San Francisco,
San Francisco, California 94143-0448, U.S.A.

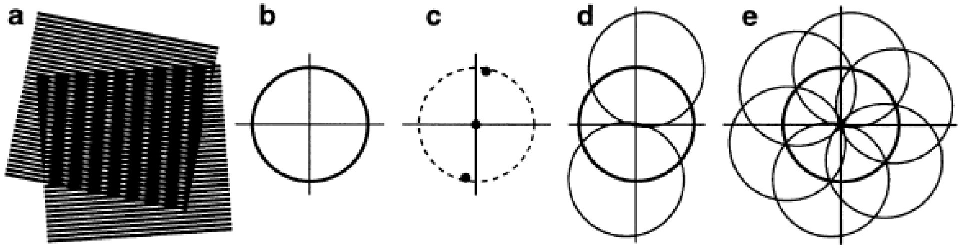

Fig. 1. Concept of resolution enhancement by structured illumination. (a) If two line patterns are superposed (multiplied), their product will contain moiré fringes (seen here as the apparent vertical stripes in the overlap region). (b) A conventional microscope is limited by diffraction. The set of low-resolution information that it can detect defines a circular 'observable region' of reciprocal space. (c) A sinusoidally striped illumination pattern has only three Fourier components. The possible positions of the two side components are limited by the same circle that defines the observable region (dashed). If the sample is illuminated with such structured light, moiré fringes will appear which represent information that has changed position in reciprocal space. The amounts of that movement correspond to the three Fourier components of the illumination. The observable region will thus contain, in addition to the normal information, moved information that originates in two offset regions (d). From a sequence of such images with different orientation and phase of the pattern, it is possible to recover information from an area twice the size of the normally observable region, corresponding to twice the normal resolution (e).

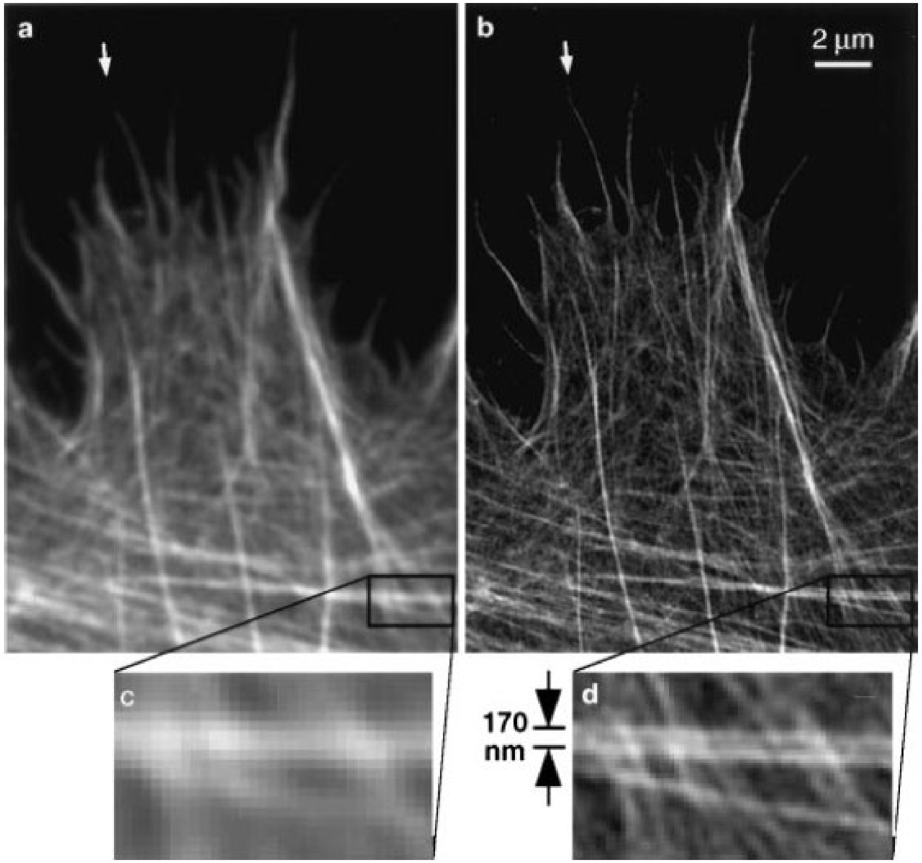

Fig. 4. The actin cytoskeleton at the edge of a HeLa cell, as imaged by (a, c) conventional and (b, d) structured illumination microscopy. (c, d) Enlargements of the boxed areas in (a) and (b), respectively. Fibres separated by less than the resolution limit of the conventional microscope are well resolved using structured illumination (d). The apparent widths (FWHM) of the finest protruding fibres [small arrows in (a, b)] are lowered to 110–120 nm in (b), compared to 280–300 nm in (a).

Nonlinear structured-illumination microscopy: Wide-field fluorescence imaging with theoretically unlimited resolution

PNAS | September 13, 2005 | vol. 102 | no. 37 | 13081–13086

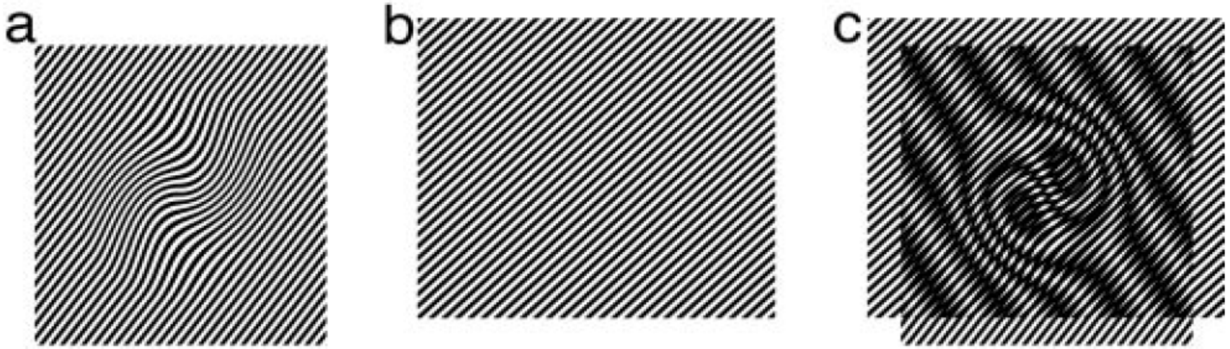

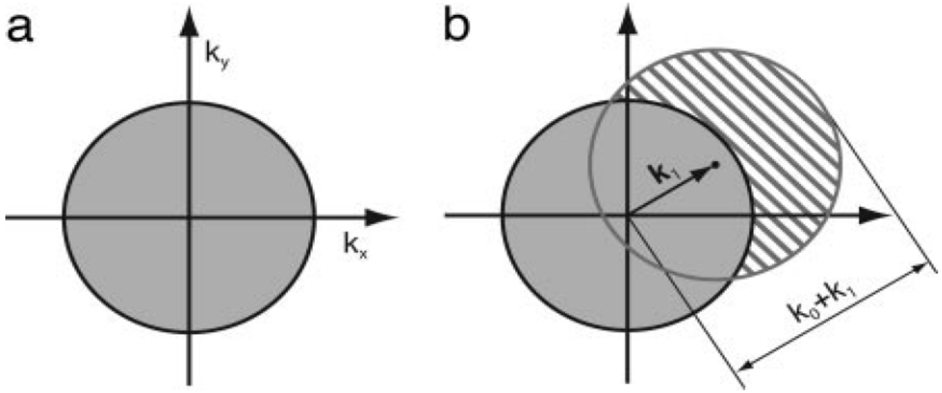

Fig. 2. Structured-illumination concept. (*a*) The set of sample spatial frequencies that can be observed by the conventional microscope defines a circular observable region of radius k_0 in frequency space. (*b*) If the excitation light contains a spatial frequency k_1, a new set of information becomes visible in the form of moiré fringes (hatched circle). This region has the same shape as the normal observable region but is centered at k_1. The maximum spatial frequency that can be detected (in this direction) is $k_0 + k_1$.

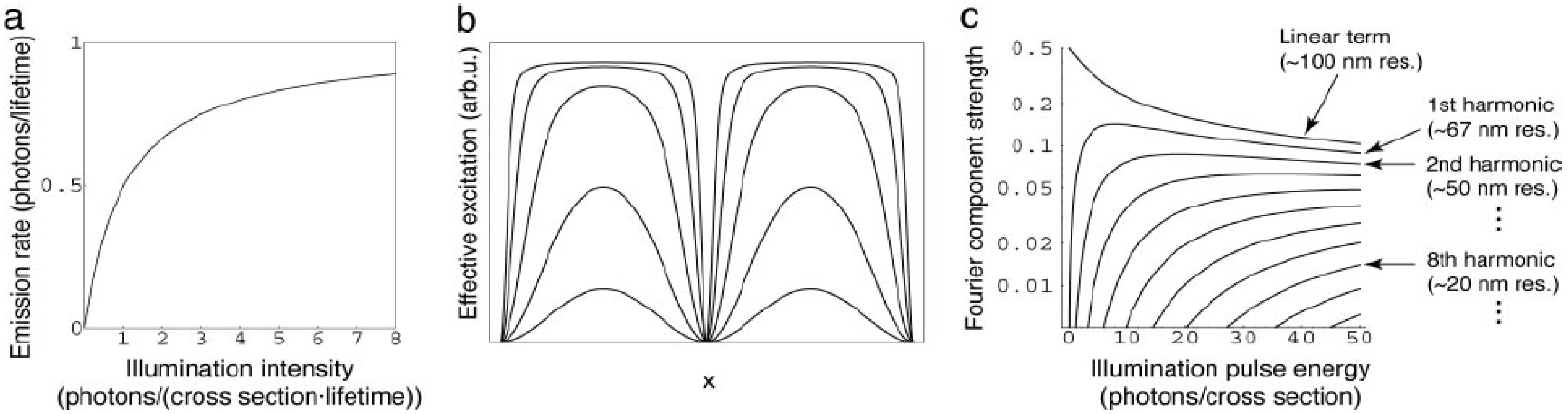
a
Emission rate (photons/lifetime)
1
0.5
0
1
2
3
4
5
6
7
8
Illumination intensity
(photons/(cross section·lifetime))
b
Effective excitation (arb.u.)
x
c
Fourier component strength
0.5
0.2
0.1
0.05
0.02
0.01
0
10
20
30
40
50
Illumination pulse energy
(photons/cross section)
Linear term
(~100 nm res.)
1st harmonic
(~67 nm res.)
2nd harmonic
(~50 nm res.)
⋮
8th harmonic
(~20 nm res.)
⋮

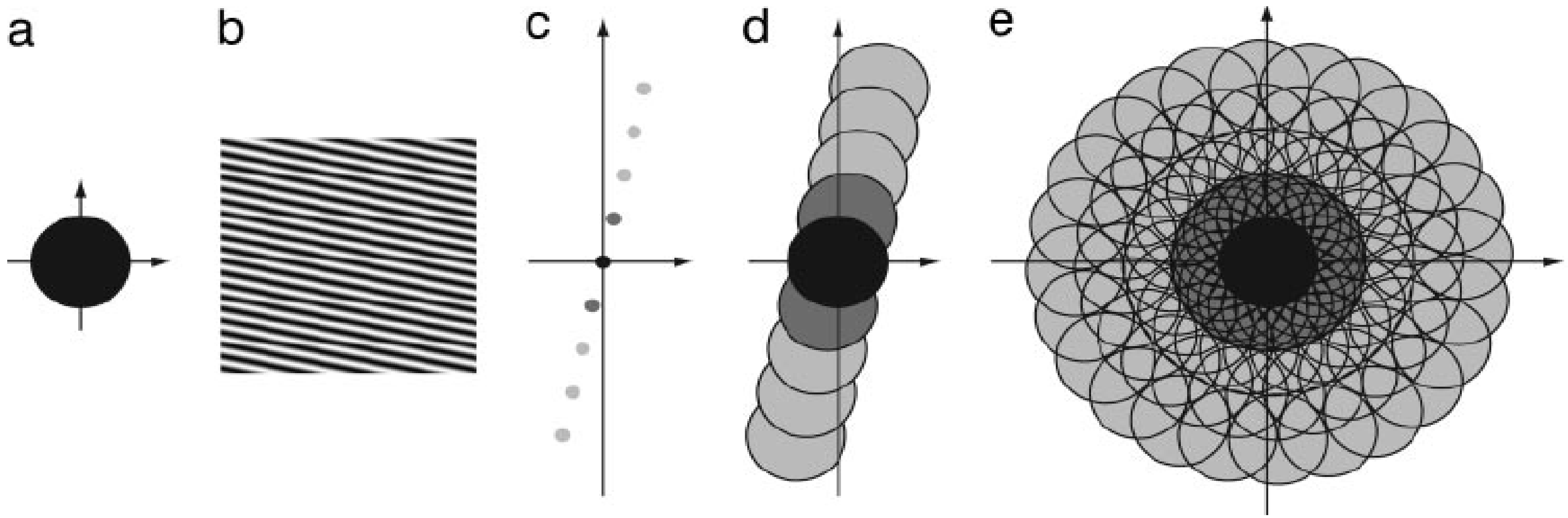
a
b
c
d
e

Subdiffraction Multicolor Imaging of the Nuclear Periphery with 3D Structured Illumination Microscopy

6 JUNE 2008 VOL 320 SCIENCE

Lothar Schermelleh,[1]* Peter M. Carlton,[2]* Sebastian Haase,[2,4] Lin Shao,[2]
Lukman Winoto,[2] Peter Kner,[2] Brian Burke,[3] M. Cristina Cardoso,[4] David A. Agard,[2]
Mats G. L. Gustafsson,[5] Heinrich Leonhardt,[1]*† John W. Sedat[2]*†

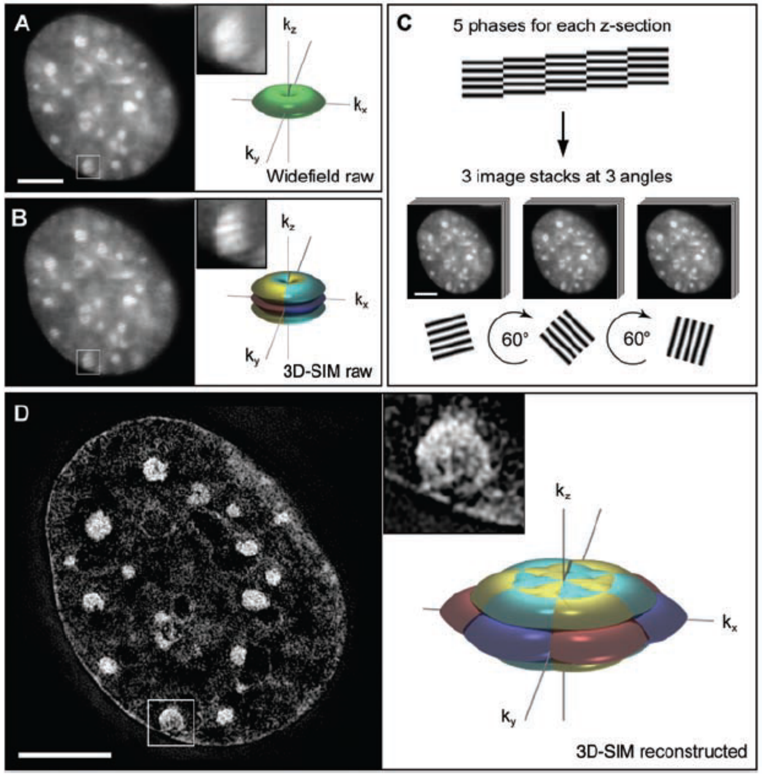

Fig. 1. Subdiffraction resolution imaging with 3D-SIM. (**A** and **B**) Cross section through a DAPI-stained C2C12 cell nucleus acquired with conventional wide-field illumination (A) and with structured illumination (B), showing the striped interference pattern (inset). The renderings to the right illustrate the respective support of detection in frequency space. The axes k_x, k_y, and k_z indicate spatial frequencies along the *x*, *y*, and *z* directions. The surfaces of the renderings represent the corresponding resolution limit. The depression of the frequency support ("missing cone") in *z* direction in (A) indicates the restriction in axial resolution of conventional wide-field microscopy. With 3D-SIM, the axial support is extended but remains within the resolution limit. (**C**) Five phases of the sine wave pattern are recorded at each *z* position, allowing the shifted components to be separated and returned to their proper location in frequency space. Three image stacks are recorded with the diffraction grating sequentially rotated into three positions 60° apart, resulting in nearly rotationally symmetric support over a larger region of frequency space. (**D**) The same cross section of the reconstructed 3D-SIM image shows enhanced image details compared with the original image (insets). The increase in resolution is shown in frequency space on the right, with the coverage extending two times farther from the origin. Scale bars indicate 5 μm.

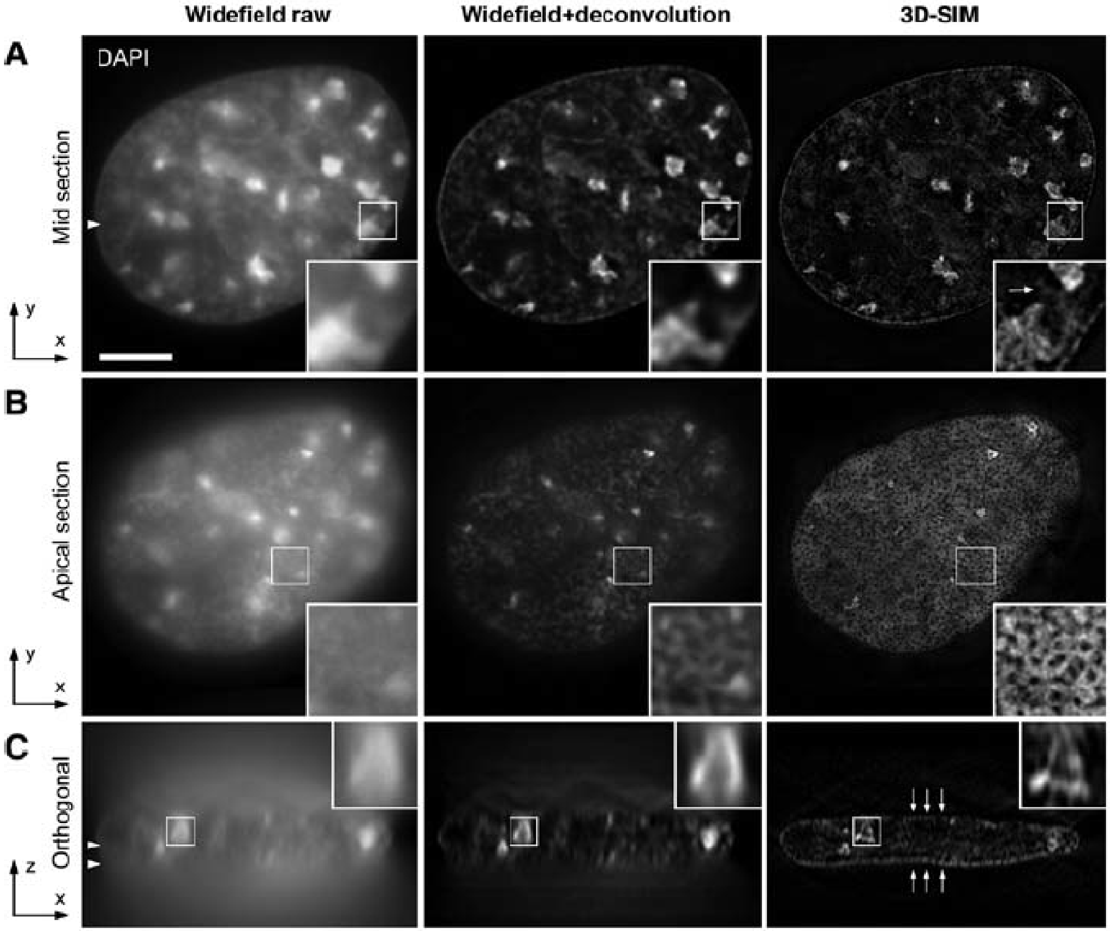
Widefield raw
Widefield+deconvolution
3D-SIM
A
DAPI
Mid section
y
x
B
Apical section
y
x
C
Orthogonal
z
x

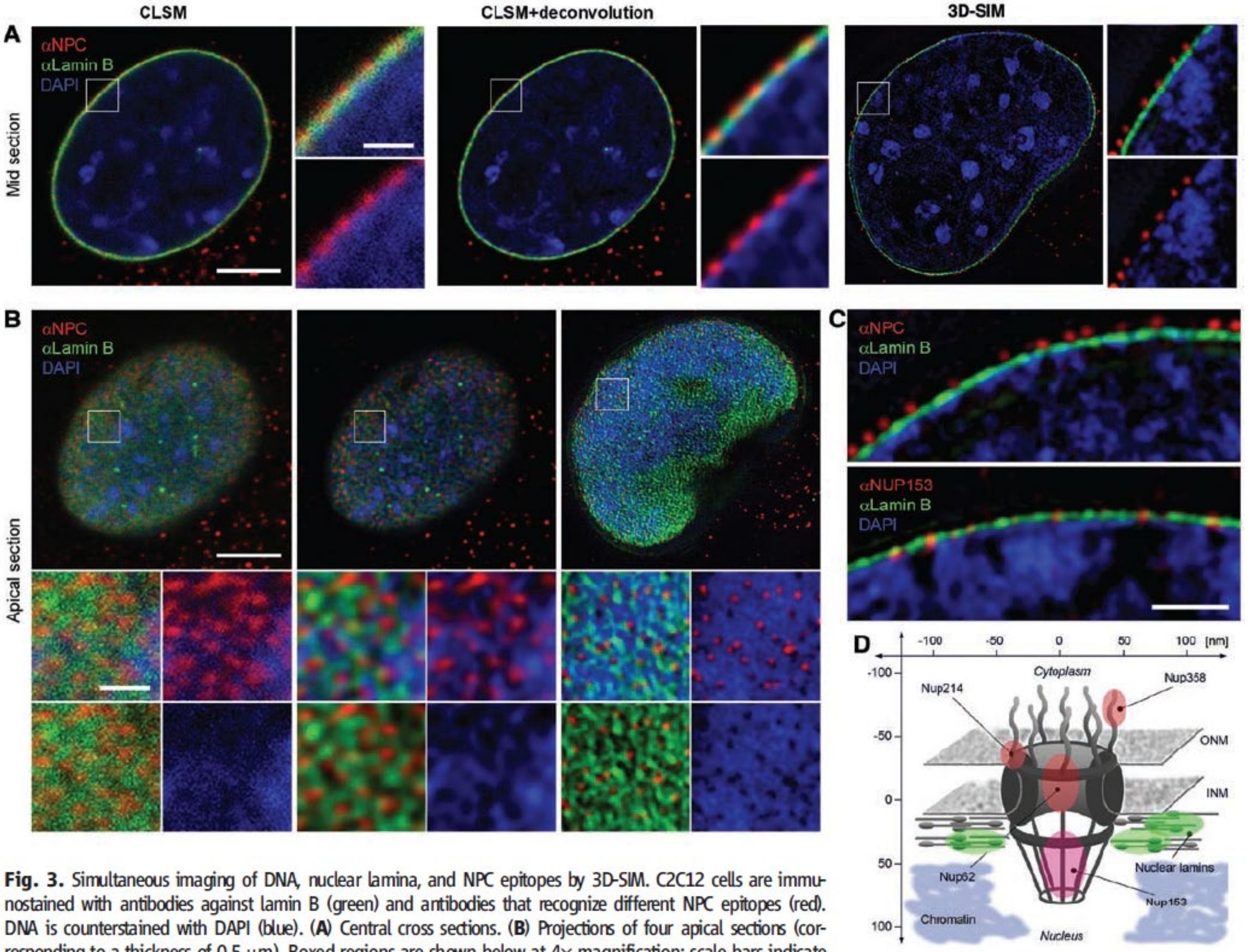

Fig. 3. Simultaneous imaging of DNA, nuclear lamina, and NPC epitopes by 3D-SIM. C2C12 cells are immunostained with antibodies against lamin B (green) and antibodies that recognize different NPC epitopes (red). DNA is counterstained with DAPI (blue). (**A**) Central cross sections. (**B**) Projections of four apical sections (corresponding to a thickness of 0.5 μm). Boxed regions are shown below at 4× magnification; scale bars indicate 5 μm and 1 μm, respectively. (A) CLSM and deconvolution still show partially overlapping signals. In contrast, with 3D-SIM the spatial separation of NPC, lamina, and chromatin and chromatin-free channels underneath nuclear pores are clearly visible. (B) Top view on the nuclear envelope. Whereas CLSM fails to resolve close nuclear pores, 3D-SIM shows clearly separated NPC signals at voids of peripheral chromatin and surrounded by an irregular network of nuclear lamina. (**C**) Mid sections comparing stainings with an antibody that mainly reacts with Nup214, Nup358, and Nup62 (αNPC) and one specifically recognizing Nup153 (αNup153). The αNPC signal is above the lamina (140 ± 8 nm), whereas the αNup153 pore signal is at the same level as the lamina (–15 ± 20 nm). Scale bars 1 μm. (**D**) Schematic outline of the NPC, showing the relative position of Nup proteins and surrounding structures. ONM, outer nuclear membrane; INM, inner nuclear membrane.

Super-resolution video microscopy of live cells by structured illumination

Peter Kner[1,2,7,8], Bryant B Chhun[1,8], Eric R Griffis[3,4],
Lukman Winoto[5] & Mats G L Gustafsson[5,6]

NATURE METHODS | VOL.6 NO.5 | MAY 2009 | 339

Structured-illumination microscopy can double the resolution of the widefield fluorescence microscope but has previously been too slow for dynamic live imaging. Here we demonstrate a high-speed structured-illumination microscope that is capable of 100-nm resolution at frame rates up to 11 Hz for several hundred time points. We demonstrate the microscope by video imaging of tubulin and kinesin dynamics in living *Drosophila melanogaster* S2 cells in the total internal reflection mode.